Design and Mechanics of Continuum Robots for Surgery

by

Robert J. Webster, III

A dissertation submitted to The Johns Hopkins University in conformity with the

requirements for the degree of Doctor of Philosophy.

Baltimore, Maryland

December, 2007

Abstract

This dissertation describes design and modeling of two new flexible, continuous backbone robotic dexterity enhancement devices, and algorithms to robotically manipulate them in surgery. These steerable needles and active cannulas provide dexterity in thin (needle-sized) form factors, permitting surgical tools to "turn corners" inside the human body.

The robotic tool manipulation algorithms are useful for rapidly and accurately aligning many kinds of surgical tools with planned poses and entry vectors. Drawing on techniques from artificial intelligence, they do not require cumbersome calibration, complete knowledge of robot kinematics, or even encoding, making them well-suited to uncertain real-world clinical environments. Simulations and experimental results demonstrate the accuracy and speed of the algorithms.

When an intervention is needle-based, steerable needles provide a means to achieve dexterity within soft tissue after insertion begins. Asymmetric forces generated by a bevel tip are harnessed robotically to generate controllable deflection, and curvature is enhanced by design of needle properties and geometry. The needle is modeled as a nonholonomic system with model parameters fit to experimental data. A new control

law inspired by mouse ballistics enables human users to teleoperatively target more accurately than traditional rate or position control.

Active cannulas are capable of similar curved dexterity without relying on tissue reaction force, making steering possible in both soft tissue and free space. Composed of multiple concentric precurved tubes, active cannula shape is described using Bernoulli-Euler beam mechanics and minimum energy principles, and predictions are corroborated with a set of experiments. Parameter values fit to experimental data are near ranges calculated from physical tube characteristics. Design tools for surgical application-specific cannula optimization are described, and differential kinematics are derived, enabling future work in image-guided control and teleoperation.

The research in this dissertation has been motivated by reducing invasiveness, improving clinical outcomes, and enabling surgical treatment for "inoperable" patients. However, the models and methods developed are broadly applicable within the fields of continuum and nonholonomic robotics.

Dissertation Advisors:

Associate Professor Allison M. Okamura and Assistant Professor Noah J. Cowan

Dissertation Readers:

Professor Russell H. Taylor and Professor Gregory S. Chirikjian

Acknowledgments

First and foremost, I would like to thank the one who is the source of life and meaning. To quote the Apostle Paul, "I consider everything a loss compared to the surpassing greatness of knowing Christ Jesus my Lord". This is the perspective with which I invite you to approach this dissertation.

I am also deeply thankful to my coadvisors Allison Okamura and Noah Cowan. One would be hard-pressed to find a professor more selflessly concerned for the good of their students Allison is. From the beginning of my graduate studies, she has continually supported and encouraged me through my many tangents and side projects with patience and good humor, as well as financial and intellectual support. Allison has been for me an example to me of how academics ought to be done. She has succeeded while maintaining balance in life, and always treated those around her with fairness and integrity. Without such an example, it is highly unlikely that I would have remained in graduate school for a Ph.D. or even considered an academic career path. Working with Noah Cowan has been similarly important to me. His enthusiasm for deeper scientific understanding is contagious. Never satisfied with the traditional Engineer's mantra, "just make it work," Noah digs deeper, faster than anyone I know

to the root of the matter. It was several years before I could leave his office without my head spinning, as he would routinely solve the most vexing problems I brought to him within minutes of hearing them. Gradually this gave way to the challenge of convincing him that models or results I produced were correct. These conversations provided the crucible from which much of this dissertation emerged.

I would also like to thank those who directly contributed to the various chapters of this thesis: Emad Boctor and Gabor Fichtinger in Chapter 2, Jin Seob Kim, Greg Chirikjian, Ron Alterovitz, Ken Goldberg, Vinutha Kallem and other Needle Steering team members in Chapter 3, and Jake Abbott, Nabil Simaan, Iulian Iordachita, Joe Romano, and Dan Gianola, who directly contributed ideas to what has become Chapter 4 of this dissertation.

In addition to those listed above, I would also like to thank my Haptics Labmates (in no particular order): Panadda (Nim) Marayong, Kyle Reed, David Grow, Netta Gurari, Sarthak Misra, Lawton Verner, Tom Wedlick, Tomonori (Tomo) Yamamoto, Carol Reiley, Chad Schneider, Katherine Kuchenbecker, Masaya Kitagawa, Mohsen Mahvash, and Todd Murphy. I have truly valued the many conversations I have had with each of you and the thoroughly enjoyable working environment the lab has been because of you. I have very much enjoyed our movie nights, chili and pasta cookoffs, poker nights, grill-outs on the balcony of Latrobe 200, and looking out on the quad with you through our 13m^2 of windows[1].

Others to whom I owe a similar debt of gratitude for conversations (both research

---

[1]Thanks to Chad Schnieder for calculating the surface area of our windows, as well as the great contribution he made to the scientific study of life in graduate school when he formulated Schnieder's laws.

related and not) over the years include: Russ Taylor, Donniell Fishkind, Louis Whitcomb, Greg Hager, Peter Kazanzides, Ameet Jain, Ankur Kapoor, Greg Fischer, Jack Li, Whitney Hastings, and Tabish Mustafa. I would also like to thank the anonymous reviewers of my publications who have contributed valuable insights that improved the content throughout this dissertation.

A very important thanks to the ME administrative staff who have many times gone out of their way to help me with orders, paychecks, registration, and many other important things that are all too easy to forget – after they are taken care of. Special thanks as well to the CS administrative staff. Their continual restocking (and cleaning) of the student lounge have enabled the mind-expanding combination of foosball and espresso that has been such a critical component of this dissertation and many others.

Finally, I would like to thank my family, and especially my wife Jessica, for their love, encouragement, and understanding. A large measure of the sacrifice of earning a Ph.D. is shared by the spouse and family of one who does so. Mine are no exception, and they deserve a corresponding measure of credit for enabling this dissertation.

Contents

List of Figures

xiv

To my dearest Jesscia.

Your love and unwavering support have made this dissertation possible.

Chapter 1

Introduction

1.1 Motivation

Manual Minimally Invasive Surgical (MIS) techniques have revolutionized surgery
in the last two decades by enabling intervention without large incisions. Computa-
tional and robotic tools for MIS appear poised to make a clinical impact of similar
importance, given recent laboratory-demonstrated advancements in surgical naviga-
tion, visualization, accuracy, and dexterity. Such computer-integrated surgical sys-
tems may include preoperative planning based on medical images, intraoperative
registration of the patient to preoperative and intraoperative imaging, a combina-
tion of robotic and manual tools for carrying out the plan, verification of surgical
objective completion, and quantitative postoperative analysis. The chief advantages
of robotic manipulation of surgical tools include accurate knowledge of tool position
with respect to anatomy, consistent movement free of fatigue and tremor, the ability
to work in imaging environments unfriendly to humans, and the ability to reposition

instruments quickly and accurately through complex trajectories.

Surgical robotic objectives may be defined by a radiologist or surgeon preoperatively or intraoperatively. Based on this distinction, surgical robots can be classified into two main groups: *Surgical CAD-CAM* systems and *Surgical Assistant* systems [163][1]. Robots in both of these categories make use of complementary skills/advantages of surgeon and robot, but do so in different ways.

Surgical CAD-CAM systems systems excel at precisely reaching a target specified preoperatively. In radiological interventions (e.g. percutaneous needle placement), these systems are used to align and sometimes insert a needle or other tool based on feedback from a variety of medical imaging modalities. Image-guided robotic systems can register tools to images and physical locations more easily and accurately than humans. The robot can then precisely manipulate instruments to reach the locations in the patient's body that are selected in medical images. The system complements the planning and decision-making ability of the surgeon by actualizing his/her intention more accurately than would be possible manually.

In robotic Surgical Assistant systems, the surgeon directly controls the motion of the instruments held by the robot. These systems combine the fine manipulation capabilities of robotic systems with the surgeon's perception and judgment, performing scaled down, tremor-free motion. They can also provide active assistance to guide surgical tools toward intended locations ("guidance virtual fixtures") or prevent them from entering dangerous areas ("forbidden region virtual fixtures") [1, 2]. Surgical

---

[1]Surgical CAD-CAM and Surgical Assistant are classification distinctions drawn from the research conducted in the Johns Hopkins University Engineering Research Center for Computer Integrated Surgical Systems and Technology by Taylor, Hager, Whitcomb, Okamura, Kazanzides and Fichtinger.

Assistants enable increased resolution of movement and vision, and can make laparoscopic tools more dexterous by providing a "wrist" near the tool tip. Laparoscopic robot wrists emulate the movement capability of human wrists much better than traditional laparoscopic tools. The most prominent example of a Surgical Assistant robot is the da Vinci system (Intuitive Surgical, Inc.) [77].

Unfortunately, both types of surgical robotic systems have thus far achieved only limited penetration into real-world operating rooms (ORs). Surgical CAD-CAM systems for needle placement have yet to reach commercial viability, while da Vinci is the lone FDA-approved commercially available Surgical Assistant system. Since the da Vinci system currently does not include active assistance, image guidance, or haptic (force and tactile) feedback, improvement of clinical outcomes is still debated in most procedures. Further impediments to more widespread use are the large size of the robot (not well-suited to ORs that must also contain many other pieces of equipment and people), as well as cumbersome setup procedures. While its rate of use continues to grow, da Vinci is currently used frequently only in a small number of specific procedures, notably radical prostatectomies. These account for a large percentage of da Vinci surgeries due to clinical performance improvements in some metrics [26], as well as patent demand driven by highly successful marketing. While these recent positive results are cause for optimism about the commercial future of surgical assistant robots in general, current devices are only a first step toward much more powerful systems including features like image guidance and registration, path planning, active guidance, haptic feedback, and many other useful laboratory-demonstrated capabilities.

Beyond da Vinci, there are many reasons for the lack of other high-impact, real-

world clinical surgical robotic systems. Many difficulties stem from the challenging environment of the OR where reliability must be near 100%, speed is at a premium (often billed by the minute), and even simple setup or calibration routines can be viewed as prohibitively cumbersome. Other real-world effects such as tissue motion, deformation, and inhomogeneity can be particularly troubling to robots that assume perfectly straight tools and consider targets as fixed Cartesian locations. Further, there remain many confined areas of the body without viable MIS alternatives (either robotic or manual) because existing tools are not of sufficiently small and dexterous to reach them.

Addressing some of the above challenges to facilitate increasing application of robots in real-world OR and interventional settings is the focus of this thesis. Enhancing ease of use and speed of setup and calibration without sacrificing accuracy can be an algorithmic and/or design problem. Given additional sensing (beyond encoders), the challenge is to use it to relax design accuracy and structural constraints and rapidly align needles or other surgical tools to the desired target with minimal calibration requirements. Dealing with needle deflections and target motion from tissue deformation, inhomogeneity, and other effects requires control of needle trajectory through tissue. Doing so requires the creation of steerable needles that can execute controllable curved trajectories, as well as models of their shape as a basis for control and planning. Reaching confined spaces in the body (that may or may not contain soft tissue) requires thin and dexterous tools that can traverse curved and winding trajectories without relying on external guiding environmental reaction forces. A challenge in creating such devices is that they must be able to change

shape inside the body. Once designed, making effective use of such devices requires kinematic and differential kinematic models. Challenges described above in tool manipulation, design, and modeling are addressed in this dissertation for several robotic and manual devices. This work aims to algorithmically improve certain aspects of the way robots manipulate tools in clinical settings, and develop design and modeling results for enhancing tool dexterity. Such results can facilitate transfer of laboratory-demonstrated robotic capabilities to real-world OR and interventional settings. The systems presented in this dissertation incorporate aspects of both Surgical CAD-CAM systems and Surgical Assistants. Needle placement normally falls under the purview of Surgical CAD-CAM, yet we also describe how steerable needles can be teleoperatively controlled. Similarly, an active cannula (needle-sized robotic manipulator) can be deployed in both an automated CAD-CAM fashion, or teleoperated as a Surgical Assistant.

1.2   Dissertation Contributions

The major contributions of this dissertation are summarized as follows:

- **Robotic Tool Alignment Algorithms.** Pose tracking of a point on a surgical robot (which can be done directly from images [114]), is used to align surgical tools and needles rapidly in the presence of several important and common forms of uncertainty, while nearly eliminating calibration procedures. This method may be directly applied to a variety of robot architectures, and it facilitates rapid prototyping of robotic surgical tool manipulation systems. It is

also designed to overcome some real-world impediments to clinical adoption of needle placement robots by making them easier and faster to use, calibrate, and operate safely. The salient features of this control method, known as "Virtual Remote Center of Motion" (Virtual RCM) control, are demonstrated in simulation and experimentally. This work was codeveloped with Emad Boctor and Gabor Fichtinger.

- **Bevel-Tip Needle Steering.** Asymmetric forces generated by a bevel-tip needle are harnessed robotically. This research resulted in several specific contributions:

  Design. Design considerations are elucidated through two novel robotic actuation mechanisms and experimental results. Enhancing shaft flexibility and appropriate choice of bevel angle increase curvature.

  Modeling. Steerable needle kinematics are described via a nonholonomic (Lie group-theoretic) model that is a generalized (SE(3)) model similar to planar bicycle/unicycle models. This is the first nonholonomic model for steerable needles (whether bevel-steered or steered via alternative methods) of which the author is aware. Both discrete and continuous forms are presented. The model was codeveloped with Jin Seob Kim and Gregory Chirikjian.

  Evaluation. Experimental results demonstrate the ability of the nonholonomic model to describe experimental steerable needle shape. When the model includes two parameters its predictions are statistically significantly better, indicating that it does not over fit the data.

Teleoperation. Mappings and control laws for teleoperation of steerable needles are proposed. Human factors experiments are used to compare various control laws, and demonstrate that a new nonlinear control law helps users be statistically significantly more accurate at tip targeting. Teleoperation results were codeveloped with Joseph Romano.

- **Active Cannulas.** Precurved elastic tubes are used to create a new kind of continuum robot suitable for surgery and other applications where dexterity is required in confined spaces. This research resulted in several specific contributions:

Design. Active cannulas are a new combination of two previously independently proposed design ideas. Counter rotation of two curved tubes to change needle curvature was proposed in [118], while translation of a curved wire tip is a feature of commercial catheter guidewires. The active cannula design combines these two ideas to form a multi-link curved continuum robot. New actuation units were also designed.

Beam Mechanics Model. The beam mechanics model described in this dissertation was the first description of the shape of active cannulas in terms of tube rotations and translations, and the first work to account for torsion in active cannula models. (A similar beam-mechanics model was simultaneously published [145], that assumed infinite torsional rigidity). Minimum energy principles are used for forward kinematics. Such techniques have not previously been applied to a system like ours.

Analysis. This research demonstrates for the first time the transcendental nature of active cannula forward kinematics (reduced to a single equation in the 3-link case). This implies the lack of a closed-form solution when infinite torsional rigidity is not assumed. However, despite transcendental forward kinematics, differential kinematics can be written in closed form.

Evaluation. Experimental results demonstrate ability of the beam mechanics model (with torsional effects included) to capture experimental active cannula shape using two parameters. Comparison with a torsionless beam mechanics model (one parameter) demonstrates both qualitatively and quantitatively the importance of including torsion for physical realism and predictive accuracy.

1.3   Related Work

Both steerable needles and active cannulas are continuously flexible robots that can be classified as continuum robots. Continuum robots are infinite degree of freedom robots characterized by flexible backbones. They are one branch of the high-degree-of-freedom area of robotics, which traces its origins to a forward-looking paper by Anderson and Horn in the late 1960s [13]. The other branch consists of hyperredundant robots whose backbones consist of many short rigid links. Since many links can, in some cases, be considered to approximate a continuum, the distinction between the two branches can and has been blurred at times. Depending on the context, similar theoretical tools and models can apply to both types of system. Sustained development of continuum and hyperredundant robots occurred in the 1980s with the

8

pioneering work of Hirose and his team, who developed many novel and innovative designs, paying particular attention to inspiration gleaned from biological systems. Much of this work is summarized in [87]. A great deal of the theoretical foundation that currently exists for hyperredundant and continuum robots and was developed in the 1990s by Chirikjian (e.g. [33–35, 37, 39–41]). More recently, Gravgne and Walker (e.g. [71, 72, 74, 75]) and Hannan and Walker (e.g. [79–81]) have studied and modeled many aspects of continuum and hyperredundant robots, respectively.

The two most important consequences of the above foundational studies with respect to steerable needles and active cannulas are (1) that continuum robots can often be approximated as consisting of a series of constant curvature arcs, and (2) that kinematics is decomposed into two mappings: one from actuators to arc parameters (curvature, plane, and arc length), and another from arc parameters to backbone shape. The former mapping is typically system specific, since actuators in each new robot design will generally influence arc parameters in different ways. The second is system independent because it is applicable for all systems that can be approximated as piecewise constant curvature.

This literature review proceeds by first describing how continuum robots can be classified by backbone characteristics and where steerable needles and active cannulas fit within this classification (Section 1.3.1). Section 1.3.2 then provides some examples of continuum robots as applied to medicine, contrasting the steerable needles and active cannulas presented in this dissertation with existing designs, and Section 1.3.3 outlines previously proposed techniques for accomplishing the system-independent mapping.

1.3.1 Backbone Classification

Hyperredundant and continuum robots have proven useful for many applications such as car painting [87], nuclear decontamination [91], inspection of unstructured environments and pipes [134, 135, 160, 161, 171, 187], and medical applications (see Section 1.3.2 below). Many possible designs have been proposed (see overviews [87, 141]).

Useful ways to classify such robot designs are according to backbone characteristics and actuation strategies. Backbones may be either continuous (continuum robots) or discrete (hyperredundant robots), and may be fixed in length or extensible. Actuation similarly may be accomplished by a few discrete actuators, or built continuously into the structure of the robot itself. Table 1.1 presents a sampling of the diversity of possible strategies. The novelty of the active cannulas and steerable needles described in this dissertation is illustrated by the final column. Dexterity/size relates the number of curved sections in a robot design to its diameter. Due to the mechanical simplicity of active cannulas, more curved sections can fit within in a smaller form factor than has been possible before.

For the active cannula, the tubes that form the backbone transmit actuator motions and transform them into curved shapes. Actuation is thus continuous since tube precurvatures contribute continuously to bending actuation as they exchange elastic energy during relative motion. For the steerable needle, the backbone is a single flexible member, and is deflected by the asymmetric forces generated by its wedge-like bevel tip as it progresses through soft tissue. It is physically inextensible.

Literature	Backbone architecture		Backbone extensibility		Actuation		Dexterity/Size		
	discrete	continuous	extensible	inextensible	discrete	continuous	low	med	high
[38, 88, 135, 172]	○			○		○	○		
[58, 158]	○		○		○		○		
[73, 115]		○		○		○	○		
[28, 87, 91]		○	○			○	○		
[149]		○		○		○		○	
Active Cannula		○	○			○			○
Bevel-Steered Needle		○	○			○			○*

Table 1.1: Table of snake-like robot architectures. Adapted and modified from [149]. * The dexterity/size ratio is actually infinite for steerable needles, but requires a suitable soft-tissue medium.

However, considering only the portion of the needle within tissue (as our model does) the backbone can be considered to extend during insertion. Further, the steerable needle may have as many curved sections as desired (new sections are added by re-orienting the bevel direction), and may even execute helical trajectories. However, all these motions require an environment where a suitable soft medium (e.g. human soft tissue) is present to generate asymmetric forces at the tip.

1.3.2 Tool Manipulation and Curved Dexterity in Medicine

Both Surgical Assistants and CAD-CAM systems for needle (or other tool) placement are generally designed to create a pivot point at body entry (overviews of surgical robot architectures and applications can be found in [155, 166]). This is useful in CAD-CAM systems because an intuitive way of aligning the tool toward the target

is to first place it at the skin entry point, then reorient it to match the desired entry vector. The pivot point is typically required for Surgical Assistants to enable them to work through small ports in the skin. There are a variety of ways to cause the tool to pivot at the entry point, and this topic is the focus of Chapter 2. Among them are mechanical and software enforcement of the pivot point, and a review of related work in both is included in Chapter 2.

While CAD-CAM steerable needle systems (or active cannulas used for CAD-CAM) relax the requirement that the needle or tool be perfectly aligned with the entry vector, needles still require approximate preoperative alignment. This can be achieved using the tool manipulation strategies described in Chapter 2. While steerability expands needle workspace from a line to a cone-like shape bounded by maximum achievable curvature, the needle must be at least sufficiently aligned preoperatively that the desired target lies within this workspace, and preferably near its center. Needle steering is a relatively new area of research, although several techniques have been proposed, as described in the related work section of Chapter 3.

Aside from needles, the idea of actively steering a surgical tool after insertion into the body has received interest in catheterization. Designs using shape memory alloys (SMA) [78,117,130] as well as electro-active polymeric actuation [76] have been proposed. SMA has also been used to create bendable endoscopes to improve the surgeon's view (e.g. [90] which was 13 mm in diameter). The smallest SMA design the author is aware of achieved active bending in a 1 mm continuum robot [14], but this design is not suited to many kinds of surgical intervention because of slow actuator response (several seconds for a full cycle), and possible lack of stiffness. The

design was eventually developed into a catheter [130]. In contrast, steerable needles and active cannulas rely primarily on the superelastic properties of Nitinol, rather than heat-activated, shape-memory effects. Active cannulas differ from SMA-based and other catheter designs in that active cannulas use internal reaction forces of tubes rather than environmental guiding forces provided by blood vessels as their primary steering mechanism. Steerable needles differ from catheters in that needles are useful for procedures in soft tissues while catheters are useful in the circulatory system.

Steerable instruments are also widely used in colonoscopy (see [140] for a description of the standard colonoscope and a review of some robotic locomotion and steering options). A variety of actuation mechanisms are possible, including pneumatic chambers (e.g. [139]), and pull wires (used in standard clinical colonoscopes). Colonoscopes are typically 14 mm in diameter at the tip [103], a size that can pass into the body without injuring the patient. Another steerable tool design by Degani et al., aimed at cardiac procedures, is 12 mm in diameter [50]. It uses two concentric jointed tubes with lockable joints to enable follow-the-leader deployment. While robotic colonoscopes and cardiac manipulators like these are examples of systems capable of curved dexterity in the body, they differ from active cannulas and steerable needles in terms of size (they are approximately an order of magnitude larger in diameter), actuation mechanism, and surgical objectives.

There have also been some efforts toward creating steerable end effectors for Surgical Assistant robots. The motivation for this comes from considering that traditional surgical robotic tools generally consist of long, stiff, cylindrical shafts with small grippers on the distal end (mimicking hand-held lapaoscopic tools). A drawback of this

13

design is that, due to the entry point pivot constraint, it requires a large open volume inside the patient (and a correspondingly larger volume outside the patient to reach everywhere within it). Optimal port placement has been studied as a means of matching robot workspace with the available space in of certain kinds of surgical procedures [4, 31]. It can improve dexterity and reduce the likelihood of robot self-collision. However optimal port placement cannot remove the requirement of open space within the patient, a fundamental implication of straight tools. Thus, it is applicable to areas of the body amenable to creation of open space such as the abdomen (which can be inflated) or chest (which already contains a cavity), where there are many port placement options.

In other surgeries (e.g. head and neck surgery), there is rarely any flexibility in port placement, since the natural openings of the mouth, nose, and ears provide the least invasive paths into the body. In these locations there is insufficient space for straight tools to work, and port placement cannot be changed to accommodate the robotic system. This motivates our desire to move away from straight, rigid tools toward actively steered flexible instruments.

One advantage of current Surgical Assistant robots over manual MIS tools is the inclusion of a wrist at the end of the tool, which can increase dexterity and reduce the amount of space necessary for the robot inside the body. Cavusoglu et al. [32] analyzed several revolute wrist designs in terms of dexterity, and Faraz and Payendeh showed that single-section snake-like wrists have superior dexterity [61] compared to designs that do not continuously bend. It was considerations such as these that have led to the development of various robotic end effectors for medical applications that

do continuously bend.

The pervasive assumption in previous flexible, curvable medical tool design is that the structure must begin fundamentally straight, and a force generated to bend it. In keeping with this, heat-activated, shape-memory devices have been devised that create mild curvature (approx. 2% strain) in 7.3 mm diameter active forceps [126], using water to transmit heat. A 10 mm diameter electrically heated device achieved similar performance [83], while an 8 mm, one degree-of-freedom curved robot for knee surgery by Dario et al. achieved nearly 5% strain by routing SMA wires through parallel solid plastic support disks [46]. Aside from SMA actuation, a variety of wire-driven, single-section continuum wrist designs have been developed. Among the smaller examples of these are the 5 mm EndoWrist instruments from Intuitive Surgical, Inc, and a 5 mm design by Piers et al. [138] for laparoscopy.

There are many distinguishing features of active cannulas and steerable needles in comparison to the above designs, not the least of which is that active cannulas utilize initially curved backbones (that can be straightened by actuation). This is a means of attaining higher overall curvature than has been possible in previous designs. Active cannulas can attain the elastic limit of Nitinol (approx. 10% strain), or even go beyond it (with respect to an initally straight structure) if task constraints do not require access to the entire configuration space. These design considerations are addressed in Chapter 4. Strain limits are much lower for initially straight devices, either because actuators (e.g. SMA) do not have sufficient force/torque/displacement capability to generate high backbone strains or because the high forces required to do so would damage other mechanism components (e.g. thin actuation wires, support discs, etc.),

or cause buckling in the central backbone. Another distinguishing feature of both steerable needles and active cannulas is the number of curved sections they can have (all prior designs mentioned in the previous paragraph have only one curved section) and the small size with which they can achieve them (this is the quality indicated by Dexterity/size column of Table 1.1). Active cannulas and steerable needles are also simpler mechanically than designs requiring external mechanisms such as wire actuation, and can exhibit much higher bandwidth actuation than SMA designs, since speed is not limited by thermal time constants. However, it is worth noting that since active cannulas and steerable needles are made from Nitinol, they are in principle able to take advantage of superelastic preformed curvature effects (their primary means of actuation) and shape memory effects simultaneously if/when useful.

One of the designs most closely related to active cannulas uses three flexible backbones around a central backbone to achieve push-pull actuation. This work was originally done by Simaan, Taylor and others at Johns Hopkins University [100,101,148–150], and subsequent development has continued at Columbia University [184,189] and Johns Hopkins University [99]. This continuum robot also has two bending sections, making it significantly more dexterous than many prior single-section designs. While the authors note that the design is miniaturizable beyond its initial 4.2 mm diameter, they have yet to explore the limits of miniaturization. Their initial goals involving surgery in the throat are suited to 4.2 mm diameter tools. One difference between this design and an active cannula is the initially straight vs. initially curved paradigm mentioned earlier. A design objective of the multi-backbone robot was to limit backbone strain to 4%, motivated by fatigue life considerations [149]. Higher

strain may be possible, but has yet to be explored. When attempting to achieve large curvature (high strain) with this multi-backbone design, one must ensure that compressive loads on all backbones remain below the threshold of buckling, and multi-backbone actuation compensation algorithms have been developed to minimize the potential for buckling in any one backbone [148]. Thus buckling prevention, fatigue life, and material strain limits all influence the maximum achievable curvature for this device.

Precurvature enables higher maximum curvature, permitting curvatures that would exceed the material elastic strain limits of initially straight structures. Thus, active cannulas are in principle able to negotiate tighter corners within anatomy than initially straight continuum robots can. Further, fatigue life is not expected to be a design constraint for active cannulas, because they will be suitable for use as disposable medical devices due to their mechanical simplicity, as discussed in Chapter 4. Also, the limit of miniaturization will likely be smaller for active cannulas that consist of one backbone, compared to designs consisting of multiple backbones, or that require wire or other actuation applied to support discs mounted on the backbone.

One potential limitation of the active cannula design is possible difficulty in directly controlling the curvature of individual links. Links will generally be coupled, and directly controlling the curvature of a specific link independent of the others will require that at least two tubes be fully overlapping, not translate with respect to one another, and ideally that their respective curvatures be designed to preclude energy bifurcation (described in Chapter 4). Thus, in practice it is expected that active cannula individual link curvatures will be coupled, which may complicate inverse

kinematics and control compared to designs where actuators more directly influence arc parameters.

1.3.3 Kinematics for Curved Robots

Many continuum robots have been observed to exhibit approximate constant curvature (e.g. $[13, 42, 80, 87, 91, 149]$, among others). Analytical arguments in $[71, 72]$ show that the equilibrium position for a single section wire-driven continuum robot undisturbed by external forces can be considered a circular arc, provided that support disks (through which actuation wires pass) are included with sufficient frequency along the length of the backbone. While it is possible to describe the shape of variable curvature elastic structures $[110]$, constant curvature is a desirable feature that has been used to simplify kinematic analysis of continuum robots from a process involving an integral along the backbone to a process involving a finite number of links. It can thereby facilitate further studies on many topics, e.g. inverse or differential kinematics.

Piecewise constant curvature allows kinematics to be divided into two mappings. The first is from actuator space, q, to a description of circular arcs. Arcs are often parameterized by "arc parameters". For each arc, there will be an associated curvature, $\kappa(q)$, arc length $\ell(q)$, and angle of plane, $\phi(q)$, in which the arc lies (measured about the tangent vector at the end designated the "base"). This mapping from actuators to arc parameters in generally system specific, since various actuator types and configurations influence arc parameters in different ways. The second is
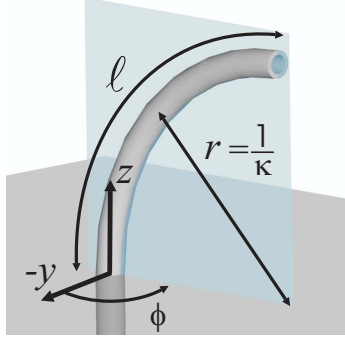
Figure 1.1: Arc parameters describe a circular arc in terms of curvature, plane, and arc length ($\kappa(q)$, $\phi(q)$, and $\ell(q)$). The axes shown are those of the fixed spatial frame.

a system-independent mapping from arc parameters to the pose of points along the backbone.

Chapters 3 and 4 of this dissertation address both mappings for steerable needles and active cannulas, two new continuum robots. Thus, a brief description is provided below of the system-independent mapping, the various ways it has been derived in literature, and how it applies to the steerable needle and active cannula models presented in this thesis.

Arc Geometry

Examination of the geometry of a continuum robot provides a means of determining the pose of points along it. Examining Figure 1.1, when $\phi = 0$ the coordinates of a point on the circular arc of radius r in the $y - z$ plane centered at $[0 \;\; -r \;\; 0]^T$ are $\mathrm{p} = [0 \;\; r(\cos\theta - 1) \;\; r\sin\theta]^T$, and the transformation from arc base to tip is

$$
\mathrm{T} = \underbrace{\begin{bmatrix} \mathrm{R}_z(\phi) & 0 \\ 0 & 1 \end{bmatrix}}_{\text{Rotation}} \underbrace{\begin{bmatrix} \mathrm{R}_x(\theta) & \mathrm{p} \\ 0 & 1 \end{bmatrix}}_{\text{Inplane Transformation}}.
$$

19

Noting that $\kappa = 1/r$ and $\theta = s\kappa$ (where $s \in [0 \quad \ell]$), this can be written as

$$T = \begin{bmatrix} \cos(\phi) & -\cos(\kappa s)\sin(\phi) & \sin(\kappa s)\sin(\phi) & \frac{(1-\cos(\kappa s))\sin(\phi)}{\kappa} \\ \sin(\phi) & \cos(\kappa s)\cos(\phi) & -\cos(\phi)\sin(\kappa s) & \frac{(\cos(\kappa s)-1)\cos(\phi)}{\kappa} \\ 0 & \sin(\kappa s) & \cos(\kappa s) & \frac{\sin(\kappa s)}{\kappa} \\ 0 & 0 & 0 & 1 \end{bmatrix}. \qquad (1.1)$$

Note that the frame in Equation 1.1 is aligned so that the curvature of the tube is about the positive x axis (its y axis points radially outward from the center of the circular arc, in the plane of the arc). Sometimes, it is be convenient to express tip orientation such that it will align with the base frame when it is "slid" along the arc to the base. This can be done by post multiplying T by $\begin{bmatrix} R_z(-\phi) & 0 \\ 0 & 1 \end{bmatrix}$.

This result can be derived using Denavit-Hartenburg parameters, modeling the arc as a combination of 5 rotational and prismatic robot links with suitable constraints [80]. It can also be obtained via Frenet-Serret frames [80] (with suitable assumptions on the sign of κ), as well as via a similar method [39] that has the advantage of being able to handle the zero curvature case (the Frenet-Serret frame is undefined at $\kappa=0$).

Needles and Cannulas as Continuum Robots

The steerable needles and active cannulas described in this dissertation exhibit approximately constant curvature. With steerable needles, a new circular arc is added each time needle is axially rotated to reorient the bevel and then translated. Thus it can have a large (theoretically infinite) number of links. More importantly, the system is inherently nonholonomic, so such a product of transformations would describe the

20

shape only if the complete sequence of joint motions is specified a priori. This would preclude online control of needle trajectory during insertion. Thus, rather than apply a product of many transformations, we sought a differential model mapping actuators directly to shape. This model is based on Lie group theory and inspired by intuition of the needle as a nonholonomic system. Here, actuators directly control ϕ and ℓ, for a constant κ (defined by needle and tissue properties). We describe how the differential model can be written in discrete form and integrated to accomplish the system-independent mapping.

For active cannulas, the system-specific mapping is substantially different from any prior continuum robot design because of the effects of elastic tubes and precurvatures, and thus we apply beam mechanics modeling techniques. The system-independent mapping is accomplished via a Lie group theoretic model similar to the steerable needle, but consisting of a finite number of links. This formulation facilitates a derivation of active cannula differential kinematics in closed form without requiring closed form forward kinematics.

1.4   Dissertation Overview

This introductory chapter presented the motivation for robotic tool manipulation and dexterity enhancement in medicine. Two new robotic dexterity enhancement devices, steerable needles and active cannulas, were placed within the context of established results in continuum robotics in terms of both design (classification by backbone characteristics) and theory (system-specific and system-independent mappings).

Chapter 2 considers robotic tool manipulation. The main focus is to describe several possible methods of creating software enforced constraints, creating a remote center of motion of a needle without assuming perfect knowledge of robot kinematics and while using minimally calibrated systems. Tool manipulation algorithms are studied both in simulation and experimentally, demonstrating rapid convergence to correct alignment using heuristic search techniques. The results of this chapter are useful for robotically manipulating many types of surgical tools, including the steerable needles and active cannulas described in subsequent chapters. Chapter 3 describes how to create a steerable needle by harnessing asymmetric forces generated by a bevel tip. We explore design considerations for steerable needles, and model the needle trajectory within tissue. Parameters are fit to experimental results and, the bevel-steering model is experimentally validated. Teleoperation of steerable needles is implemented and a custom-designed nonlinear control law is compared with position and rate control via human subject experiments. Chapter 4 describes the design and modeling of active cannulas. Beyond the basic beam-mechanics-based model, we explore the hypothesis that overall cannula shape locally minimizes stored elastic energy, and examine the significance of modeling torsional effects in addition to bending effects. The model enables several predictions of physical behavior which are demonstrated experimentally. We conclude and discuss future work in Chapter 5.

Chapter 2

Virtual Remote Center of Motion

Tool Manipulation

Robots designed for image guided needle-based interventions can improve the accuracy and precision of tip placement within the human body in comparison to current gold standard free-hand techniques. They can match preinsertion alignment to a planned straight trajectory from clinician selected skin entry point to internal target point. Steerable tools (including bevel-steered needles and active cannulas), while relaxing alignment accuracy requirements, also require preoperative alignment to ensure that the device workspace (bounded by maximum achievable curvature) contains the target. While the excellence of robots at needle placement has been well established by many research groups, widespread clinical adoption of needle placement and tool alignment robots has not immediately followed. Obstacles that must be overcome to bring such robots into standard clinical use include (1) reducing robot cost (2) increasing the speed of system setup and operation, and (3) streamlining

calibration procedures. In laboratory settings, it is also important to be able to rapidly adapt a given robot manipulator to hold new kinds of surgical tools. This is facilitated by removing dependence on the coincidence of the surgical tool and a mechanically constrained fulcrum point. We address cost and speed algorithmically without sacrificing accuracy, enabling the use of robots that are mechanically simple and permitted to have unknown transformations (e.g. passive positioning arms) in their kinematic chains. Ease of use is improved by combining fiducial-enabled, image-based sensing of tool pose with our algorithm that nearly eliminates calibration. The algorithm is also applicable when the tool does not lie on a mechanically constrained fulcrum, enabling rapid retrofitting of existing robots to manipulate new tools (e.g. multiple kinds of needle, radiofrequency ablation probes, active cannulas, etc.).

The research described in this chapter was published in [23–25], and has subsequently successfully been applied by collaborators to needle placement in both phantom studies and animal models [18, 19] and under 3D ultrasound guidance [23]. Further experiments comparing the accuracy of a robotic system using the motion control algorithms described in this chapter to the manual accuracy of a surgeon has been submitted for publication [20].

2.1   Motivation and Related Work

Recent advances in medical imaging have encouraged a rapid increase in minimally invasive image-guided interventions, including biopsy and other needle or cannula-based local therapies. The success of these procedures hinges on the accuracy of

preoperative tool alignment. Conventional unassisted free-hand techniques depend primarily on the physician's hand-eye coordination resulting in inconsistent and potentially inaccurate tool alignment and final tip placement. As an appealing alternative, medical robots offer the potential to manipulate surgical instruments more precisely and accurately than is possible by hand. At the same time, contemporary medical robots introduce a prohibitively complex engineering entourage into otherwise straightforward needle placement procedures.

Manual needle placement typically includes the following three decoupled tasks: (1) move the needle tip to the preselected entry point with 3-degree-of-freedom (DOF) Cartesian motion, (2) orient the needle by pivoting around the entry point using 2–DOF rotation, and (3) insert the needle into the body using 1–DOF translation along a straight trajectory. While steerable tools (e.g. steerable needles and active cannulas) and curved trajectories allow for a larger margin for error, the above sequence remains important to ensure that the desired target lies within device workspace. The technical challenge for robot-assisted needle placement has been to reproduce the above sequence of motions robotically in a safe, practical, and affordable manner.

One means of addressing these technical challenges is to use serial linkages and coordinate the joints under computer control, as was done in the Zeus and Aesop laparoscopic robots (formerly of Computer Motion, Inc., currently owned and discontinued by Intuitive Surgical, Inc.). Similar solutions have been used with IGOR [165], PUMA [49, 112], Neuromate [116, 169], Kawasaki [190], Sankyo Scara [144], and LARS [162] systems. However, general serial linkages like these present two fundamental problems. First, the robot kinematics induces singularities, which can be

problematic in medical applications. Another difficulty with conventional serial robots is that their use requires a fully described and precisely encoded kinematic chain. It is rather difficult to calibrate these arms and losing calibration accuracy during clinical use is a critical risk.

A decidedly more appealing and safer alternative is the family of kinematically decoupled robots. These devices contain separately controlled and sequentially operated Cartesian, rotational, and insertion stages. Thus, they appear to be a more natural fit for the process of needle placement. They are also safer because the range of motion of each individual stage can be independently constrained and mechanically locked if needed. The least straightforward action for a decoupled needle placement robot is orienting the needle toward the preselected target. One approach is to use a 2–DOF design that mechanically constrains the fulcrum point at the needle tip. Goniometric arcs have been proposed to perform this function [82], but these are impractical for needle placement because the fulcrum point must be in the center of the arcs, blocking access to the patient. Taylor et al. implemented the remote center of motion (RCM) point concept in a laparoscopic robot [164], where the fixed fulcrum point is produced farther away from the mechanism, leaving room for surgical instruments and clinical personnel to access the patient. The RCM concept has been applied in several laparoscopic and needle placement robots, including commercial systems such as the da Vinci (Intuitive Surgical, Inc.). At Johns Hopkins University, Stoianovici et al. developed a chain-drive RCM robot that is used in conjunction with a radiolucent needle driver for percutaneous access [156]. Variants of this robot have been tested under image guidance using fluoroscopy [157], computed tomography

(CT) [62], ultrasound (US) [22], and CT–fluoroscopy (CTF) [152]. The workflow in these systems is usually the following: (1) register robot to imager, (2) select target and entry points, (3) solve inverse kinematics, (4) move needle to entry point, (5) align needle with target, and (6) insert needle. Depending on the number of actuated degrees of freedom available, some steps may be executed manually, but the workflow remains the same.

While the RCM paradigm has had a significant impact on the field, it also has some disadvantages: (1) precise construction must guarantee the existence of a known fulcrum (RCM) point, (2) a tool holder must be carefully designed for each new tool, placing it exactly on this RCM, (3) each joint must be fully encoded, and (4) the robot must be carefully calibrated. An appealing alternative to the mechanically constrained fulcrum point is generating a programmed or "Virtual RCM" in software, used with decoupled and nearly uncalibrated Cartesian, rotational, and insertion stages. This system has the advantages of (1) not requiring tool–RCM coincidence, (2) requiring only minimal (entirely offline) calibration processes, (3) decoupled workflow mimicking the manual procedure, (4) rapid convergence to correct alignment, and (5) providing redundant sensing (robot pose tracking and encoders) to enhance safety. Creating such a system is the focus of this chapter.

A variety of established controls techniques are applicable to objectives like those listed above. Contemporary Magnetic Resonance Imaging (MRI), fluoroscopy, and CTF allow for real-time visualization, which enables real-time tracking of surgical instruments. Three-dimensional US-guided interventional systems [22, 185] also include a real-time tracker in the field of interest. In these systems, one can track the end

effector of a surgical robot and manipulate the device under visual servo control. It has been known in general robotics that the operational space formulation [107] and partitioned control [44] can be used to alter the behavior of the system to appear, kinematically and dynamically, to be an RCM device. Unfortunately, existing kinematic and dynamic models need to be precise, so the joints need be fully encoded and calibrated. Extensive research has also been devoted to visual servo control [89], but work applied to uncalibrated and/or unencoded robots has focused on estimating the robot's Jacobian rather than generating a Virtual RCM. Artificial intelligence (AI)–based algorithms for robot motion have also been investigated, but not yet applied to the needle placement task. These algorithms have been used in the control of uncalibrated mobile robots to explore unknown environments and navigate familiar environments [55]. Related research has also examined the effect of uncertainty in robot sensors and/or the environment [16] to generate a collision-free maps.

Our present contribution is to compose an essentially uncalibrated needle placement robot from three linear stages, two rotational stages, one linear insertion stage, and an AI-based motion algorithm to create a Virtual RCM robot that does not require encoded joints or complete knowledge of the robot kinematics. Unlike classic RCM robots, the Virtual RCM method does not require (1) the existence of a physically fixed fulcrum point, (2) a priori knowledge of the kinematic chain, or (3) encoding of the joints. This relaxes many requirements previously imposed on RCM needle placement robots. For example, the axes of the prismatic stages do not need to be orthogonal, the axes of rotation stages do not need to intersect, and kinematically unknown passive linkages are permitted anywhere within the chain. This allows

robots using the Virtual RCM algorithm to be simple and inexpensive to construct, eliminates laborious calibration, and permits testing of new robots or parts of robots to proceed rapidly without affecting the accuracy of image guidance.

2.2   Virtual RCM Algorithm

2.2.1   System Overview

Our proof-of-concept system (Figure 2.1) is comprised of a 3–DOF motorized Cartesian stage (NEAT, Inc.), a passive unencoded adjustable arm, a 2–DOF motorized rotational stage designed by Stoianovici et al. [153]. The Virtual RCM algorithm requires measurement of the pose of a point on the robot with a known transformation to the tool frame. In clinical practice, fiducials attached to the robot can provide this information directly from CT [114] or MRI images. When using US as the imaging modality, magnetic tracking can provide the pose of both the image and the tool [23]. In our system, we attach a magnetic tracker (Flock of Birds, model 6D FOB, Ascension Technology, Inc.) to the tool holder. The passive arm shown in Figure 2.1 helps in gross initial positioning of the needle tip and also purposely introduces an unknown linkage in the kinematic chain, demonstrating that the Virtual RCM does not require fully defined kinematics. The tool holder also purposely removes the RCM property of the Stoianovici rotation stage by holding the needle off the RCM point, demonstrating that the Virtual RCM does not require careful construction of the fulcrum constraining mechanism or the tool holder.
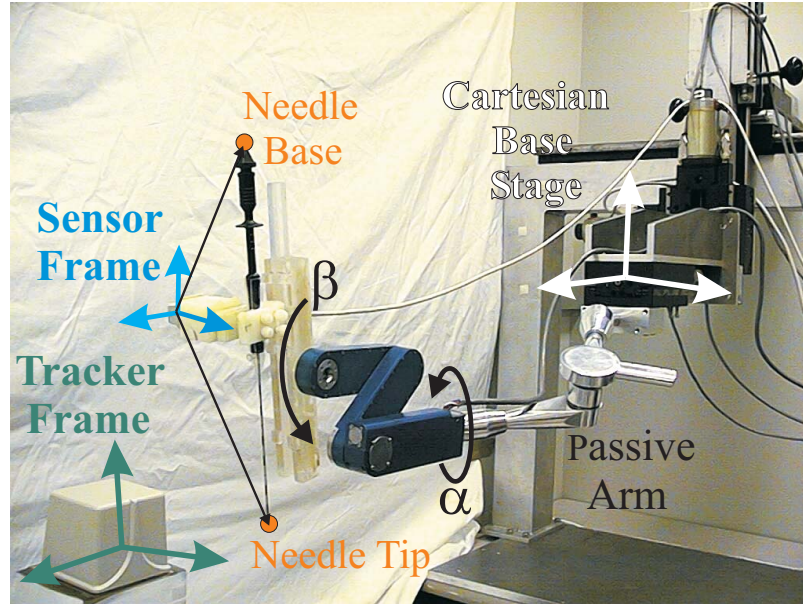
Figure 2.1: Photograph of Virtual RCM experimental setup showing a Cartesian base stage, an unencoded passive positioning arm, and a wrist with two degrees of freedom [153]. The tool, an ablation needle, is attached so that it does not coincide with the RCM point. The pose of a point on the tool holder is sensed with the magnetic tracker shown.

Low-level control of the robot is achieved using a motion control card (MEI, Inc.), driven with the Modular Robot Control (MRC) library developed at the Johns Hopkins University [165]. The readings of the FOB tracker are reported to a PC running the 3D Slicer medical data visualization package [108]. Slicer is a public domain, open source program primarily developed by the MIT AI Lab and the Surgical Planning Laboratory at the Brigham and Womens Hospital, with sustained contribution from Johns Hopkins. In Slicer, we create a 3D virtual environment (Figure 2.2) where objects are represented in the FOB tracker coordinate frame.

The incremental adaptive motion cycle of the Virtual RCM algorithm is described in Sections 2.2.2–2.2.3, tested in simulation in Section 2.3, and experimentally verified in Section 2.4. It aligns and translates the needle and requires knowledge of
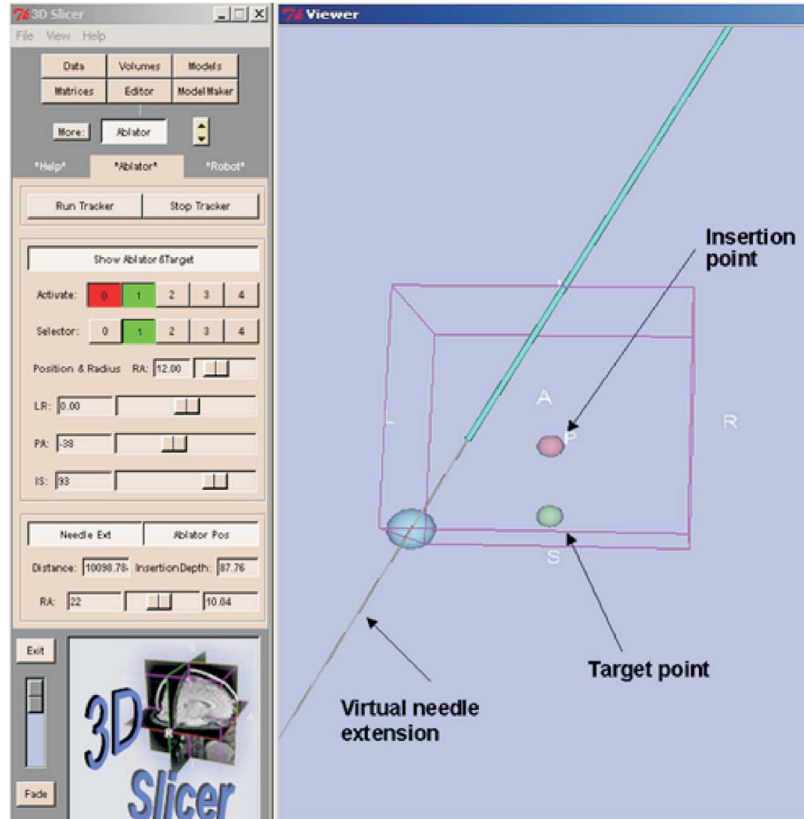
Figure 2.2: The 3D Slicer graphical user interface. Pictured is the needle with a virtual needle extension line on which is shown a spherical planned ablation zone. The insertion point and target are also represented as spheres.

the transformation between the magnetic sensor and the tool frame. Using readings from the FOB tracker, this transformation is determined off line by a version of the pivot calibration [21]. Orientation of the Cartesian stage expressed in the coordinate frame of the tracker is also required. This is obtained by moving the Cartesian stage arbitrarily (maintaining a safe distance from the patient) while recording sensor readings. From these readings it is straightforward to extract Cartesian stage orientation with respect to the sensor frame whether or not the axes are orthogonal. If they are orthogonal (as is the case for us) direction cosines are a means to determine the orientation of the Cartesian stage with respect to the tracker.

2.2.2 The Virtual RCM: A Heuristic Search

Since operating room time is costly, a key performance criterion for the Virtual RCM needle placement algorithm (in addition to accuracy and robustness) is fast convergence within a small number of cycles. In systems where the Virtual RCM algorithm is implemented (where the tool tip is not mechanically constrained to an RCM point), the roll and pitch DOF (α and β) are no longer decoupled, and thus cannot be optimized individually. A blind search of all possible α and β combinations is not useful for these coupled variables, because it would be impractical to repeatedly rotate the two joints a full 360° until the best alignment is determined from all possible discrete combinations of the two. To rapidly optimize α and β simultaneously we draw upon AI techniques, including heuristic-based breadth or depth first search techniques. We discretized each rotational DOF and partition our search space into two subspaces, one for each angle. A heuristic function guides the search to optimal needle alignment rapidly by deciding where to search next at each state. In practical terms this means that the robot makes incremental motions, and after each motion it uses the heuristic function to observe whether the needle is becoming more or less aligned. This enables the algorithm to determine which direction of motion is likely to cause better alignment. By continually moving both angles, the robot is able to rapidly converge on the proper alignment.

Selecting a heuristic function that quantifies improvement in needle alignment is not trivial. A desirable function should not have local minima that may cause the final alignment to converge at an incorrect solution. Another consideration is that the
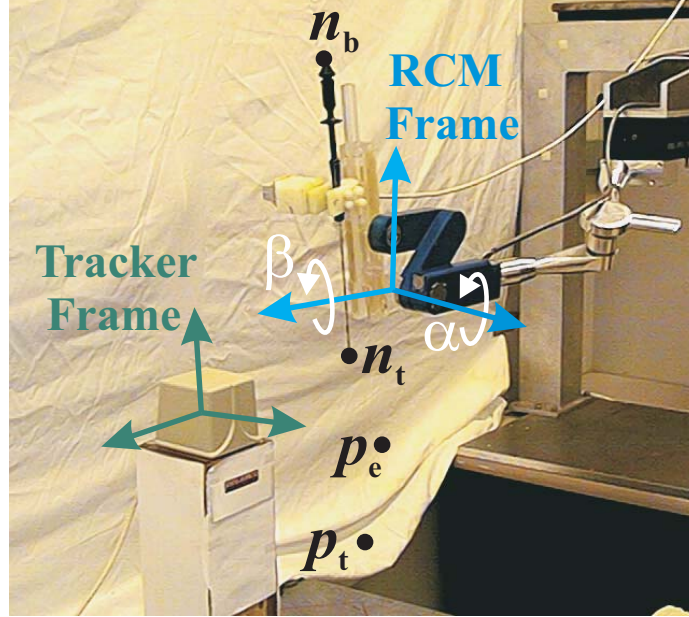
Figure 2.3: Illustration of frames and the points which define needle and entry vectors. These are used to build a simulator for candidate heuristic functions.

magnetic tracker (or any device that provides the pose of the needle) introduces some uncertainty. Therefore, a good heuristic function must have a low sensitivity to noise and it is important to consider error propagation in candidate heuristic functions.

2.2.3 Analysis of Candidate Heuristic Functions

One potential heuristic function is the cross product between the needle vector (see Figure 2.3, $n = n_b - n_t$) and the entry path vector ($p = p_e - p_t$). Minimizing the magnitude of the cross product between these two vectors yields a needle aligned with the entry path. Another potential heuristic function (assuming the tip of the needle is first placed at p_e, is to align the needle by minimizing the perpendicular distance between the target point and the line defined by the needle (d_{normal} in Figure 2.4) while maintaining the needle tip at the entry point.
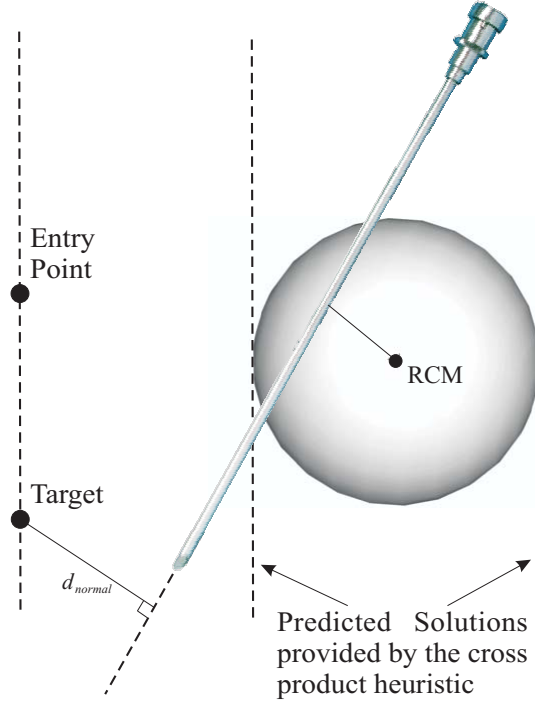
Figure 2.4: Illustration of the relationship between the needle, RCM point, and entry vector. As the needle moves, the normal vector from it to the RCM point traces out a sphere. The cross product heuristic can lead to needle alignments on either side of the sphere that are parallel to the entry vector. An alternative heuristic is d_{normal} as pictured.

In order to compare different heuristic functions, we built a simulator reflecting our robot. In the simulator we define a frame based at the RCM point and aligned with robot Cartesian frame (see Figure 2.3), in which the needle base and tip points are expressed. Planned entry and target points are expressed in the tracker frame. The transformation between these two frames is $F_{\mathrm{rcm}}^{\mathrm{tracker}}$. Note that this transformation is not required in the physical system since the needle is already expressed in the tracker frame, but is assigned a value here for simulation purposes. The needle vector in the RCM frame (note that needle tip is not at the RCM point) can be transformed to

tracker frame by,

$$n^{\text{tracker}} = F^{\text{tracker}}_{\text{rcm}} R_x(\alpha) R_y(\beta) n^{\text{rcm}}, \tag{2.1}$$

where α and β are as defined in Figure 2.1 and the notation $R_{\text{axis}}(\text{angle})$ indicates a rotation of magnitude "angle" about "axis". Candidate heuristic functions tested in this simulator were the cross product heuristic,

$$c = \|n \times p\|, \tag{2.2}$$

and the distance heuristic,

$$d_{\text{normal}} = \left\| v - (v \cdot n) \frac{n}{\|n\|} \right\|, \tag{2.3}$$

where all vectors are expressed in the tracker frame and $v = p_{\text{t}} - n_{\text{t}}$.

There are a number of reasons the cross product heuristic is preferable to the distance heuristic for creating a Virtual RCM, as will become clear in the simulation results presented in the next section. The distance heuristic requires the needle tip to be placed at the insertion point (eliminating some desirable alignment methods discussed in section 2.4), while the cross product heuristic function is applicable anywhere in the robot workspace. Further, the cross product heuristic is less sensitive to sensor error, as illustrated in simulation in the next section.

2.3   Simulation Results

In simulation, all discrete combinations of α and β can be plotted with respect to the value of a heuristic function. Figure 2.5 shows the simulated needle as α is rotated a full 360° while β is held constant at 5° and 50°. This procedure is repeated

for each β value. Plots of two heuristic function results across the entire $\alpha - \beta$ space can be seen in Figure 2.6. As can be seen from the figure, the cross product heuristic has a higher specificity than the distance heuristic. Its deep minima will yield a more accurate alignment result in the presence of sensor noise or other real world uncertainties than the shallow minima of the distance heuristic function.
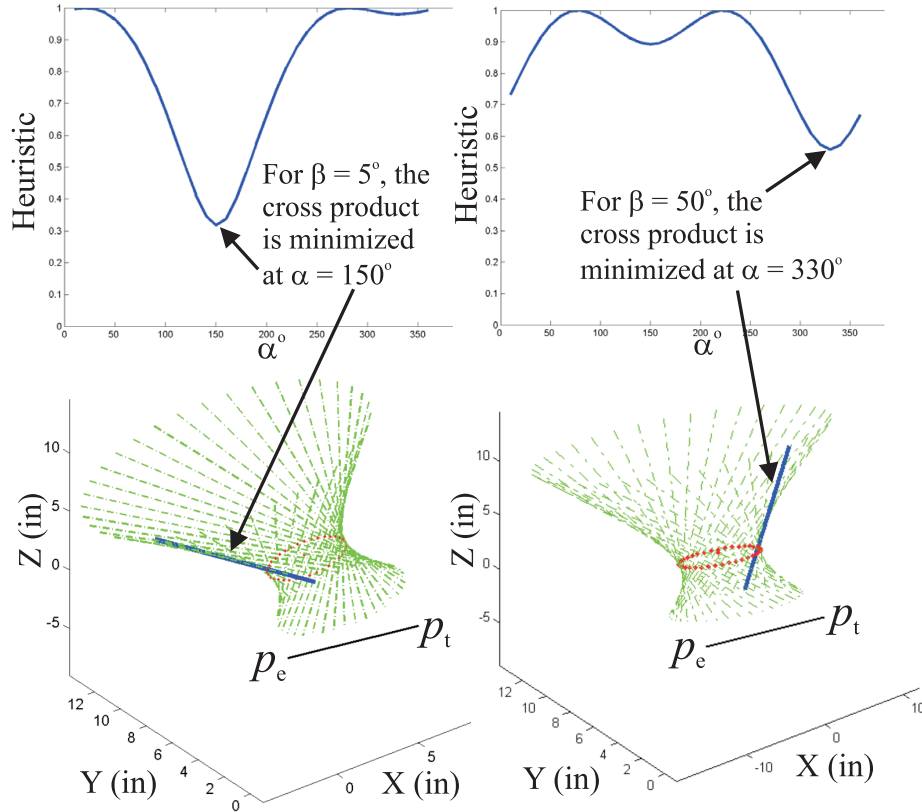
Figure 2.5: 360° rotations of α for two particular β angles to illustrate coupling between α and β.

It is not necessarily obvious which of the four minima of the cross product are acceptable solutions. Two can be discarded immediately, because they represent the needle being oriented the wrong way, with the base toward the target. The other two minima are equally good solutions, representing the needle being aligned on either
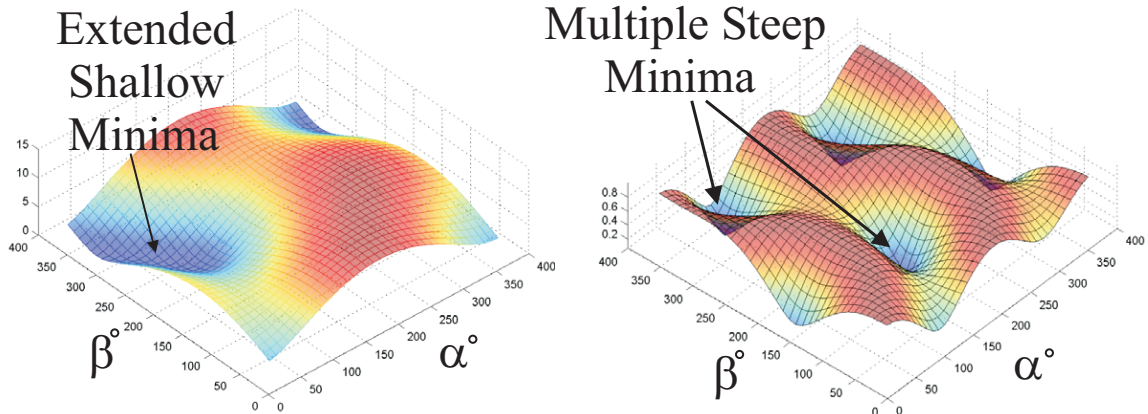
Figure 2.6: Plot of distance (left) and the cross product (right) heuristic functions for all angular values.

side of the actual RCM point as shown by the dashed lines on Figure 2.4. The only potential reason for choosing one over the other would be application-specific task or workspace constraints, since both represent equally good alignment of the needle. If no such task constraints exist, this multiple solution property of the cross product heuristic function is beneficial to the speed of the algorithm. A search of a multiple solution space can generally converge more quickly than a search for a single solution.

The most compelling advantages of the cross product heuristic are its spatial invariance (no dependence on Cartesian position) and its insensitivity to sensor noise. Spatial invariance has important practical implications in that it enables multiple procedural options for the needle alignment task as described in the following section.

2.4   Experimental Implementation

The two rotational joints of the robot shown in Figure 2.1 perform needle alignment using the cross product heuristic function. The joints are moved in small incre-

37

ments. Since the tool tip is not on the mechanical fulcrum point, it will be displaced a small amount during each rotation. However this displacement is immediately compensated for by the Cartesian stages, based on the tracker reading. Thus the needle tip remains on a Virtual RCM point. The robot continues to move through the search tree by moving the rotational joints alternately in incremental motions that decrease the value of the heuristic function.

There are several ways to apply this algorithm in needle placement (Figure 2.7). The most obvious is to perform needle placement using the same sequence of motions as would be done manually (the "Virtual RCM" method), where the robot first moves the needle tip to the entry location, and then aligns it along the insertion vector. Humans do not orient the needle first and then move it to the entry point, although this is an equally good order of operations. (Perhaps the reason is that humans are able to discern smaller differences in vector alignment between nearby vectors than those separated by some distance. It may be easier for humans to control alignment accurately by pivoting on a fixed point.)

A robot can perform alignment before moving the needle to the surgical site (the "Align/Move" method). The advantage of this is speed. Since the robot is a safe distance from the patient, eliminating the Cartesian correction portion of the Virtual RCM algorithm allows faster convergence to the correct alignment. A third alternative is to use a combination of the first two methods (the "Hybrid" method). The robot can rapidly make a quick rough alignment using the Align/Move method, then fine-tune alignment with the Virtual RCM method once at the entry point. Figure 2.7 presents a flow chart of all three methods.
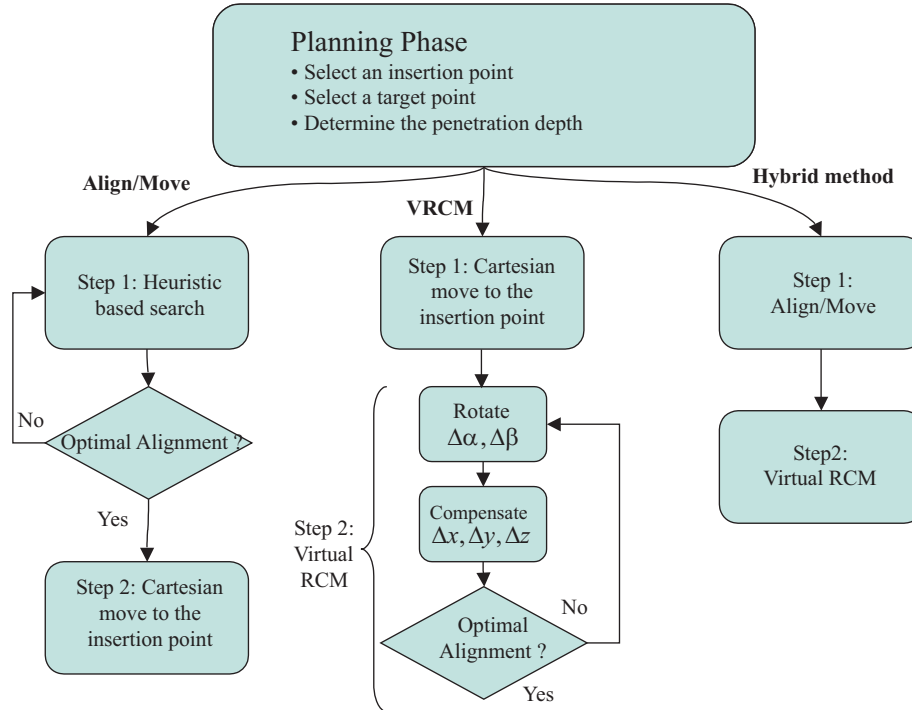
Figure 2.7: A flow chart of several ways needles can be aligned using Virtual RCM algorithms. One can align the needle before moving it to the insertion point, or one can move it first and then align it (denoted "VRCM" above). A third Hybrid Method involves performing the other two methods sequentially.

2.4.1 Results and Discussion

We performed needle placement according each of the three methods, and the results are summarized in Table 2.1. In our experiment, the number of steps required (regardless of the method used) was nearly linearly proportional to the initial misalignment. This was because we used a fixed initial (largest) step size. If the initial step size was large and adaptively modified as the solution was approached, the algorithm could reach a solution in fewer steps. However, this would only be practically feasible for safety reasons in the Align/Move or the Hybrid Methods, when the needle is far from the patient. In our experiments it was possible, given a wide range of

initial conditions, to get an optimized solution within a few (20–30) steps requiring a total time of only 0.8–1.2 sec, since each step requires an average of 40ms.

As can be seen from on Table 2.1, Align/Move is the fastest (fewest steps required) of the three methods, because there is no Cartesian motion needed to compensate for tip displacement. The results for Virtual RCM show that it alone is essentially equivalent to Align/Move in both rotational and displacement accuracy, yet much slower. The Hybrid method is much more accurate than the first two, yet the algorithmic complexity has the same order of magnitude as Align/Move. It is important to note that the accuracy presented in the table is severely limited by the tracker accuracy, which is reported by the manufacturer as 2.54 mm RMS (this is a first-generation FOB tracker).

	Experiment Sets		Set I	Set II	Set III
Method	Initial angle deviation (deg)		15.6	28.7	51.4
	Initial target displacement (mm)		21.2	41.8	118.2
Align/Move	# of steps	Rotation	17	35	66
		Translation	1	1	1
	Angle error (deg)		2.2	2.8	2.1
	Target displacement (mm)		1.05	2.81	3.40
Virtual RCM	# of steps	Rotation	17	35	66
		Translation	17	35	66
	Angle error (deg)		2.8	2.2	2.8
	Target displacement (mm)		1.68	3.02	5.15
Hybrid Tech.	# of steps	Rotation	Method I	17	35	66
			Method II	2	2	3
		Translation	2	2	3
	Angle error (deg)		1.4	1.7	1.9
	Target displacement (mm)		0.78	2.44	3.99

Table 2.1: Experimental Results.

2.5 Conclusions

This chapter has described the Virtual RCM algorithm for aligning surgical tools along desired entry vectors. The Virtual RCM is applicable to both straight needles and curved tools like the steerable needles and active cannulas described in the next two chapters. The Virtual RCM has the potential to make surgical robots easier to set up, calibrate, register, and use in the operating room. Addressing these issues is a key to bringing the many laboratory-demonstrated advantages of needle placement robots (notably enhanced accuracy and precision, which are directly correlated to clinical outcome) to bear on what have to date been manual hand-held tool alignment procedures. The Virtual RCM is an incremental adaptive motion control cycle for robotic alignment of the needle with the desired entry trajectory. Key features of the Virtual RCM are that it can be carried out with direct image-extracted robot pose measurement, requires minimal calibration, does not require encoding (potentially allowing encoders to become redundant safety features), can tolerate unknown transformations (e.g. passive positioning arms) in the kinematic chain, and that it removes the requirement that the tool be coincident with a mechanically enforced RCM. Our proof-of-concept prototype system achieved 0.78 mm translation and 1.4° rotational accuracy (which is within the tracker accuracy), from the an initial error of 15.6° and 21.2 mm, within 17 iterative steps (0.5-1secs).

A future goal in Virtual RCM research is to replace the magnetic tracker with a CTF scanner, sensing the pose of a site on the robot directly from CTF images using the method described in [114]. The long-term goal is to clinically accurately

place needles using inexpensive, safe, and easy to use robots in a variety of intraop-erative imagers (e.g. CTF, MRI, fluoroscopy, etc.) using purely image-based spatial registration. In terms of algorithmic enhancements, we hope to incorporate target uncertainty into our algorithm in the future.

The Virtual RCM described in this chapter (published in [23–25]) has subsequently successfully been applied to needle placement in both phantom studies and animal models [18,19], and used in conjunction with 3D US reconstructed from a magnetically tracked 2D US probe [23]. Subsequent experiments comparing the image-guided robot system to the accuracy of current clinical needle placement technique have been submitted for publication [20]. Both the experimental results presented in this chapter and these subsequent positive clinical and imager-integration results demonstrate the usefulness of the algorithm. It is well-suited for use in initial animal studies and clinical trials with steerable needles and active cannulas, the design and modeling of which are the topics of the following chapters.

Chapter 3

Steerable Needles

Needle insertion is a critical aspect of many medical diagnoses, treatments, and scientific studies, including percutaneous procedures requiring therapy delivery to, or sample removal from, a specific location. As described in Chapter 2, the success of needle-administered therapy and diagnosis depends on the accuracy of final tip position, which motivates the use of needle alignment robots and algorithms like the Virtual RCM. However, while accurate initial alignment is clearly important, even perfect alignment cannot guarantee accurate tip placement. Many factors influence the needle after entry (e.g. tissue inhomogeneity, deformation, membrane puncture, patient motion, etc.), causing deviations from the intended trajectory. Thus, acquiring the intended target with sufficient accuracy may not be possible, or may require multiple withdrawals and reinsertions of the needle causing additional tissue damage. While deviations from intended trajectory can often be visualized, they cannot be compensated for during insertion without a means of control or "steering" of the needle inside tissue during insertion. Steering can also enable obstacle avoidance and

permit access to targets inaccessible via straight trajectories. This chapter describes a means of robotically harnessing natural bending forces arising from the standard asymmetric bevel-tip to controllably deflect flexible needles within tissue media to enable needle steering. We address design considerations for both needle and robotic actuation system, and kinematic modeling, performing a set of experiments to fit and validate the model. Experiments also examine the effect of particular needle design parameters and insertion strategies on steerability. The kinematic model generalizes versions of standard three degree-of-freedom (DOF) nonholonomic unicycle and bicycle models to six DOF using Lie group theory. This provides a foundation for path planning and closed-loop, image-guided control. In this chapter we also investigate teleoperation as a first step toward clinical adoption of steerable needles, since direct participation often appeals to physicians. The kinematic model has formed the foundation for recent closed-loop control, planning, and design studies by our research group and others, which are surveyed in the chapter conclusions section. Promising initial results in planning and control indicate that an automated steerable needle system may one day exceed the accuracy not only of current free-hand insertion, but also that achievable via robot-assisted preinsertion alignment, and even that of teleoperated steerable needles under the control of human operators. We anticipate that a system where the clinician controls some degrees of freedom while others are automated may strike the best practical balance between accuracy and human factors considerations.

The work presented in this chapter has been published in [121, 143, 175–177], and relevant portions are patent pending [180]. It has also laid the foundation for many

further studies by others, which are surveyed in Section 3.6.

3.1 Motivation and Related Work

While needle-steering techniques are applicable to nearly all needle insertion procedures, the prostate, liver, and brain provide specific examples of organs where treatments might be improved by steerable needles. There are significant engineering challenges associated with generating steering capability in needles, stemming from the very small size of the needle, the required working channel through its center, and the diversity and inhomogeneity of tissues in which needles are used. Despite these challenges, several mechanisms have recently been proposed to enable needle steering within tissue. In the remainder of this section, we first motivate needle steering with three promising application areas, then describe the bevel-tip steering mechanism, and finally describe recent work on alternate mechanisms, comparing and contrasting them to bevel steering.

3.1.1 Medical Motivation for Steerable Needles

Needles are used clinically in nearly every area of the body, and are one of the least invasive mechanisms for surgical treatment. Three compelling initial application areas for needle steering include the prostate, liver, and brain; these examples illustrate ways in which needle steering might address difficulties observed by surgeons using traditional straight, rigid needles, thereby improving targeting, enabling novel treatment methods, and/or reducing complication rates.

Prostate. Needle biopsy for diagnosis of prostate cancer is performed on about 1.5 million men per year and one in six men in the United States will be diagnosed with this condition at some time in their lives [92]. A common treatment option is transperineal brachytherapy [17], involving implantation of thin needles to deposit radioactive seeds [43]. In these procedures, it is challenging to achieve precise targeting in the event of organ dislocation and deformation. Significant seed-placement error can occur if the needle is tangential to the prostate capsule wall upon penetration [173]. Hence, the ability to steer the needle and bevel to an optimal capsular penetration angle is of particular importance. After penetration, steering within the prostate may be useful for correcting the combined effects of deflection, dislocation, and deformation of the organ observed (but difficult or impossible to correct) in contemporary practice.

Liver. Hepatocellular cancer is one of the most common cancers in the world, and also one of the deadliest. Without treatment, the five-year survival rate is less than 5%, and the incidence is rising [168]. The liver is also the most frequent location of secondary tumors metastasized from colorectal cancer, with about 130,000 new cases and 60,000 deaths annually in the United States alone [125]. Liver tumors smaller than 5–6 cm in diameter are often treated with thermal ablation administered at the tip of a needle inserted through the skin and visualized using ultrasound. Since liver tumors often have very different mechanical properties than the surrounding tissue, they can behave as if encapsulated with respect to needle penetration, presenting challenges similar to those of the prostate. Also, "all but the smallest [liver] tumors" [122] are large enough to require multiple overlapping thermal treatments for full

coverage. Currently each treatment requires removing and reinserting the needle. If it were possible to partially retract, steer, and redeploy the needle into an adjacent treatment zone, some targeting uncertainty and additional puncture wounds might be avoided.

Brain. In brain tissue, steerable needles might be used to stop the flow of blood from an intracranial hemorrhage (ICH), and remove resulting clots via targeted drug injection. The incidence of ICH is in the range of 10–20 persons per 100,000, and untreated clot resolution takes two to three weeks, with an exceedingly high mortality rate of 50–75%. It is suggested that ultra-early intervention, given within three to four hours of onset, may arrest ongoing bleeding and minimize swelling of the brain after ICH [120]. Precisely steered delivery vehicles have the potential to increase drug-target interactions and may enable very rapid removal of clots. In a typical emergency setting, a non-specialist surgeon free-hand drills a burr hole to introduce a device for injecting such drugs. The surgeon's hand-eye coordination limits the location and alignment accuracy of the burr hole, and it may be misaligned by as much as 20–25°. To compensate, the burr hole is usually made significantly larger than the diameter of the interventional tool, and this can lead to subsequent technical and clinical complications. Steerable devices may allow this hole to be much smaller, since steering can compensate for initial alignment error.

3.1.2 Bevel Steering Mechanism and Model Intuition

Physicians who have performed needle insertion know that needles with standard bevel tips (the most inexpensive and common tip design) tend to deflect as they are inserted due to tip asymmetry. The angle of the bevel generates forces at the needle-tissue interface that causes the needle to bend as it is pushed into the tissue. While such bending is reduced in clinical practice by making the needle shaft as stiff as possible (usually out of stainless steel), the bevel (along with many other factors) can still cause clinically significant placement error. Some physicians have learned to exploit such bevel induced "error" to combat other sources of error by steering the needle using a combination of translation (insertion) and axial shaft rotation. However, this approach requires excellent 3D spatial reasoning, extensive experience, and high-resolution, real-time image feedback, and the amount of bending achievable is severely limited by the high stiffness of the steel needle shaft.

In this work, we enhance and magnify the bevel steering effect by making the shaft of the needle more flexible. We then use a robot to actuate the input degrees of freedom of the needle. With suitable model-based control techniques, a robot will be able to drive the needle tip to a desired target or along a desired path. To facilitate this, we wish to express the shape the needle will take in terms of the input degrees of freedom.

We consider the bevel tip needle as a nonholonomic system with a steering constraint. There are clearly directions in which the tip may not instantaneously move when embedded in tissue. Similarly, the wheels of a bicycle or unicycle cannot in-

stantaneously move sideways, despite their ability to attain any desired pose in the plane through a sequence of motions. This is intuitively analogous to retracting the needle a certain distance, reorienting the bevel tip, and then pushing it forward again to achieve motion in a direction that would have been instantaneously impossible. Thus, we model the needle as a nonholonomic system, that is to say, one with nonintegrable velocity constraints [123]. Such systems are path dependent, so determining the necessary set of inputs to reach a desired final configuration is not necessarily straightforward. However, nonholonomic motion planning and control have been studied extensively in the robotics and control literature, making a large body of work available for future application of our model. Within this framework, it can be shown that the system is controllable and can reach any desired pose, given a sufficiently large environment.

3.1.3 Related Work

Early work in needle modeling and simulation involved recording the forces applied to a needle during insertion and playing back "haptic recordings" or simple force versus position models in a force-feedback virtual environment [29,70,86]. More recent work has modeled both tissue deformation and needle-tissue interaction forces. The geometry of the soft tissue for modeling and simulation purposes is now typically defined using a mesh composed of 2D or 3D polyhedral elements [66]. The simulated forces exerted by the needle are used to compute deformations of the soft tissue mesh. Most past work using this approach has approximated the needle as infinitely thin

and rigid [8,52], although some researchers have modeled needle geometry (thickness) and its effect on friction [128].

Simulating needle insertion for medical procedures typically requires as input the properties of the needle and the soft tissue in which the needle will be inserted. DiMaio and Salcudean performed pioneering work in measuring and simulating the deformations that occur during needle insertion [52,54]. A robot instrumented with a force sensor inserted a needle into 2D gel and deformations captured with video and image processing. Using a quasi-static finite element method based on the acquired material parameters, they simulate the insertion of a rigid needle. Alterovitz et al. proposed an alternative dynamic 2D model based on a reduced set of scalar parameters such as needle friction, sharpness, and velocity [8]. For a given kind of surgery, such as prostate brachytherapy, this allows the needle designer to choose optimal parameter values (within limits) to improve needle placement accuracy. This model has allowed collaborators to produce interactive simulations and analyze the sensitivity of current medical methods to these parameters. In both of the simulators described above, the models considered only symmetric needle tips. Other researchers, including Mahvash and Hayward [119] and Nienhuys and Van der Stappen [127], have integrated cutting into simulations. However, cutting by needle tips has yet to be addressed through experiments or complete simulations. There has also been some previous work on planning curved paths for curved, rigid needles [129].

Determining Parameter Values

Setting accurate parameters for tissue properties is important for realistic needle insertion modeling in deformable tissues. Krouskop et al. estimated the elastic modulus for prostate and breast tissue using ultrasonic imaging [111]. Kataoka et al. separately measured tip and frictional forces during needle insertion into a canine prostate, which is useful for simulation validation [105]. Okamura et al. measured the stiffness, cutting and friction forces occurring during needle insertion into a bovine liver [131]. Tissue properties can also be taken from handbooks [64, 84], or measured during procedures [28, 191]. Unknown parameters for needle insertion in some simulators (e.g. [8, 9, 11]), were set so that the output closely resembles an ultrasound video of a physician performing prostate brachytherapy on a patient.

Needle Bending

The effects of needle bending have been explored by several groups. O'Leary et al. [133] experimentally demonstrated that needle bending forces are significantly affected by the presence of a bevel tip, but did not generate a model for this behavior. Kataoka et al. [104] created a model for needle deflection that does not include bevel effects. They also note that they believe the bevel to be the main source of deflection in bevel-tip needles. DiMaio and Salcudean [53, 54] and Glozman and Shoham [68, 69] created finite element-type models for needle bending; their application to steering is described in more detail below.

Needle bending can also be generated using different strategies. One promising

51

strategy incorporates a prebent stylette inside a straight cannula as was proposed by Okazawa et al. [132]. The further the flexible curved stylette is extended from the stiffer outer cannula, the greater the curvature as the needle is inserted. Direction can be selected by axial stylette rotation. The maximum curvature attainable by such a design has yet to be determined, and doing so will require careful study of the relative stiffnesses of stylette, cannula, and surrounding tissue. The cannula must be stiff enough to straighten the curved stylette when the stylette is retracted, yet flexible enough to allow the needle to bend into a curved trajectory. Changes of the direction of curvature (e.g. 'S' or 'corkscrew' shapes) may be possible with this design, but have yet to be demonstrated. Okazawa, et al. also leave 3D kinematics and planning to future work, focusing their initial efforts on planar inverse kinematic planning using a single bend of the needle. Another similar prebent element design is a telescoping double cannula where the internal cannula is prebent [48]. This and several other designs that incorporate curved cannulas [65, 118, 145] are more closely related to the active cannulas of Chapter 4, and are described in detail there.

Robotic Alignment and Steerable Catheters

In order to steer a flexible bevel-tip needle, we have developed two specialized needle insertion robots. As described in Chapter 2, the idea of using robotic systems to insert needles is not new; many researchers have demonstrated improved targeting by utilizing the inherent stability, accuracy, and registration abilities of robots. A robot is better able than a human to translate information from medical images to 3D physical locations, and then to precisely align a needle to a target [155]. These

systems generally seek to increase the accuracy of the initial alignment of the needle (prior to insertion) as a means of reducing final targeting error. However, they do not address some of the most important factors contributing to targeting error, needle deflection after insertion, and target motion from tissue deformation and patient movement. None of the systems described in Chapter 2 is able to offer accurate control of the needle path after entry into the body. A steerable needle will also have less stringent requirements on initial alignment accuracy, allowing accurate targeting without precise or perfectly calibrated alignment robots. This contributes to the objectives of Chapter 2, namely reducing cost enhancing ease of use, making needle placement systems more suited to practical application in the clinical setting.

We note that the idea of actively steering a surgical tool after insertion into the body has received interest for the purpose of catheterization. Designs using shape memory alloys [78, 117], as well as electro-active polymeric actuation [76] have been proposed. However, these systems are more complex and expensive than needles, and are not typically designed to cut through tissue.

Robotic Steering With Bending

There are only two recent studies that have analyzed robotic needle steering using bending and path planning. First, DiMaio and Salcudean [53, 54] formulate a needle Jacobian that describes tip motion due to needle base motion and a tissue finite element model. Their needle is stiff relative to the tissue, and steering is accomplished by pulling on and angling the needle shaft outside the body to cause the tissue to deform. Our approach contrasts theirs in that we consider a system where the needle

is very flexible relative to the tissue, and does not displace a large amount of tissue in order to steer itself. Second, Glozman and Shoham [68,69] use an approach similar to DiMaio and Salcudean, but suggest a simplified model that allows fast path planning and real-time tracking for needle insertion procedures. Neither of the studies above consider the effect of tip asymmetry on steering, and both use standard stainless steel surgical needles, which are less flexible than the Nitinol needles considered in this chapter.

The above method of steering via deforming tissue with a traditional stiff needle appears able to generate a large steering capability at shallow depths, but this ability is reduced as depth increases [68]. More tissue must be deformed to generate steering, and more force must be applied to the tissue. Since there is clearly a limit on the maximum force that can be applied without tissue damage, there will be a corresponding depth where it is no longer possible to steer using this method. In contrast, while bevel steering and prebent element methods may generate somewhat less steering at shallow depths (no study exists comparing such steering amounts), their steering ability is not affected by depth, and they do not require large force application or tissue deformation to achieve steering. Ultimately, we expect that a combination of force application at the needle base (the method of DiMaio and Glozman) and our bevel-steering techniques will be most successful in enhancing and controlling needle insertions into human soft tissues.

To fully model or simulate needle steering in soft tissues, it is necessary to model the effect of cutting with a bevel tip and needle bending in 3D. All current models we are aware of either approximate the needle as a rigid object, restrict the motion

of the needle to a 2D plane, or do not consider the effect of a bevel tip. These approximations may not be valid when the needle is very thin and flexible, as is the case in our specific needle steering system design, as well as in many medical procedures that seek to minimize tissue damage. Although the work described in this paper does not explicitly consider soft tissue deformation (we use a needle designed to be sufficiently flexible that it does not cause significant deformation in phantom tissues), our model can be integrated with simulators handling deformation [7], as is described in the discussion section.

Related work in Teleoperation

In addition to specific work on needle steering, there are a number of examples in the literature of robot-controlled needle insertion [155], many of which are commanded with simple computer interfaces such as mice, keyboards, and joysticks. The input devices in this prior work differ from our system because they are used to control the orientation of the needle *before* it is inserted into tissue, and only move the needle along its axis after insertion. There are also teleoperation systems for robot-assisted catheter insertion, e.g. Hansen Medical, Inc. (Mountain View, CA, USA), which do not operate under the same kinematic constraints as our needle steering system.

Our needle steering teleoperation work is more closely related to teleoperation of nonholonomic systems, such as wheeled mobile robots. Researchers have developed control methods for telemanipulation of mobile robots with joysticks, e.g. [67, 124]. In these systems, the input degrees of freedom (typically left/right and up/down) are not kinematically similar to the mobile robot motion (e.g. they might adjust wheel

speeds for a 2-wheeled, skid-steered mobile robot). In this chapter, we match the needle insertion degree of freedom to translational motion of the master stylus, and the needle spin degree of freedom to the spin of the stylus. As far as the author is aware, there is no prior work comparing different degrees of freedom of operator control versus autonomous control for teleoperated nonholonomic systems.

3.2 Design Considerations

Before describing kinematic models of needle shape in tissue, we will describe the design of the needle steering system. This section describes various tradeoffs in actuation, drawing on examples from two actuation units that we have constructed. It also experimentally examines the effects of insertion velocity and bevel angle on needle steering.

3.2.1 Robotic Devices for Needle Steering

Automated insertion of flexible needles is challenging because the needle will buckle if not supported near the tissue entry point. However, automation appears necessary because many of the requirements for flexible needle steering (e.g. prevention of buckling, accurate 2-DOF velocity control, stabilization of other DOF to avoid unintentionally applying base forces and torques), seem beyond human ability. In this section we present two different robotic devices for steering needles using tip asymmetry. Each device is able to control insertion velocity and the rotation (spin about the needle axis) velocity. We do not consider devices for lateral motion of the
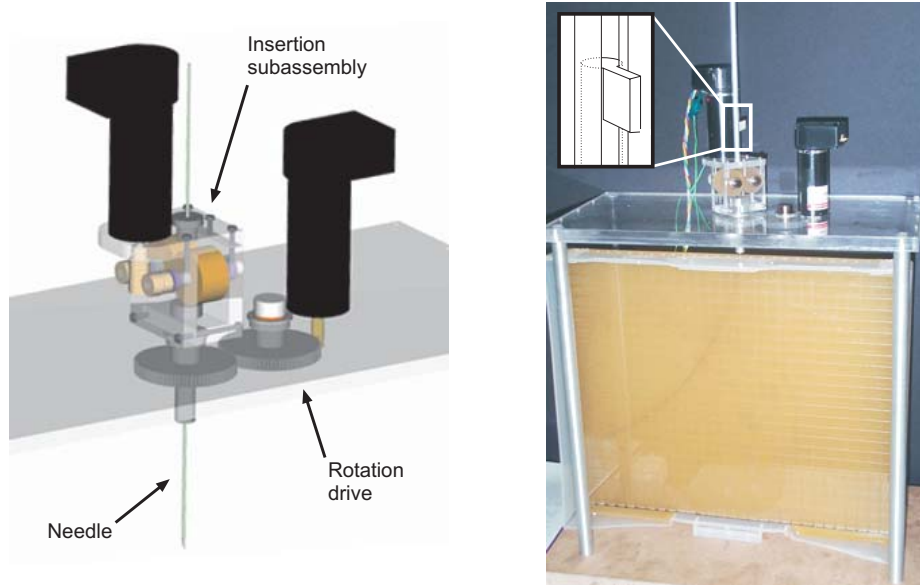
Figure 3.1: (Left) CAD model of a friction drive needle insertion mechanism for steering of flexible needles. (Right) Experimental setup using a friction drive needle insertion mechanism for steering of flexible needles. Inset line drawing shows the needle base in the slotted needle guide that prevents unintended axial needle rotation.

needle base here, but note that it can be readily achieved by mounting our devices on a higher-DOF manipulator (e.g. those described in Chapter 2), in order to combine a variety of needle steering methods.

Friction Drive

The first device designed was based on a friction drive concept. There have been other needle insertion devices incorporating friction drive, notably a novel robot for percutaneous access to the kidney (PAKY) [154]. In that system, the goal was to provide a radiolucent driving mechanism and direct control of only insertion velocity. Our system consists of a friction-drive insertion subassembly, which is then rotated to generate spin about the needle axis. The device is shown in Figure 3.1.

In this device, the insertion subassembly drives the needle by grasping it on the
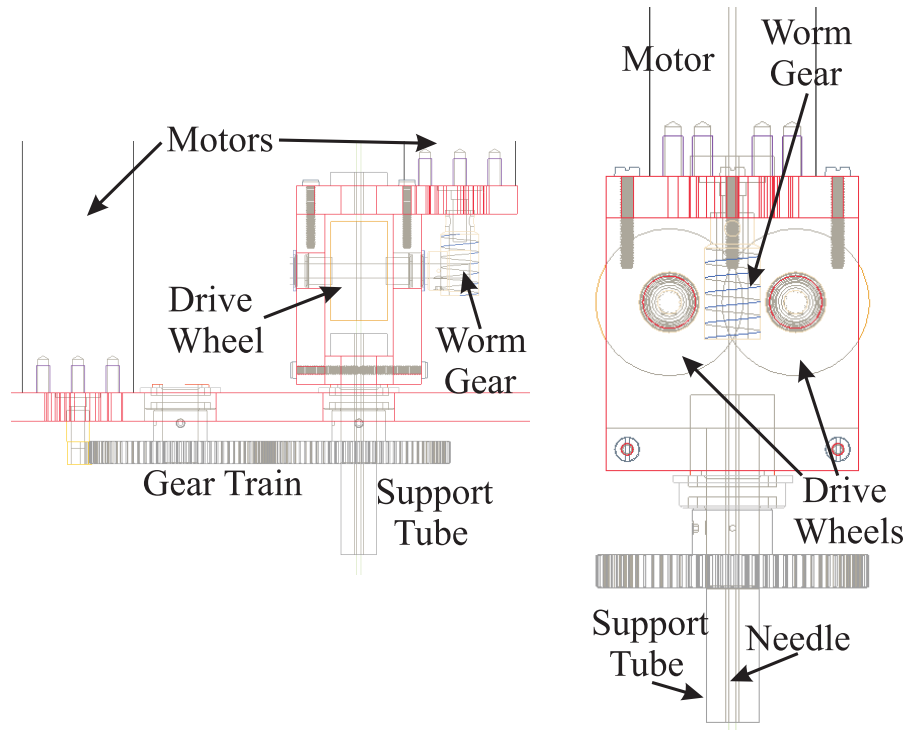
Figure 3.2: CAD sketches of the friction drive design shown in Figure 3.1 for inserting flexible, steerable needles.

barrel using two opposing rubber wheels actuated by a worm gear attached to a motor. Rotation of the needle about its axis is achieved by rotating the insertion subassembly as a unit. Since the wheels grasp the needle tightly by the barrel, rotating the subassembly causes the needle to rotate as well. A slotted needle guide shown in the photograph in Figure 3.1 further fixes the orientation of base of the needle, and thus the bevel direction, relative to the drive wheels. This mitigates unwanted needle rotation as the drive wheels turn. Buckling is prevented by passing the needle through a 1.5 mm hole drilled through the aluminum rod that supports the insertion subassembly. This rod extends to the surface of the phantom tissue into which the needle is inserted. Sensing is accomplished using a single camera that captures images of the needle through a physical ground-truth 1 cm square grid (shown in Figures 3.1

and 3.8), laser etched into a clear polycarbonate sheet. This system was used for the kinematic model validation and parameter fitting experiments described in Section 3.3.

The main advantage of this friction drive mechanism is compactness and simplicity. However, a potential drawback is the possibility of slippage between needle and drive wheels. In experiments, such slippage was generally small, though noticeable. Thus, in experiments, absolute encoding of needle depth was accomplished not using motor encoders, but by manually recording needle base translation distance with respect to the slotted needle guide. Further, if rubber drive wheels are not perfectly cylindrical and wheel axes are not perfectly aligned, uneven wheel contact can impart axial torque, causing the needle to spin axially during insertion. (This spin is much more pronounced in [154], where there is effectively only one drive wheel.) Preventing unintended axial spin was the motivation for including the slotted needle guide shown in Figure 3.1, which compensates by fixing the angular orientation of the needle base with respect to the rotation subassembly.

With the friction drive, it is also difficult to instrument the needle to obtain force and torque measurements. While these have not been explicitly used in kinematics or control to date, it is expected that such information will be useful for future model enhancements, especially those accounting for the finite torsional stiffness of the needle. While potentially mitigated in real tissues by lubricating blood, needles in rubber phantoms exhibit high friction resulting in a difference in angle between the base (outside the tissue) and the needle tip (inside the tissue) when the base is rotated axially. Model-based planning and real-time control require estimates of

the tip angle, which may be obtained by observers (as described in the discussion section) or potentially facilitated by torque sensing and torsional models. To explore a different balance of design tradeoffs (sacrificing compactness to add sensing and eliminate the possibility of wheel slippage), a second device was designed.

Telescoping Support Drive

An alternative needle insertion actuation unit design involves driving the needle from the base while using a telescoping support sheath to prevent the needle from buckling. In this design, a needle rotation subassembly is moved by a translational lead-screw driven stage, as shown in Figure 3.3. The needle is attached to a motor controlling spin about the needle axis through a Nano-17 ATI force/torque sensor (Figure 3.4). This allows measurement of force along the needle axis and the torque about the needle axis. The translational stage used for linear insertion is a Velmex MA2524 linear stage with 20.5 inches of travel and a 2.5 turns/inch lead screw. It is actuated via a VEXTA PK266-03A stepper motor, which is operated by a Velmex VXM-1 controller.

The telescoping support sheath is created from the five segments of a disassembled radio antenna. Removing the friction couplings between the different segments results in a very low friction device. Figure 3.4 shows the antenna segments compressed near the entry point of the tissue. The inner diameter of the largest segment is 5.5 mm, while the inner diameter of the smallest segment is 2.3 mm. This smallest segment is inserted a short distance into a block of black Delrin (also shown in Figure 3.4). Upon exiting the support sheath, the needle passes through a 1.0 mm diameter hole
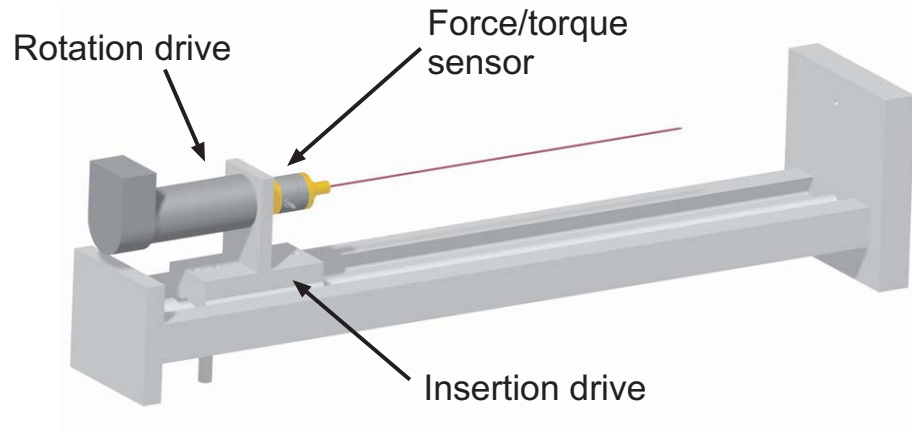
Figure 3.3: CAD model of a mechanism that allows telescoping support (not pictured) for steering flexible needles.

in the delrin block before entering tissue. This system is capable of delivering a 0.83 mm diameter needle perpendicularly to the surface of the phantom tissue without applying significant frictional forces. The friction force between the segments of the telescope was not measurable until the needle had been inserted a long distance into the tissue. When friction on the barrel of the needle presents sufficient opposing force to needle motion, the needle presses against the support sheath wall with sufficient force to noticeably increase the friction of the telescope sections sliding over each other. However, this does not result in any visible deformation of the telescoping support. Figure 3.5 shows the experimental setup using this needle insertion device. The support sheath was initially (in sections 3.2.4 and 3.2.5) compressed directly by the needle mount causing both needle and support sheath forces to be recorded by the force sensor. However, later a plastic shield to compress the support sheath was added to the rotation motor support plate, allowing the force sensor to measure only forces between the needle base and motor.

Sensing in this system was accomplished using calibrated stereo cameras placed
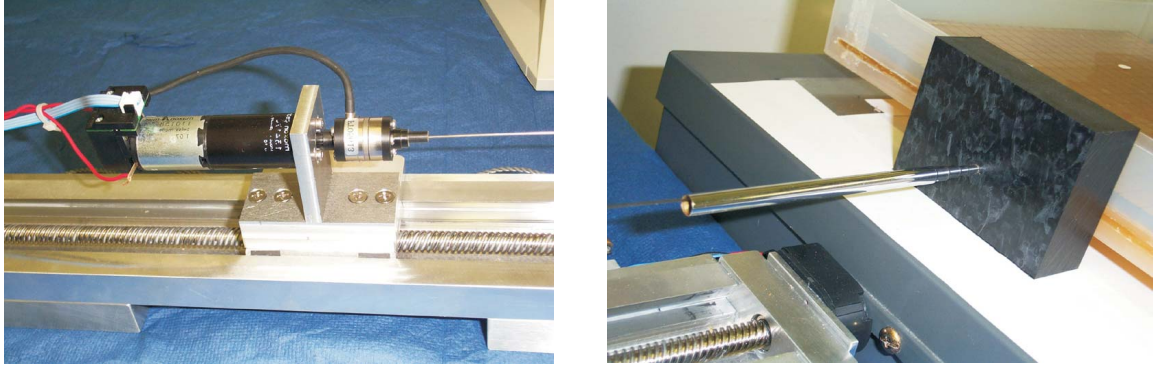
Figure 3.4: (Left) Needle rotation mechanism showing 6-axis force/torque sensor at needle base. (Right) Telescoping support sheath (compressed to show needle). A 1.0 mm hole in the black Delrin front block introduces the needle perpendicularly with respect to the tissue surface.

approximately 0.8 m above the horizontal surface of the tissue phantom. The cameras were calibrated using the Camera Calibration Toolbox for Matlab [27]. The cameras used were Sony DFW-V500 digital firewire cameras, and provided 640×480 pixel images at a rate of 7.5 frames per second. The actuation unit and sensing system described in this section was used for all experiments in Sections 3.2.4 and 3.2.5.

3.2.2   Teleoperation System

To enable direct human control of steerable needles, we extended the system in Figure 3.5 by (1) including the Freedom 6S (F6S) [51] haptic device (MPB Technologies, Inc.) as a master input device, (2) using higher resolution cameras for data collection (Sony XCD-X710 Firewire Cameras running with 1024×768 at 30 Hz), and (3) a third camera perpendicular to the phantom tissue surface for visualization. Shown in Figure 3.6, this extended system facilitated the teleoperation experiments described in Section 3.4. The F6S controls the two input DOF of the steerable needle according to the mapping shown in Figure 3.7. To teleoperate the needle steering
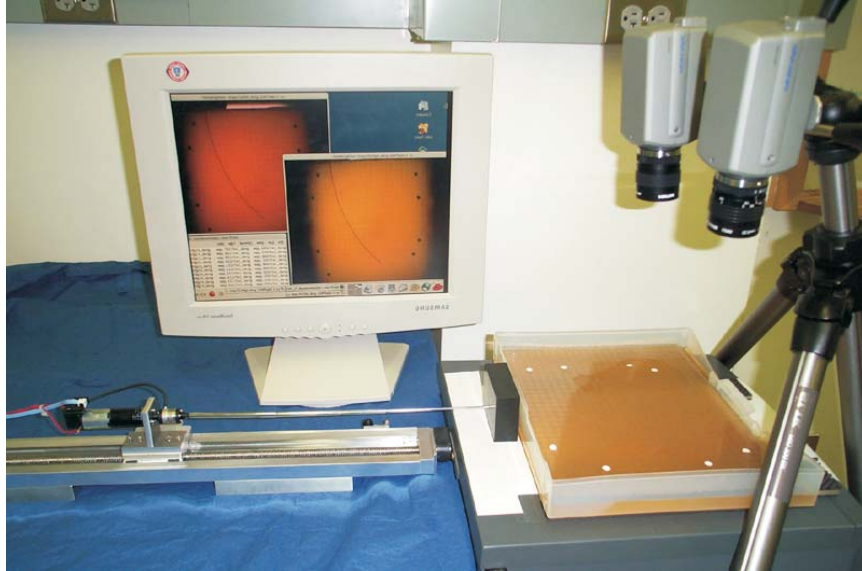
Figure 3.5: Experimental setup with telescoping support sheath, used for bevel angle and velocity experiments (Sections 3.2.4 and 3.2.5).

robot, the user grasps the pen-like stylus of the F6S. Stylus axial rotation is mapped to needle axial rotation, and the horizontal translation of the stylus (the x direction with respect to the F6S base frame) is mapped to the translation of the needle. Since the base of the needle cannot translate perpendicularly with respect to insertion direction, the F6S was similarly constrained in its y and z directions by virtual springs.

3.2.3 Experimental Design Considerations

In addition to appropriate robotic mechanisms, needle steering experiments require careful selection of needle and phantom tissue materials, calibration methods, and needle tracking algorithms. We note that although the experiments presented here are essentially planar, this system has the capability for three-dimensional experiments.
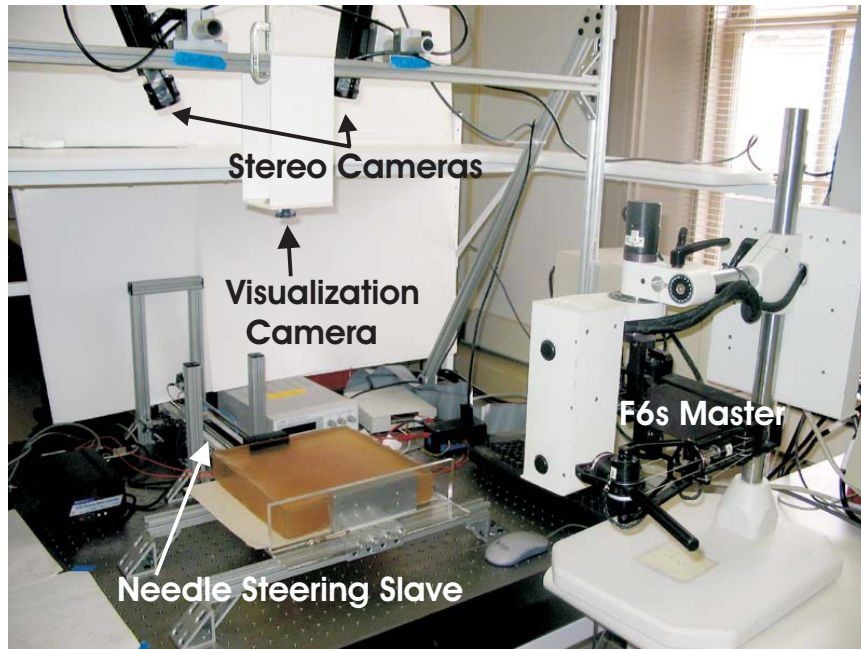
Figure 3.6: Complete needle teleoperation system. Components pictured include the slave telescoping support drive described in Section 3.2.1, the master Freedom 6S robot [51], calibrated stereo cameras to record needle position, and an overhead camera to capture images displayed to the user.

Needle and Phantom Tissue Selection

The amount of needle bending is related to material properties and diameter of the needle shaft, bevel angle of the needle tip, material properties of the phantom tissue, and friction forces between needle surface of the needle and the surrounding tissue. The ideal phantom tissue would closely approximate the material properties of human tissue, and simultaneously be transparent so that optical cameras can be used to collect tip data. While medical imagers like fluoroscopes would replace the optical cameras in a clinical setting, it is useful to use optical sensing in a laboratory testbed for safety and cost considerations. It is difficult to measure human tissue properties. They must be measured in living people, since ex vivo and cadaver tissues have significantly different properties than live tissues. Despite these difficulties, there have
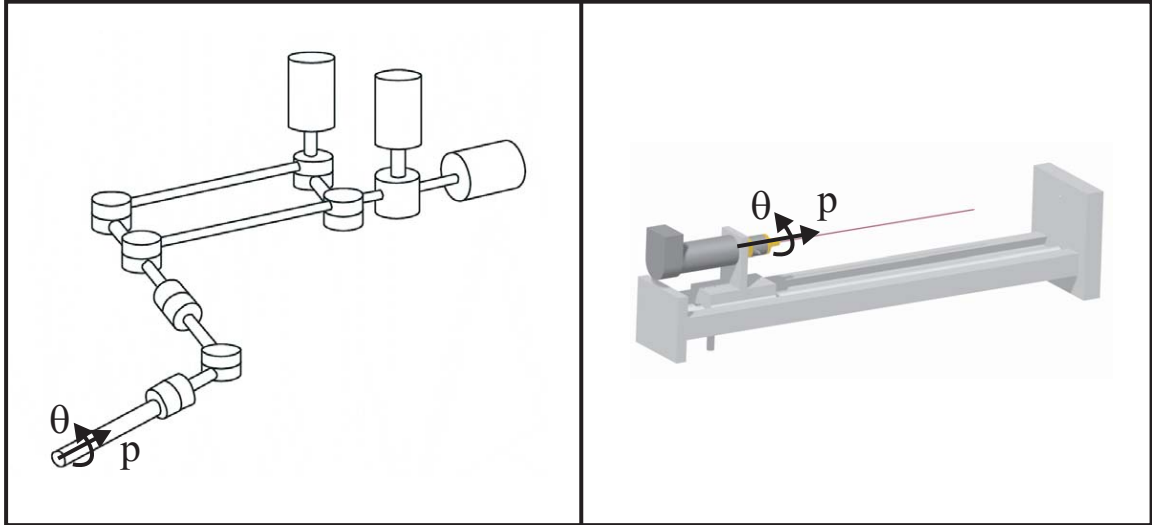
Figure 3.7: Correspondence of master robot DOF (left) and slave robot DOF (right) for teleoperation.

been some studies on in vivo animal tissue properties [30], and also on the mechanical properties of perfused ex vivo organs [106], which are expected to be more representative of living tissues than ex vivo organs without perfusion. Even if the properties of living tissues could be measured accurately there currently do not exist methods to recreate them in a phantom tissue. Thus Phantom tissues demonstrated to approximate all or nearly all properties of live human tissues have yet to be developed. However, there have been some attempts to replicate certain individual properties of human tissue. One of these is the Simulated Muscle Ballistic Test Media (Sim-Test) from Corbin, Inc. This rubber-like simulated muscle is particularly useful for needle insertion because it is fairly stiff (4.9 N/mm by a blunt indentation test), and yet has a comparatively lower friction on the barrel of the needle than many alternative rubber-like phantom tissues (e.g. silicone). It is also very easy to work with, reusable by recasting after melting at low temperatures (e.g. on a standard hot plate at low

heat). It is also non-toxic, and its stiffness can be modified by adding water while melted. Sim-Test further has a reasonable shelf life (several months) if enclosed in an air-tight container. The drawback of Sim-Test is that it is only semi-transparent. Thus, it is useful for experiments where the needle can be kept near the surface of the phantom tissue such as the planar experiments in Sections 3.2.4, 3.2.5, and 3.3.

Other phantom tissues have a different mixture of desirable and undesirable properties. Porcine Gelatin (Sigma-Aldrich, Inc. "Gelatin porcine skin for electrophoresis Type A") is transparent and well lubricated by suspended water (simulating the presumed effects of blood in real tissue), but has a very short shelf life (approximately one day with refrigeration) and its properties are likely temperature dependent, meaning that experiments must be completed rapidly, or a cooling system used during experiments. While porcine gelatin is non-toxic and manufacturing samples is straightforward (heat water, dissolve gelatin powder, allow to chill for several hours), it requires more time than Sim-Test, and samples are not reusable. One significant drawback of porcine gelatin is that it exhibits low strength. Needles embedded more than a few centimeters may shear through the gelatin (causing an effect similar to a wire-based cheese slicer). Thus, porcine gelatin was not used in any of the experiments presented in this chapter.

Other noteworthy phantom tissues include various commercial silicones and rubbers, such as "Super Soft Plastic" (M-F Manufacturing, Inc.). This material (and others like it) has the advantage of being transparent, but exhibits very high friction with the needle shaft, requiring large forces to insert needles beyond depths of approximately 10 cm. While not highly toxic, mixing such materials requires a fume

hood, and they are not reusable. An advantage is an exceptionally long shelf life (several months) without refrigeration or air-tight storage, although gradual leaching of an oil-based liquid does occur. This material is not suitable for experiments with the friction drive insertion device design, but can be used with the telescoping base-driven actuation unit, and is used in the teleoperation experiments in Section 3.4.

For needles to steer significantly through any of the media above, they must be flexible. One good candidate material for steerable needles is Nitinol, although other flexible materials may also be used (although they have not yet been explored). Nitinol, an alloy of approximately 55% Nickel and 45% Titanium, exhibits superelastic properties when properly heat treated. Nitinol has the additional benefit of being a bio-compatible material commonly used in stents and catheters, so it poses no danger of toxicity to the patient. Using Nitinol, needles of standard medical diameters (approximately 0.3–1.0 mm or equivalently 30–19 gauge, depending on the particular phantom tissue) exhibit bevel-steering ability in the phantom tissues above. Bevel angle also has an effect on steering, which we explore experimentally after discussing the calibration and data collection issues necessary for such experiments below.

Calibration of Needle Axial Angle

One of the most challenging practical considerations in attempting planar experiments was initial calibration of the orientation of the bevel tip about the needle axis. The small needle diameter hampers one's ability to accurately orient the bevel angle (Figure 3.9) by eye, especially considering that even a few degrees of error in initial
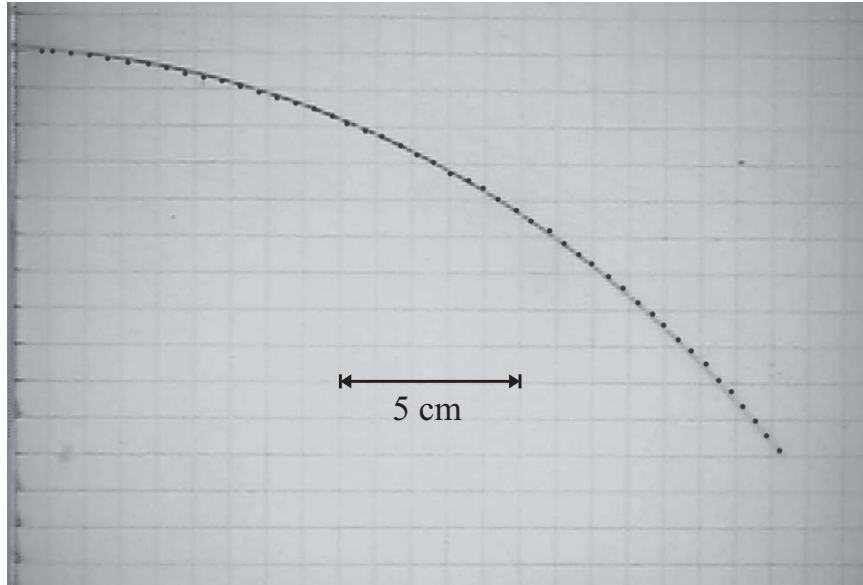
Figure 3.8: Tip positions during needle insertion shown overlaid on an image of the final needle path. Tip positions were extracted automatically from a sequence of insertion images.

rotation can cause the needle to move out of plane a centimeter or more over the course of a 25 cm insertion. One way to ensure that the bevel direction will create bending in the horizontal plane is to initially calibrate bevel angle as accurately as possible by eye, and then insert the needle several times. With each insertion, the out of plane motion is observed and corrected by appropriate small rotations of the needle between insertions. This is done until the needle can be inserted to its full depth without moving out of plane more than a few millimeters.

In practice, for an eventual commercial bevel steering system, we do not expect
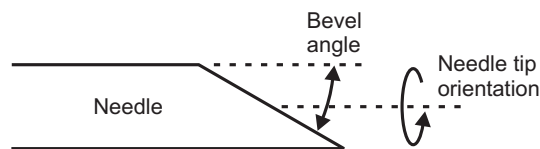
Figure 3.9: Definition of the bevel-tip angle and needle orientation.

68

this calibration issue to be problematic. When needles are produced in quantity, it should be straightforward to manufacture them such that the bevel is cut at an axial orientation accurately known with respect to a base fixture that remains part of the needle. This base fixture will enable the needle to be attached to the robot at a repeatable and known angular orientation. In our prototype system, no base fixture was included, so there was no means available to reproduce the exact axial angle of attachment between robot and needle. This necessitated the above-described angular calibration procedure.

Needle Tracking

To track needle tip trajectory through the phantom in a sequence of images, the first step is to create a difference image by subtracting the previous image from the current image. This yields a difference image that is blank aside from a group of pixels indicating the change in needle tip position between the current and previous image. The difference image is then thresholded and the "blob" of connected pixels at the needle tip identified. The pixel furthest from the needle base within this blob is then taken as the needle tip position. Repeating this process many times with subsequent images yields the needle path, as shown by the dots superimposed on the final needle image in Figure 3.8.

When corresponding points on the needle in the left and right camera images have been identified using the above method, the 3D coordinates of these points are found by stereo triangulation. For intuition about these trajectories, it is useful to express them in a coordinate frame attached to the phantom tissue surface (with

two axes parallel to it). To obtain the transformation between a camera frame and this phantom frame, a point cloud registration was applied [15]. A 1 cm square grid was overlaid on the surface of the phantom tissue and 22 corresponding points were selected using a computer mouse by clicking on grid intersections in the left and right images. Since these points were known in both the camera coordinate frame (triangulated) and the phantom coordinate frame (from physical grid locations), the point cloud registration yields the transformation between the two. For the experiments in Sections 3.2 and 3.3, the needle was maintained within a few millimeters of the tissue surface at all times, so that it was not necessary to compensate for optical refraction. However, in the teleoperation experiments presented in Section 3.4, optical refraction compensation algorithms were employed (as discussed in Section 3.4), because it was possible for a human to drive the needle further beneath the tissue surface.

3.2.4   Effect of Insertion Velocity

An experiment was undertaken to explore the effect of velocity on needle steering. The needle used was a 0.83 mm diameter solid Nitinol cylinder (simulating a 21 gauge needle) with a smooth surface finish and a hand-machined bevel tip. The Nitinol cylinder used in these experiments was obtained from Nitinol Devices and Components, Inc. The phantom tissue was the Sim-Test material described previously, cast into a sheet approximately 15 mm thick. The needle was introduced horizontally, using the telescoping support device described previously (pictured in Figure 3.5). During the experiment, macroscopic displacement of the tissue by the needle did not occur. That
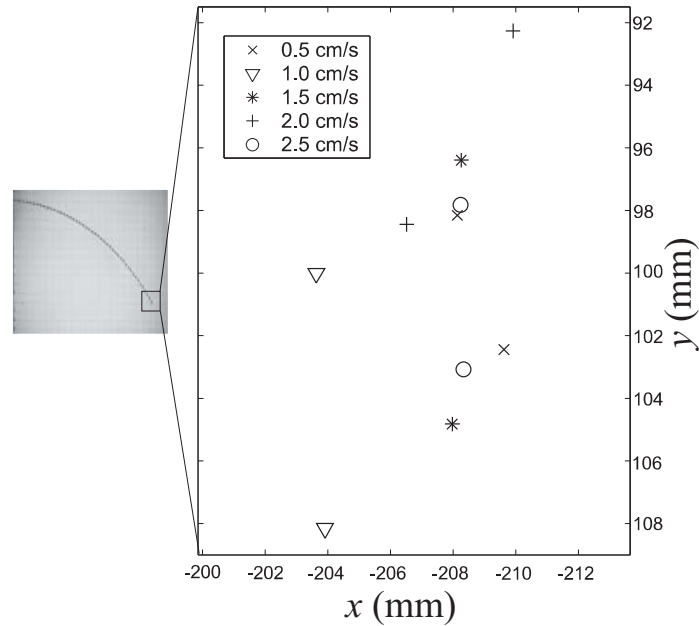
Figure 3.10: A scatter plot of final needle tip positions for different insertion velocities. No trend is apparent.

is to say, the needle shaft followed and remained approximately fixed in the path the tip cut through the rubber as shown in Figure 3.8.

The effect of velocity on needle bending was studied by inserting the needle multiple times into a single rubber sample at velocities from 0.5 to 2.5 cm/s in increments of 0.5 cm/s. Care was taken that the needle was not inserted repeatedly at the same location, so the path cut by each insertion would have no effect on other insertions. The needle used in this experiment had a hand-machined bevel angle of 40°. Each velocity was run twice, and the insertion distance for all runs was 25 cm.

The resulting tip and base positions were triangulated and expressed in the phantom tissue coordinate frame. The various needle paths were shifted so that they had a common starting point. Some runs were performed with the bevel tip facing to the right and some to the left, so the "left" data sets were reflected with respect to the
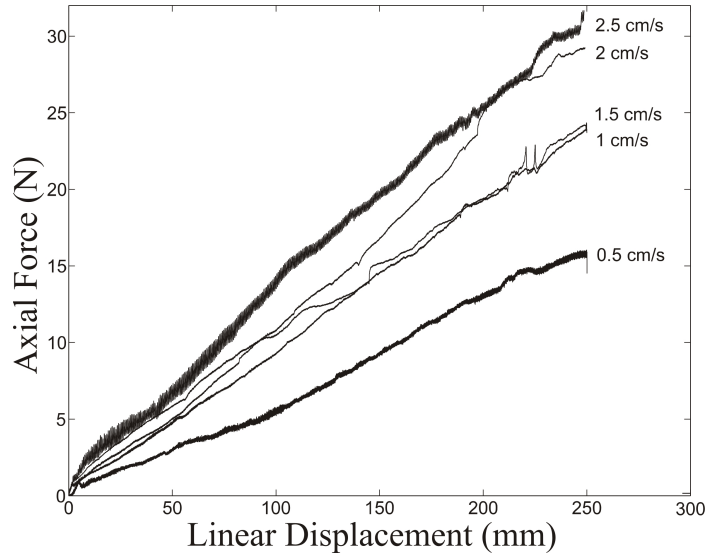
Figure 3.11: Axial forces for runs with different velocities showing that forces increase with velocity.

$y - z$ plane of the phantom coordinate frame at the needle base so that they could be compared directly to the "right" data sets.

Path effects

The results of the velocity experiment are plotted in Figures 3.10 and 3.11. As can be seen from the figure, there is no discernible trend in the final tip location of the needles for the different velocities. For our choices of phantom material, needle, and velocity range, velocity-dependent effects on path appear negligible.

Force effects

Velocity did have an effect on the force required to drive the needle into the tissue. Figure 3.11 indicates that as the velocity increases, the force required to insert the needle also increases. The variability of the force data changes at different velocities – some of the plots are smoother than others. The reason for this is mechanical
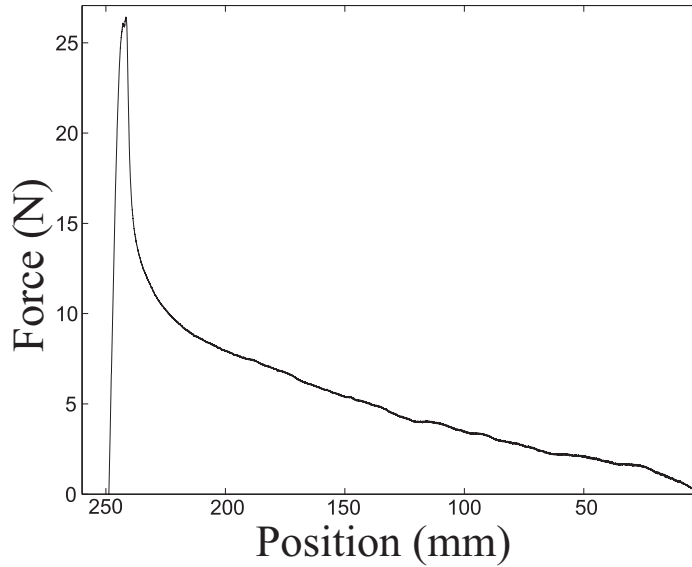
Figure 3.12: Example retraction forces. The peak where static friction releases the needle is clearly evident, and friction is fairly linear with insertion depth thereafter.

resonance of the linear stage–stepper motor combination used for insertion. The forces measured as the needle is extracted from the tissue (Figure 3.12) are as one would expect. The needle first overcomes static friction, and then the effects of kinetic friction are evident and shrink as the the amount of needle embedded in the tissue decreases.

3.2.5   Effect of Bevel Tip Angle

Since the asymmetry of the bevel tip provides steering actuation forces, it is reasonable to expect that different bevel angles will result in different needle paths, given other insertion parameters are held constant. We conducted an experiment to test the effect of a wide range of practical bevel angles on needle steerability. The materials and experimental setup used were identical to those described above in the velocity experiment above.
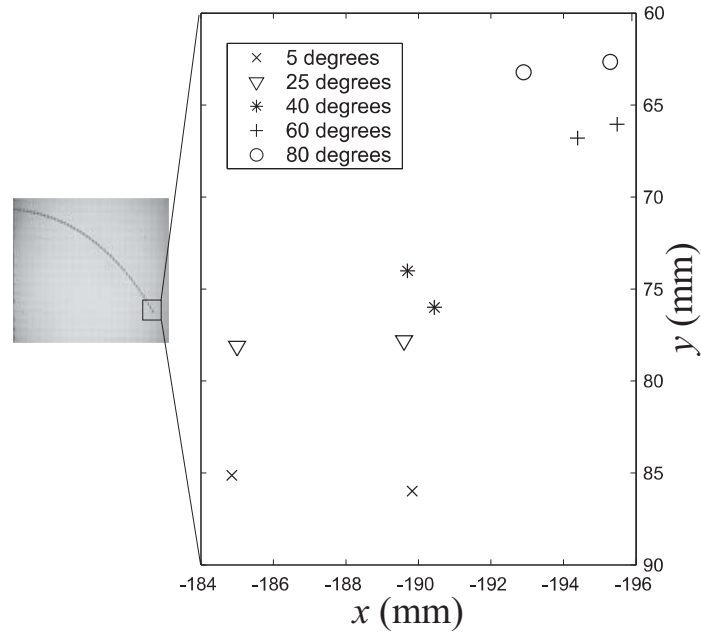
Figure 3.13: A scatter plot of final needle tip positions for a variety of bevel angles, showing a trend of increasing curvature with decreasing bevel angle.

The effect of the bevel angle on needle bending was examined by inserting the same needle multiple times into a single rubber sample. Between insertions, a different bevel angle was ground onto the needle tip. The angles used, measured as indicated in Figure 3.9, were 5°, 25°, 40°, 60°, and 80°. As in the velocity experiment, care was taken that the needle was not inserted at the same location twice. The needle was inserted for each run at a constant velocity of 1.5 cm/s. Each bevel angle was run twice, and all runs were for an insertion distance of 22 cm. The resulting tip positions were triangulated and compared as in the velocity experiment.

Path effects

The results of the bevel experiment are shown in Figures 3.13 and 3.14. As can be seen in the figure, there is a trend in the amount of bending obtained from the
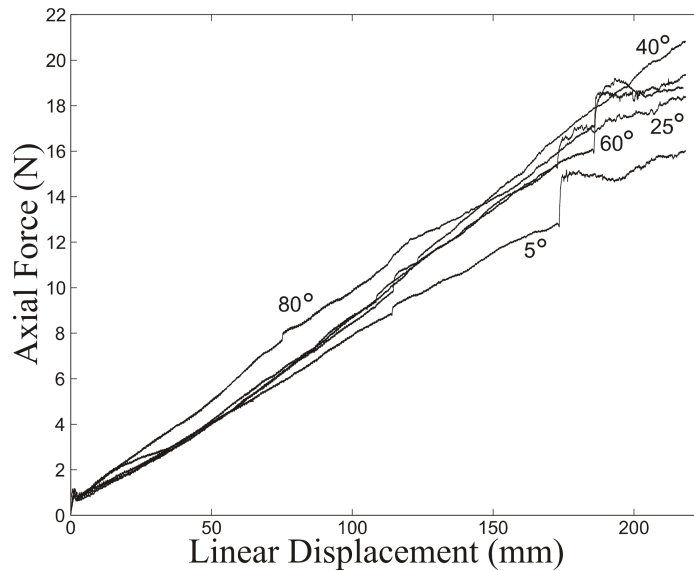
Figure 3.14: There is little discernible difference in axial forces for insertions of the same needle with different bevel angles.

Figure 3.15: The final needle locations, extracted from difference images, with different bevel angles illustrate the steering effect of the bevel tip. A 5° bevel exhibits the most bending while an 80° bevel exhibits the least.

different bevel angles, with 5° producing the most bending and 80° the least. Note that the range of bending in the y direction between the different bevel angles is approximately 2.5 cm, or over 10% of the total insertion distance. The final positions of the entire needle for all 5 bevel angles are shown in Figure 3.15.

Force effects

Figure 3.14 shows that there is little difference in the axial forces on the needle for different bevel angles, compared with the effect of velocity (Figure 3.11). This indicates that either the axial force associated with cutting is not strongly dependent on bevel angle, or (more likely) that friction on the barrel of the needle tends to dominate the axial cutting force of the needle tip. The sudden jumps in force near the end of the runs indicate situations when the needle pressed on the wall of the telescoping support sheath with enough force to cause a significant increase in its friction. The tangential forces (not shown here) yield little information, because the Delrin block that supports the needle at the tissue surface to prevent buckling does not allow them to be transmitted to the force sensor at the needle base. Torque data also is not useful for these particular experiments because the needle was not rotated about its axis during insertion. In more complicated 3D trajectories, torque may be useful for determining needle tip orientation.

3.3   A Model for Bevel-Tip Needle Steering

Until now, this chapter has examined needle steering through design and qualitative observation, addressing actuation, needle, and phantom tissue characteristics useful for bevel steering. This section explores steerable needle shape within tissue and describes a model for it. Consider a bevel-tip needle driven with two velocity inputs, insertion speed and rotation speed, actuated from the base of the needle. As the needle is inserted into tissue, the tissue imposes a reaction force on the bevel that
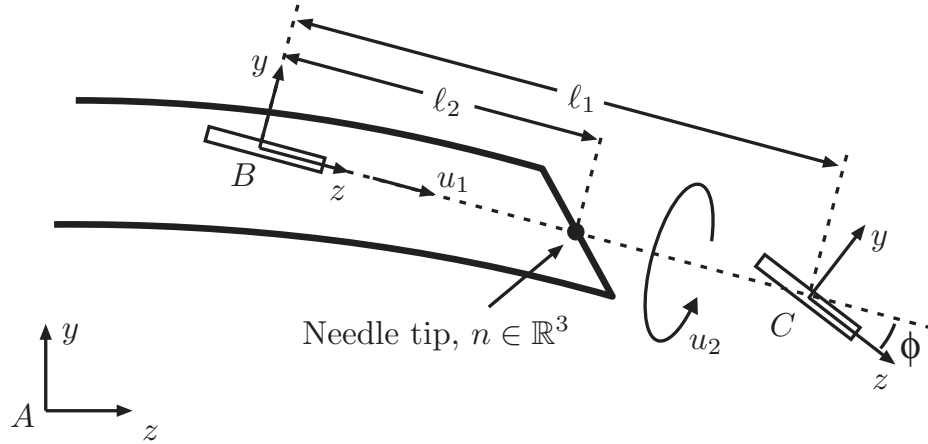
Figure 3.16: Configuration of a bevel-tip needle during steering showing the front and back "wheels" at frames B and C of a superimposed bicycle-like nonholonomic model. In this particular configuration, the x-axes for all three frames are pointing into the page.

deflects the needle tip, causing it to follow an arc. The rotational input at the base causes the needle to turn about its shaft reorienting the bevel. Neglecting the torsional compliance of the needle and assuming that the needle "stays in place" during reorientation, the tip rotates at the same speed as the base.

We model insertion speed and rotation speed as inputs to a kinematic nonholonomic system. We propose a variant of the standard kinematic bicycle, with constant front wheel angle, ϕ, and wheel base, ℓ_1, as depicted in Figure 3.16. Together ϕ and ℓ_1 specify the curvature, κ, of the needle path, and a second parameter, ℓ_2, determines the location along the bicycle that is attached to the needle tip, n. Roughly speaking, inserting the needle at speed u_1 is like "riding the bicycle" along a circular arc of radius $1/\kappa$ while rotating the needle at speed u_2 reorients the plane containing the bicycle's path. The two-parameter bicycle model can be reduced to a one-parameter "unicycle" model (a single wheel located directly at the needle tip) by appropriate

simplifications that remove ℓ_2 while retaining κ.

The purpose of this section is to determine the extent to which the 3D generalizations of the standard nonholonomic bicycle and unicycle models quantitatively capture the needle steering kinematics. To do so, we fit the model parameters experimentally and then statistically compare the bicycle and unicycle models to determine if the additional bicycle model parameter significantly improves the model fit. We suspect that the model parameters depend on many factors such as tissue stiffness, needle stiffness, and bevel angle, but we leave verification of these hypotheses for future investigation.

3.3.1   Planar Needle Kinematics

If the material properties of the needle are appropriately selected with respect to the properties of the tissue through which it travels, the needle shaft follows the trajectory of the tip almost exactly. This was shown in Section 3.2.3 using video of the needle insertion and comparing tip position in each frame to the final shaft trajectory (Figure 3.8). Thus, for an accurate representation of the entire needle shape, it suffices to describe the motion of the tip. We note that the models derived in this setting also applicable for less well-matched needle-tissue combinations (e.g. the same needle with a more compliant tissue medium). This has been investigated by collaborators, and their studies are briefly outlined in Section 3.6. However, for the remainder of the modeling work presented in this thesis, we will proceed by considering well-matched needle and tissue combinations, such that the shaft follows
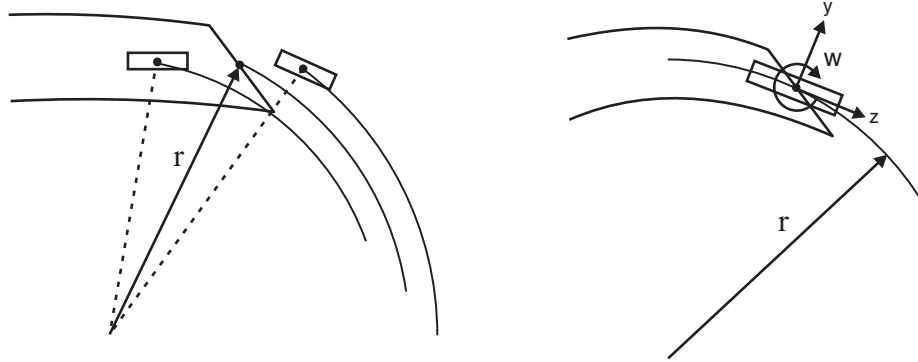
Figure 3.17: (Left) The modified planar bicycle model rotates as a rigid body about a center of rotation defined by the intersection of the two wheel axes. (Right) The modified planar unicycle model rolls with an angular velocity proportional to its linear velocity.

the trajectory of the needle tip.

In the plane, the standard nonholonomic model for a single wheel or "unicycle" (see [123], Example 7.4) has a single no-slip constraint. As shown in Figure 3.17, written in body frame coordinates, this constraint is $v_y = 0$. In the standard unicycle model, the angular velocity ω is variable and serves as a control input to the system. However, the needle bevel angle is fixed. To model this, we can modify the standard unicycle model slightly by fixing the ratio of linear velocity to angular velocity. This constraint can be written (again in body frame coordinates) as $v_z = r\omega = \frac{1}{\kappa}\omega$, and causes the unicycle to trace out a circular path with radius r and curvature κ.

Similarly, the standard nonholonomic car or "bicycle model" (see [123], Example 7.5) can be modified slightly by fixing the angle of the front wheel. The two wheel constraints cause the bicycle to rotate as a rigid body about the point where the perpendicular wheel axes intersect. If the needle tip was attached to the back wheel, this modified bicycle model would predict paths identical to the modified unicycle
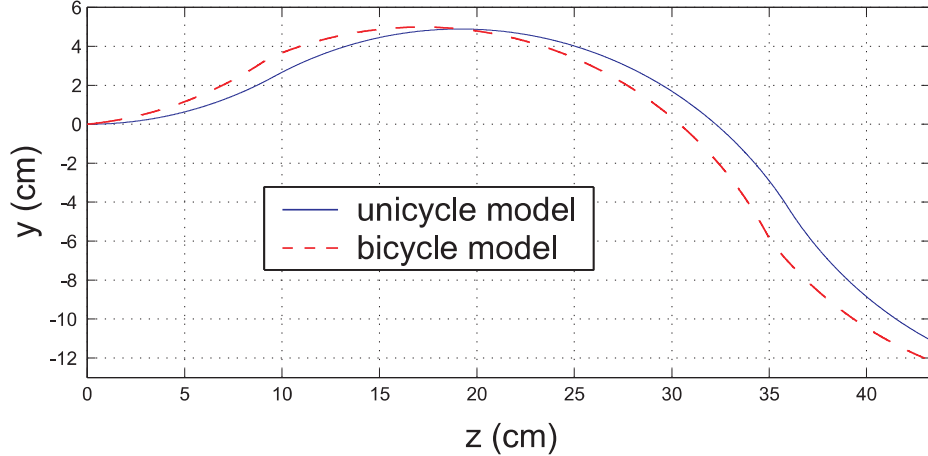
Figure 3.18: Comparison of the different planar paths for the one parameter unicycle model and the two parameter bicycle model. Parameters were $\kappa = 0.05$ and $\ell_2 = 2$.

model for $\kappa = \frac{\tan\phi}{\ell_1}$. However, if we allow the needle attachment position to be at a distance ℓ_2 from the rear wheel, we add a parameter to the model.

If the needle path is simply a single circular arc, this new parameter does not add descriptive power. However, for any trajectory more complex than a single arc, its predicted shape will differ from the single parameter unicycle model. The utility of this will be illustrated in Section 3.3.5, in which the model is fit to experimental data.

In the plane, a more complex trajectory with inflection points can be constructed by alternately pushing the needle into tissue for a finite distance and then axially rotating it $180°$. For the planar unicycle model, each axial rotation has the effect of changing the sign of the angular velocity constraint (changing the sign on κ). For the planar bicycle model, each axial rotation corresponds to instantaneously turning the front wheel from $+\phi$ to $-\phi$ or vice versa.

While both models generate circular arcs when moving forward, the arcs traced out by the unicycle must be tangent to one another, whereas the arcs traced out by

the bicycle need not be. Figure 3.18 simulates this effect on the trajectory predicted by each model given parameters of $\kappa = 0.05$ and $\ell_2 = 2$. In this simulation, the input profile was:

1. insert for one second at 10cm/s,

2. rotate 180°,

3. insert for two seconds at 10cm/s,

4. rotate 180°, and

5. insert for one second at 10cm/s.

It is interesting to note that the bevel-steering approach does not preclude linear paths for the needle. The needle may be inserted along an approximately straight path by continually rotating it at the base as it is inserted (effectively using a "drilling" motion). When this is done, our models predict a helical needle trajectory with extremely small radius that approximates a line. This effect is observed clinically, and spinning the needle is a recommended surgical technique to reduce the bending that results from the bevel tip (see [173], page 8.16). In addition, a path approximating a planar circle with reduced curvature can be obtained by duty-cycling the needle, effectively creating very small out of plane helices. Generalizing the planar unicycle and bicycle models to full rigid transformations (SE(3)) is the subject of the next section.

3.3.2 Notation and Definitions

Ultimately, we seek to use the two control inputs, insertion and rotation, to drive a needle to a desired position and orientation in six degrees of freedom (DOF). Since generalized coordinates (such as $(x, y, z, \mathrm{roll}, \mathrm{pitch}, \mathrm{yaw})$), have singularities, we resort to a coordinate-free representation of the kinematics. Fortunately the kinematic needle equations are quite simple in the coordinate-free representation, but the convenience and generality comes at the added expense of the formalism and notation established in this section. We follow the conventions in [123].

Consider the three reference frames such as those of the bicycle model depicted in Figure 3.16: a stationary world frame, A, and two "body" frames, B and C, attached to the needle tip. Using the homogeneous matrix representation, let

$$g_{ab} = \begin{bmatrix} R_{ab} & p_{ab} \\ 0^T & 1 \end{bmatrix} \in \mathrm{SE}(3) \quad \text{where} \quad R_{ab} \in \mathrm{SO}(3), \ p_{ab} \in \mathbb{R}^3 \tag{3.1}$$

denote the rigid transformation between A and B. Likewise, let $g_{bc} = (R_{bc}, p_{bc}) \in \mathrm{SE}(3)$ denote the transformation between B and C.

The isomorphism $\mathbb{R}^3 \simeq \mathfrak{so}(3)$ is defined by

$$\widehat{}: \begin{bmatrix} \omega_1 \\ \omega_2 \\ \omega_3 \end{bmatrix} \mapsto \begin{bmatrix} 0 & -\omega_3 & \omega_2 \\ \omega_3 & 0 & -\omega_1 \\ -\omega_2 & \omega_1 & 0 \end{bmatrix} \in \mathfrak{so}(3), \quad \vee: \begin{bmatrix} 0 & -\omega_3 & \omega_2 \\ \omega_3 & 0 & -\omega_1 \\ -\omega_2 & \omega_1 & 0 \end{bmatrix} \mapsto \begin{bmatrix} \omega_1 \\ \omega_2 \\ \omega_3 \end{bmatrix}, \tag{3.2}$$

where $\mathfrak{so}(3)$ is the Lie algebra of $\mathrm{SO}(3)$. It will be convenient to "overload" the definitions of $\widehat{}$ and $\vee$ for $\mathfrak{se}(3)$, the Lie algebra of $\mathrm{SE}(3)$. In other words, if $(v, \omega) \in$

$\mathbb{R}^6$, then

$$\widehat{\ } : \begin{bmatrix} v \\ \omega \end{bmatrix} \mapsto \begin{bmatrix} \hat{\omega} & v \\ 0^T & 0 \end{bmatrix} \in \mathfrak{se}(3), \qquad \vee : \begin{bmatrix} \hat{\omega} & v \\ 0^T & 0 \end{bmatrix} \mapsto \begin{bmatrix} v \\ \omega \end{bmatrix}. \tag{3.3}$$

Given two frames, X and Y, related by the rigid transformation $g_{xy} \in \mathrm{SE}(3)$, the body-frame velocity between them is given by

$$V_{xy}^b = \begin{bmatrix} v_{xy}^b \\ \omega_{xy}^b \end{bmatrix} = (g_{xy}^{-1} \dot{g}_{xy})^\vee, \quad \text{where} \qquad \begin{aligned} v_{xy}^b &= R_{xy}^T \dot{p}_{xy}, \\ \omega_{xy}^b &= (R_{xy}^T \dot{R}_{xy})^\vee. \end{aligned} \tag{3.4}$$

Given three frames A, B and C moving relative to each other, their body velocities are related by $V_{ac}^b = \mathrm{Ad}_{g_{bc}^{-1}} V_{ab}^b + V_{bc}^b$, where

$$\mathrm{Ad}_g = \begin{bmatrix} R & \hat{p}R \\ 0 & R \end{bmatrix} \tag{3.5}$$

is the Adjoint operator for a rigid transformation $g = (R, p) \in \mathrm{SE}(3)$.

The unit vectors $e_1, e_2, e_3 \in \mathbb{R}^3$ are the standard basis.

3.3.3 Nonholonomic Constraints and Control Inputs

In the bicycle model, frames B and C are rigidly connected with parallel x-axes, such that the origin of C is a distance ℓ_1 along the z-axis of B. The y-z plane of C is rotated by angle ϕ about the x-axis, as shown in Figure 3.16. Thus $R_{bc} = e^{\hat{e}_1 \phi}$ and $p_{bc} = \ell_1 e_3$, where ϕ and ℓ_1 are constants to be determined experimentally as described in Section 3.3.5.

There are four Pfaffian constraints, because the velocity of the origin of frame B cannot have a projection along the x or y axis of frame B, and the velocity of the

origin of frame C cannot have a projection along the x or y axis of frame C. In other words:

$$e_1^T v_{ab}^b = e_2^T v_{ab}^b = e_1^T v_{ac}^b = e_2^T v_{ac}^b = 0. \tag{3.6}$$

Since frames B and C are fixed with respect to each other, $V_{bc}^b = 0$. Thus $V_{ac}^b = \mathrm{Ad}_{g_{bc}^{-1}} V_{ab}^b + V_{bc}^b = \mathrm{Ad}_{g_{bc}^{-1}} V_{ab}^b$, and the Pfaffian constraints can be simplified to

$$\begin{bmatrix} 1 & 0 & 0 & 0 & 0 & 0 \\ 0 & 1 & 0 & 0 & 0 & 0 \\ 0 & 0 & 1 & -\frac{1}{\kappa} & 0 & 0 \\ 0 & 0 & 0 & 0 & 1 & 0 \end{bmatrix} V_{ab}^b = 0, \tag{3.7}$$

where $\kappa = \frac{\tan \phi}{\ell_1}$. Assuming $\ell_1 \neq 0$ and $\phi \in (0, \pi/2)$, a basis V_1, V_2 for the right nullspace of A defines the two allowable directions:

$$V_1 = \begin{bmatrix} v_1 \\ \omega_1 \end{bmatrix} = \begin{bmatrix} e_3 \\ \kappa e_1 \end{bmatrix} \quad \text{and} \quad V_2 = \begin{bmatrix} v_2 \\ \omega_2 \end{bmatrix} = \begin{bmatrix} 0_{3\times 1} \\ e_3 \end{bmatrix}, \tag{3.8}$$

The vector V_1 corresponds to pure needle insertion, while V_2 corresponds to pure needle shaft rotation.

Since we assume the needle shaft is held in place by the surrounding tissue, the effect of the shaft is to replicate needle base control inputs at the tip. Let $u = (u_1, u_2)$ denote the control inputs, where u_1 is the insertion speed, and u_2 is the shaft rotation speed. This leads to the following kinematic model:

$$V_{ab}^b = u_1 V_1 + u_2 V_2, \quad \text{or, equivalently} \quad \dot{g}_{ab}(t) = g_{ab}(t)(u_1 \widehat{V_1} + u_2 \widehat{V_2}), \tag{3.9}$$

and

$$n(t) = R_{ab}(t)\ell_2 e_3 + p_{ab}(t). \tag{3.10}$$

The unicycle model can be viewed as a simpler form of the bicycle model by setting $\ell_2 = 0$. This is equivalent to removing the front wheel of the bicycle to create a unicycle with a fixed ratio of linear velocity to angular velocity. The unicycle model also has four Pfaffian constraints:

$$e_1^T v_{ab}^b = e_2^T v_{ab}^b = e_2^T \omega_{ab}^b = 0, \qquad \frac{1}{\kappa} e_1^T \omega_{ab}^b = e_3^T v_{ab}^b, \tag{3.11}$$

the first three of which are straightforward. The fourth constraint above relates the angular velocity of the unicycle about e_1 to the insertion speed, corresponding in the planar case to a circular path with curvature κ. These constraints lead to a constraint matrix identical to the bicycle model (Equation 3.7), thus yielding the same allowable directions as before (Equation 3.8). In the unicycle model, n coincides with the origin of frame B, reducing the number of model parameters from two to one by removing ℓ_2.

Summarizing, the two models can be written as follows:

$$g_{ab}^{-1}(t)\dot{g}_{ab}(t) = u_1 \widehat{V_1} + u_2 \widehat{V_2},$$

$$V_1 = \begin{bmatrix} e_3 \\ \kappa e_1 \end{bmatrix}, \quad V_2 = \begin{bmatrix} 0 \\ e_3 \end{bmatrix} \tag{3.12}$$

$$n(t) = R_{ab}(t)\ell_2 e_3 + p_{ab}(t) \quad \text{bicycle model}$$

$$n(t) = p_{ab}(t) \qquad\qquad\qquad \text{unicycle model} \;\; (\ell_2 = 0)$$

Note that for both the bicycle and unicycle models, the constraints (Equation 3.7) are independent of g_{ab}, and thus the control vector fields are left-invariant. The systems (Equation 3.12) are nonholonomic, since the distribution $\Delta = \text{span}\,\{V_1, V_2\}$ is not involutive. This can be seen by taking the first Lie bracket of V_1 and V_2 in Equation

3.12

$$V_3 = [V_1, V_2] = (\widehat{V_1}\widehat{V_2} - \widehat{V_2}\widehat{V_1})^\vee = \begin{bmatrix} 0_{3\times1} \\ \\ -\kappa e_2 \end{bmatrix}, \qquad (3.13)$$

which is linearly independent of V_1 and V_2 (and thus Δ is not involutive). Successive

Lie brackets reveal that the system is of nonholonomy degree 4, with a relative growth

vector of $(2, 1, 2, 1)$ ([123], Chapter 7). Therefore, this system is controllable, and

as described in Section 3.6 subsequent work has applied this model successfully to

control and planning for bevel-steered needles.

3.3.4 Discrete Model

A discrete implementation of the kinematic model, Equation 3.12, enables simu-

lation and visualization. Advancing the homogeneous transformation, g_{ab}, along V_{ab}^b

for t seconds for each time step, $k = 0, 1, 2, \ldots$, yields the discrete-time model

$$g_{ab}(k+1) = g_{ab}(k)e^{\left(u_1(k)\widehat{V_1} + u_2(k)\widehat{V_2}\right)t}$$

$$(3.14)$$

$$n(k) = R_{ab}(k)\ell_2 e_3 + p_{ab}(k).$$

The control inputs $u_1(k)$ and $u_2(k)$ now denote the insertion distance and change in

rotation angle, respectively, at step k.

3.3.5 Experimental Parameter Fitting and Validation

The friction drive actuation unit (Figure 3.1) was used to control both insertion

(u_1) and rotation (u_2) speeds. The needle used in the experiments was a 0.7 mm

diameter solid Nitinol cylinder (simulating a 22-gauge needle) with a smooth surface

finish and a hand-machined bevel tip of 45°. The phantom tissue was the Sim-Test

material described in Section 3.2.3. As discussed previously, for this needle and phantom tissue, the needle shaft will follow the tip as it cuts through the tissue (Figure 3.8). It is expected that similar results can be obtained in phantom tissues with a wide range of properties by selecting the appropriate needle stiffness. While the Sim-Test media, which is qualitatively similar to muscle, is stiffer than some organs (e.g. liver), we expect our modeling assumption to hold even in softer tissues if we increase the flexibility of the needle shaft. Quantifying the properties of living tissue is an active research area. As these properties are quantified more fully, our understanding of the effect of needle shaft properties on steering will improve. Our Nitinol needle and Sim-Test media represent a specific example of a needle/tissue pair with appropriately matched properties. This results in a significant steering capability and fits our modeling assumptions. Initial experiments indicate that bevel-tip needles can steer well even in needle/tissue combinations that are not as well matched (e.g. softer tissue, stiffer needle), but the shapes they take on may change to some degree. This is a topic of future research, and is discussed in more detail in Section 3.5.

The Sim-Test material was cast into a sheet approximately 15 mm thick, and the needle was introduced vertically. To collect coordinates describing the needle path, a physical grid was overlaid on the phantom tissue. A one cm square grid (shown in Figures 3.1 and 3.8) was laser etched into a clear polycarbonate sheet so that digital images could be taken of the needle path through the grid. Thirty two points along the needle path were recorded in pixel coordinates for each run. These pixel coordinates were converted to physical coordinates in a frame attached to the polycarbonate grid using the following procedure.

Nine calibration points (grid intersections), distributed evenly across the planar grid, were obtained in both pixel coordinates and physical coordinates. Then, using a 2-dimensional version the Direct Linear Transform (DLT) algorithm, the projective transformation was estimated from the point correspondences for each run. These transformations enabled us to express coordinates along the needle in the physical coordinate system. We estimate the error associated with this collection process to be within ±1 mm. The nonholonomic model was fit to this physical data as described in the following section.

Experimental Procedure

The needle described previously was inserted multiple times into a single phantom tissue sample for all experiments. Care was taken to insert the needle at a different location each time so that the holes cut by previous experiments would not affect subsequent trials. Because the phantom tissue is semi-opaque, visualizing the needle with an optical camera requires it to stay within a few millimeters of the surface. Doing so requires control of axial needle rotation (bevel direction), or the needle may move out of plane as a result of small errors in initial needle rotation calibration that can cause the plane of needle curvature to be slightly misaligned with phantom tissue surface. Accurate control of needle axial rotation requires the needle steering model parameters that these experiments are designed to reveal. However, the needle can be kept in a plane just below the surface of the tissue by manually making slight corrections to the axial rotation of the needle as necessary to minimize out of plane motion. In contrast to the rotational degree of freedom, the linear insertion velocity

is constant, and is computer controlled. Possible sources of error in these experiments include initial insertion angle from vertical, human controlled (approximately constant) spin angle, slippage of drive wheels relative to the shaft (not visually perceptible), small deformations of the phantom tissue, and identification of points on the needle path in digital images.

Two sets of input parameters were used in the experimental insertions. In one, u_2 was set to zero, and the needle was inserted at a constant u_1 to a depth of 235 mm. This created a "single bend" insertion profile. In the other, u_2 was set to zero for the first 1/3 of the total insertion depth (83.3 mm). Then u_1 was set to zero and the needle was rotated 180 degrees. Finally, with u_2 again fixed at zero, the needle was inserted the remaining 2/3 of the insertion depth at constant u_1, until the needle reached a total insertion depth of 250 mm. This created an S-shaped or "double bend" insertion profile. A total of 13 insertions were performed, composed of eight single bend insertions and five double bend insertions.

When the insertion speed u_1 is constant and needle rotation does not change ($u_2 = 0$), the needle tip follows a planar circular arc as described in Section 3.3. This arc is a function of the parameters κ and ℓ_2. To fit all 13 trials simultaneously, the parameter set was expanded to include two unique "nuisance parameters" for each individual trial. These parameters were y_o^j (the y entry point of the needle) and γ^j (the initial angle of needle with respect to the z axis in the y-z plane) for each run, $j = 1, \ldots, 13$. The γ^j parameter was included because it was observed that while all insertions had similar basic shape and curvature properties, they differed by a slight rotation indicative of a small amount of error in initial entry angle. This error

was probably caused by the needle tip deforming the surface of the rubber before puncturing it, which deflects the angle of entry a small amount in the process. The vector of parameters is given by $\theta = (\kappa, \ell_2, y_o^1, \gamma^1, \ldots, y_o^{13}, \gamma^{13})$.

While it is possible to integrate the path of the needle using the Lie group expressions given in Section 3.3 (which is done to generate the plots in Section 3.3.5), the nonlinear parameter estimation is greatly facilitated with a closed form expression for the needle trajectory. This allows the nonlinear fitting algorithm to run much more efficiently, and eliminates small errors associated with the integration time step. It is straightforward in the planar case to derive such an expression for the needle path in terms of the circular segments that describe it.

For a single run of the bicycle model (j superscript omitted for clarity), the radius of the arcs (all have the same radius) is

$$ r = \frac{1}{\kappa} = \sqrt{\ell_2{}^2 + (\ell_1 \cot(\phi))^2}. \tag{3.15} $$

The position of the center of the first arc is

$$ c_1 = \begin{bmatrix} 0 \\ y_o \pm r \cos(\sin^{-1}(\ell_2 \kappa) + \gamma) \\ \pm r \sin(\sin^{-1}(\ell_2 \kappa) + \gamma) \end{bmatrix}, \tag{3.16} $$

where the $\pm$ is selected by whether the arc points toward the positive or negative y direction. The center of subsequent circular arcs (after rotating u_2 by $180°$) is given by a similar expression where the nuisance parameters have been replaced by the

90

ending conditions of the previous arc (denoted by the leading superscript e):

$$c_i = \begin{bmatrix} 0 \\ {}^e y_{i-1} \pm r \cos(\sin^{-1}(\ell_2 \kappa) + {}^e \gamma_{i-1}) \\ {}^e z_{i-1} \pm r \sin(\sin^{-1}(\ell_2 \kappa) + {}^e \gamma_{i-1}) \end{bmatrix}. \tag{3.17}$$

For a single run of the unicycle model, the radius of the arcs is

$$r = \frac{1}{\kappa}. \tag{3.18}$$

The position of the center of the first arc simplifies to

$$c_1 = \begin{bmatrix} 0 \\ y_o \pm r \cos(\gamma) \\ \pm r \sin(\gamma) \end{bmatrix}, \tag{3.19}$$

and the center of subsequent circular arcs similarly simplifies to

$$c_i = \begin{bmatrix} 0 \\ {}^e y_{i-1} \pm r \cos({}^e \gamma_{i-1}) \\ {}^e z_{i-1} \pm r \sin({}^e \gamma_{i-1}) \end{bmatrix}. \tag{3.20}$$

Given these circle centers, the desired z directional prediction ($\hat{z}$) for a value y is then given by the equation for a circle:

$$f(z, \theta) = e_2^T c_i + \sqrt{r^2 - (z - e_3^T c_i)^2}$$
$$e_3^T {}^e c_{i-1} \le z \le e_3^T {}^e c_i, \tag{3.21}$$

where e_2 and e_3 are standard basis vectors such that, for example, $e_2^T c_i$ denotes the y component of the center of the ith circle segment.

This closed-form model can now be fit to the experimental data using Matlab's `nlinfit` command. This function numerically computes a Jacobian in terms of the
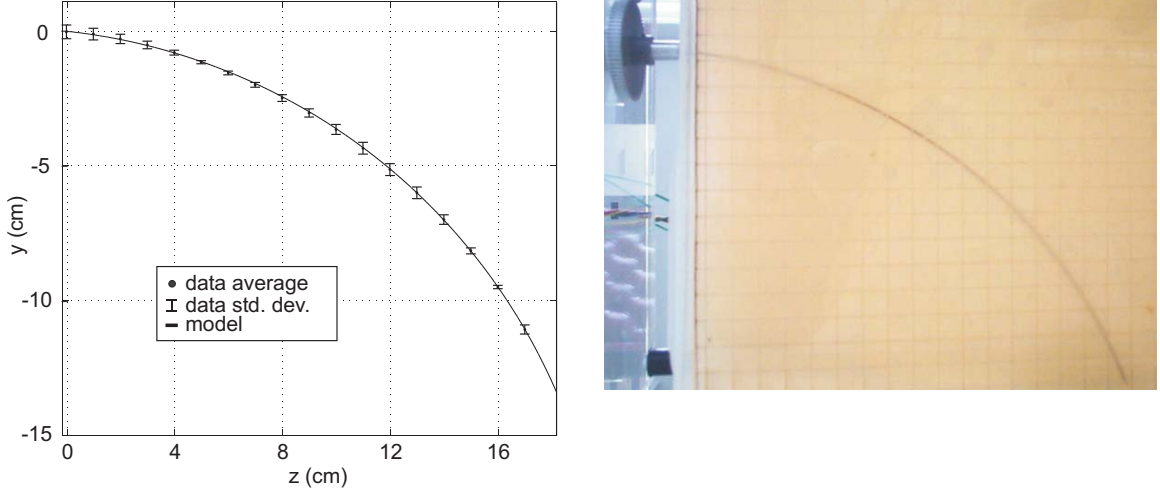
Figure 3.19: (Left) The bicycle nonholonomic model prediction for a single curve run, shown with average data (including nuisance parameters) and standard deviation bars. (Right) During the experiment, the needle was inserted 23.5 cm, without spin.

parameters,

$$J = \frac{\partial f}{\partial \theta}. \tag{3.22}$$

It then uses the Gauss-Newton gradient decent method to minimize the residual error between the observed data points and the predicted ones.

Results

For the bicycle model, the experimentally fit parameters were $\kappa = 0.0449$ and $\ell_2 = 2.38$ cm, with 95% confidence intervals of $\pm$ 0.001 and $\pm$ 0.15, respectively. Note that κ can be directly related back to bicycle steering angle (ϕ) and distance between the wheels (ℓ_1), since κ is a function of both. For example, choosing $\ell_1 = 4$ cm yields a steering angle of $\phi = 10.18°$. Figures 3.19 and 3.20 show plots of the single bend and double bend fitted models along with mean data values and standard deviation bars for each data point, with the nuisance parameters taken into account.
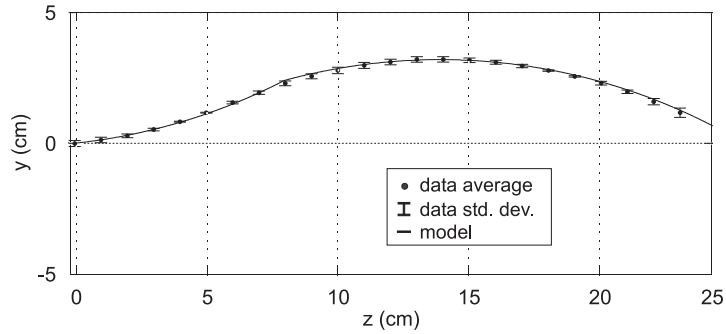
Figure 3.20: (Top) The bicycle nonholonomic model prediction for a run with two curves, shown with average data (including nuisance parameters) and standard deviation bars. (Bottom) During the experiment, the needle was inserted 8.3 cm, spun 180°, then inserted another 16.7 cm.

The plots were generated by integrating the Lie group expressions given in Section 3.3.

The experimentally fit parameter for the unicycle model was $\kappa = 0.0468$ with a 95% confidence interval of $\pm$ 0.0001. Since the unicycle model can be viewed as a simpler form of the bicycle model, we can use a hypothesis test to determine whether the second parameter in the bicycle model represents a statistical improvement in describing the needle trajectory over the unicycle model (null hypothesis). A t-test with $\alpha = 0.01$ leads to rejection of the null hypothesis, $(P < 0.01)$ and we conclude that the bicycle model is statistically significantly better at describing the data. This is illustrated graphically in Figures 3.21 and 3.22.

As shown in Figures 3.19 and 3.20, the bicycle model qualitatively fits the data very well. Quantitatively, the root mean squared error between the model prediction
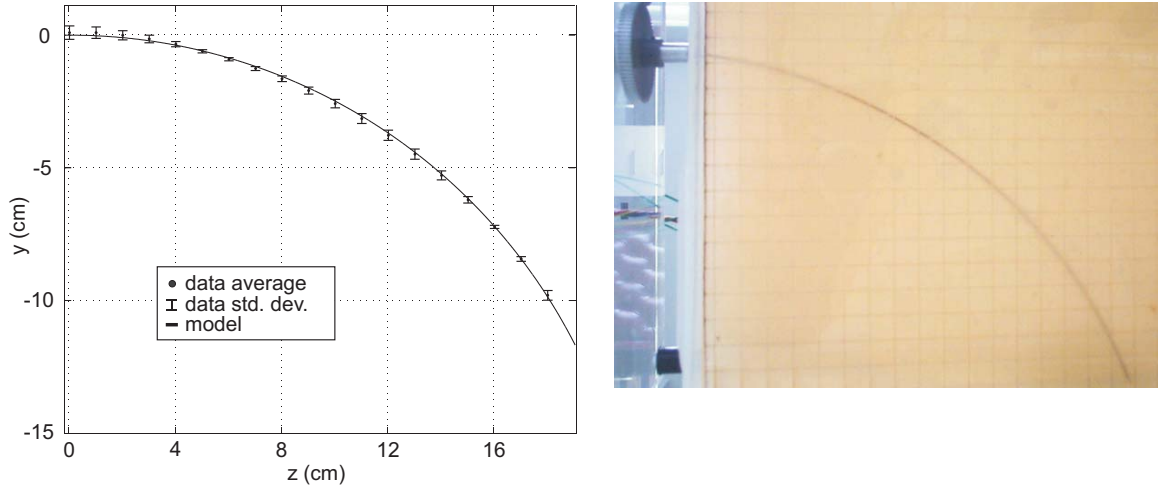
Figure 3.21: (Left) The unicycle nonholonomic model prediction for a single curve run, shown with average needle path data (including nuisance parameters) and standard deviation bars. (Right) Photograph of one needle insertion.

and the observed data points is 1.3 mm for the bicycle model, compared to 2.6 mm for the unicycle model. The error for the bicycle model is quite low, however it is slightly above our measurement error estimate of ± 1 mm, so there may be a small amount of inherent variability in the data not captured by our kinematic model.

3.4 Teleoperation

Model-based or teleoperative control for steerable needles can compensate for disturbances from a variety of sources including error in entry angle (the "nuisance parameters" mentioned with regard to model fitting above), tissue deformation, etc. Planning can also accomplish this, but a priori knowledge of tissue properties are usually limited in clinical practice. In this section, we consider the teleoperation of very flexible needles with beveled tips. We view teleoperation as a key enabling technology for clinical adoption, both because many doctors are more readily willing to adopt a
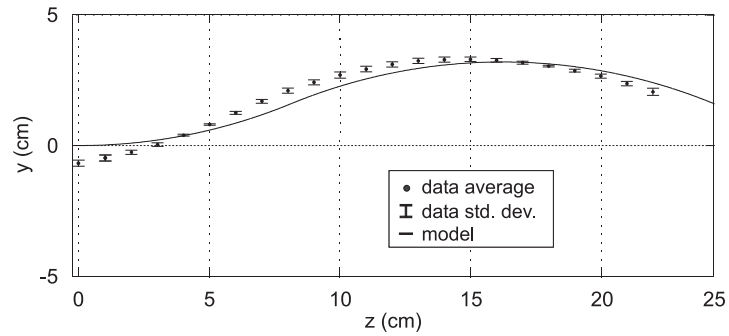
Figure 3.22: (Top) The unicycle nonholonomic model prediction for a run with two curves, shown with average needle path data (including nuisance parameters) and standard deviation bars. The single parameter model is not able to fully capture the curvature variations of the physical needle. (Bottom) Photograph of one needle insertion.

system that provides them with a sense of direct control, and because initial closed loop control results, while promising, have not yet exceeded teleoperative accuracy. This is a qualitative observation since no study exists to date comparing teleoperation and automatic control. It is expected that teleoperative control will provide a gold standard with which to compare the accuracy and safety of automatic controllers, since bevel-steered needles are too flexible to be inserted by hand. When an automatic controller can exceed human teleoperative ability in terms of either accuracy or safety in phantom studies, it will be a good candidate for clinical application.
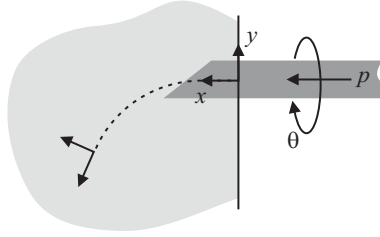
Figure 3.23: All coordinates in the teleoperation system are considered with respect to a coordinate frame fixed to the rubber at the needle entry point and oriented as shown above. The linear and angular positions of the needle are represented by θ and p, respectively.

3.4.1 Role of Teleoperation in Control

In Section 3.3, a nonholonomic model was presented that describes the needle tip pose as a function of two inputs, insertion velocity and angular velocity of the bevel about the needle axis. Using this model, along with mechanical and geometric tissue properties, it is possible to plan optimal paths to reach a desired target [6, 7, 10].

While the nonholonomic model can describe the path of the needle in fairly homogeneous phantom tissues (e.g. those discussed in Section 3.2.3), there will be unmodeled perturbations in living tissue, due to inherent inhomogeneity and deflection effects of boundary layers. To address these disturbances, several complementary approaches are possible. One is a low-level, closed-loop, image-based control system and another is high-level replanning based on image feedback. Initial studies on each of these have been undertaken by collaborators (see Section 3.6). These methods would allow completely autonomous needle control, once the target and obstacles are defined by the radiologist or surgeon. The focus of this section is a third approach, teleoperation. In teleoperation, the human operator provides real-time position or rate commands that are followed as closely as possible by a slave robot.

Teleoperation offers both advantages and disadvantages in comparison to autonomous, closed-loop control methods. A primary advantage is that it allows the surgeon to have closer control over the needle motion. For reasons of safety and acceptance by the medical community, this close interaction may be needed for initial clinical trials. A disadvantage is the difficulty humans have in planning and following paths with nonholonomic systems. In comparison to hand-held needle insertion, teleoperation can enhance steerability because the robot can use needles that would be far too flexible to accurately insert by hand. We propose that the best teleoperation method may be a mixed approach, where the human controls the invasive degree of freedom (DOF), insertion, while the computer controls the steering by spinning the needle about its axis. This section describes how to combine the teleoperation system hardware described in Section 3.2.2 with visualization and graphical steering assistance displays. We then explore various control laws and levels of control through human subjects experiments comparing control methods in terms of accuracy and the paths planned by users.

3.4.2 Visual Feedback

In addition to an overhead camera view, the user is provided with two additional visual aids as shown in Figure 3.24. Since the overhead camera does not show depth well, we provide a depth meter in the form of a slider that displays the vertical depth of the needle tip with respect to the top and bottom surfaces of the tissue (in the z direction as shown on Figure 3.24).

Since the bevel tip is too small to visualize clearly in camera images, we also provide a second visual aid to the user to indicate bevel direction. A dial gauge indicates the direction the needle will curve (in the needle tip frame) as it translates forward, by displaying the reading of an encoder attached to the needle base. At the initial needle configuration, when the arrow is pointing toward 90°, insertion will cause the needle to curve in the plane of the tissue toward the positive y direction, as shown in Figure 3.24. An angle of 270° will make the needle curve in the opposite direction. Readings of 180° and 0° make the needle go up or down in the z direction, respectively. While the encoded base rotation may not perfectly correspond to tip rotation due to friction and finite torsional stiffness of the needle shaft, it is a good approximation – especially at shallow depths. Additionally, we expect the blood in human tissue to form a natural lubricant, making torsional deformation even less significant than in rubber phantoms.

3.4.3 Control Methods

To determine the effects of various controllers for the translational degree of freedom on user targeting accuracy we performed a set of experiments. These experiments also compare user performance against automatic open-loop control. The correspondence of degrees of freedom between the master and the slave is maintained as shown in Figure 3.7 for all experiments.

The teleoperation of needle spin is accomplished through a proportional-derivative
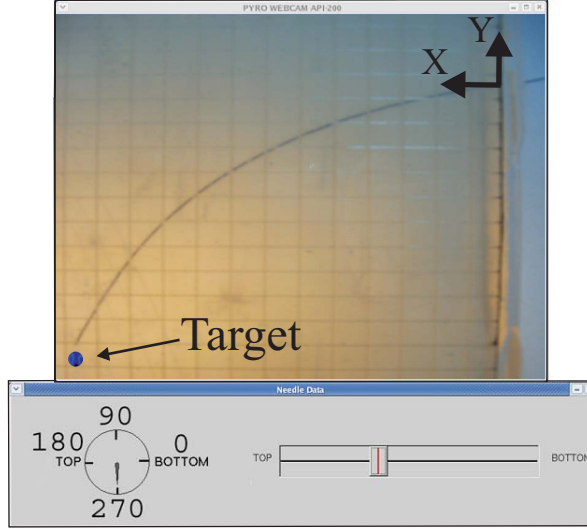
Figure 3.24: Operator feedback graphics window. The overhead camera view (top), direction gauge (bottom left), and depth meter (bottom right) can all be seen simultaneously by the user.

control law,

$$\tau_n = k_p(\theta_m - \theta_s) - k_d\dot{\theta}_s, \tag{3.23}$$

where θ_m and θ_s are the angles of the master stylus and slave needle/motor, respectively, k_p and k_d are the proportional and derivative gains, with values of 6.02 mN-m and 0.0602 mN-m-s respectively, and τ_n is the torque applied to the needle by a DC brushed motor. The needle is actuated using the telescoping support drive described in Section 3.2.1. The stepper motor on the linear degree of freedom in this system has its own low-level controller, which can accept either position or velocity commands. Three different methods to compute these commands are described below.

Position Control

One possible translational control method is a position controller:

$$p_s = k_1 p_m, \tag{3.24}$$

where p_m is the position of the master stylus, p_s is the desired position of the slave needle (transmitted to the low-level stepper motor controller), and k_1 is a unitless scalar gain of 0.7. The gain k_1 sets the fixed scaling between the master and slave positions. There is a tradeoff between fast response and accuracy in selecting k_1. Low values allow fine position control, but require the master to move a great distance to achieve appreciable slave motion. For our system, 0.7 yields the best accuracy for a reasonable distance of master motion. Also, the system can be "clutched" such that motions made in the direction of retraction are ignored, allowing repositioning of the stylus for further insertion. This effectively increases the workspace of the master. A beneficial consequence of preventing backward motion for the human factors experiments presented in Section 3.4.4 is that it limits the variation in user strategies for reaching the target, so that they can be more easily compared.

Rate Control

Rate control enables master displacement to define the velocity of the slave. In our system it is implemented using the following relationship,

$$v_s = k_2 p_m, \tag{3.25}$$

where k_2 is a scalar gain with a value of 0.052/sec. A point near the center of the F6S workspace was set as the zero position of the x-axis. Translations of the

master to the left (positive x direction) result in needle insertion into the tissue. A virtual spring-damper force feedback system was implemented on the master to pull the operator back to the zero position, as is commonly done in rate-control input devices. Retractions of the needle are again disallowed by ignoring displacement in the negative x direction.

v^2 Control

To create a system that simultaneously enables long quick motions, yet maintains the ability to do fine positioning in the vicinity of the target, we developed a new control law based on the square of the velocity (the "v²" control law). This law was inspired by computer mouse pointer control, also known as mouse ballistics. It is a scaling control law where rapid motions of the mouse cause much larger pointer displacement than slower motions of the same physical distance. Mouse ballistics inspired the following v² needle control law,

$$v_s = k_3 v_m^2, \tag{3.26}$$

where k_3 is a scalar gain with a value of 21.6sec/m. This nonlinear control law causes slow motions of the master to produce fine-resolution movements of the slave regardless of workspace position, but also enables the slave to move faster when the master is moved quickly.

3.4.4 Teleoperation Experiments

As described in Section 3.2.2, 3D needle position sensing is accomplished using calibrated stereo cameras. A version of the well-known Sum of Squared Differences (SSD) tracking algorithm was used to process images, extracting needle tip position with an update rate of approximately 5 Hz. Using high-resolution cameras we applied an algorithm provided by Vinutha Kallem to account for light refraction at the tissue surface. Kallem devised this algorithm by observing that light rays from each stereo camera will be refracted with the same refractive index at the tissue surface, and finding the intersection of the refracted rays. If rays do not exactly intersect (due to small noise in the system), the midpoint of the normal line at the closest passing of the rays to one another is used. This algorithm provides a position measurement accuracy of 1 mm. This tip position data is recorded for analysis and also transmitted to visual displays that assist the user in performing the insertion task as described below. A third camera, an ADS Technologies Pyro Firewire Webcam, provides a real-time view of the needle to the user.

All experiments reported in this section were performed using a cylindrical Nitinol needle with a diameter of 0.6 mm and a bevel angle of 45°. The phantom tissue used for the experiments was Super Soft Plastic described in Section 3.2.3 molded into a rectangular prism $28 \times 28 \times 4$ cm. Similarly to previous experiments described in this chapter, care was taken to insert the needle at a new position for each run, so that trajectories previously cut in the phantom tissue would not affect the current insertion.

To test the effect of the control methods described in Section 3.4.3 on user performance in reaching specific targets, we conducted a series of experiments. Subjects were instructed to perform a series of targeting tasks to reach two different points in the needle's workspace – one near its edge and one near its center – requiring different strategies to reach them. Target 1 was selected as the average point reached by the needle tip in the x-y plane in eight 12 cm insertions with a fixed bevel direction of 90°, at a fixed velocity of 6.35 cm/s. Target 2 was selected as the average point reached by the needle tip in the x-y plane in eight 13 cm insertions at the same velocity, where the bevel tip was first fixed at 90°, then inserted 6.5 cm, then rotated to 270°, and finally inserted another 6.5 cm. In order to view the needle tip in the camera image and initiate tip tracking, the starting point for all insertions was at a depth of 2 cm inside the phantom tissue. The needle was moved to this position by first inserting 1 cm with the bevel angle was fixed at 0°, and then inserting 1 cm with the bevel angle was fixed at 180°. All data reported (including the selection of target positions) starts from this 2 cm position inside the tissue.

For each trial, the control method was described to the user and he or she performed an unrecorded practice run in order to become acclimated to the system. The user was instructed to position the needle tip as close as possible to the target in the $x - y$ plane, and perform the task as swiftly as possible without sacrificing position accuracy. During the practice run, users were instructed to navigate to one of the two targets described above, while the experimenter provided assistance (primarily, pointing out the proper interpretation of the graphical feedback). After the practice run, the system was reset to the starting conditions and the users were then told to

repeat the task for the recorded trial. The recorded trials were identical to the sample run, with the exception that no assistance was provided by the experimenter. After navigating to one target under a given control law, the target was then changed and the trial repeated with the user being instructed to navigate to the new point. The control law was then changed, and the above sequence of explanation, practice run, and recorded trial was repeated. The order of presentation of the three control laws was varied randomly among the users to remove any potential learning effect from the results.

Our nomenclature for the experimental conditions is of the form [letter] [letter] [number]. The first letter denotes the control law used for the translational motion with P indicating the position control law (Equation 3.24), R indicating rate control (Equation 3.25), H indicating the v^2 control (Equation 3.26), and A indicating automatic insertion at a fixed velocity by the computer. H is used for the v^2 controller because it seeks to be a hybrid of the best features of the other two control laws (though not in the traditional sense of a "hybrid controller" applied to systems that contain both discrete and analog signals). The second letter in our nomenclature denotes whether the rotation stage was controlled by the human operator (denoted 'H') or controlled automatically by the computer (denoted 'A'). The final number in our nomenclature refers to the specific target point, '1' for Target 1, and '2' for Target 2. For example, PH1 should be interpreted as position control of translation, human control of needle axial rotation, and Target 1 as the objective.

A total of 14 subjects, from 18 to 27 years of age, performed the experiments described above. Experience in teleoperation ranged from novice to expert, a range

equivalent to the varying experience level in teleoperation of interventional radiologists and other clinicians who perform needle-based procedures. Since steering flexible needles (especially via teleoperation) is significantly different from inserting rigid steel needles by hand, we did not require subjects to have experience in hand-insertion to qualify for our study. To keep the each subject's experiment duration below one hour, each subject performed a subset of all combinations of trials listed above. All subjects attempted RH1, RH2, RA1, RA2 with one trial each. For PH1, PH2, PA1, PA2, HH1, HH2, HA1, and HA2 subjects were alternated between position and hybrid control, performing all permutations of only one of the two. That is, if a user performed PH1, he/she would not perform HH1, and vice versa.

3.4.5   Results

The effect of different control methods on the targeting accuracy of the subjects was determined from data collected by the stereo cameras. The error metric used to evaluate the targeting accuracy was the $x - y$ distance of needle tip from the target $(e = \sqrt{\delta x^2 + \delta y^2})$. We did not include depth (z) in our error metric because the main goal specified to subjects was to reach the correct $x - y$ position, with maintaining constant depth being a secondary objective. We did not restrict needle motion to a specific plane because this would require closed-loop control of tip position, and such controllers are not yet available, despite promising initial results [97]. Simply restricting the angular rotation of the needle to two discrete values 180° apart would not account for tissue inhomogeneity and finite torsional stiffness of the needle shaft.

	RH1	PH1	HH1	RA1	PA1	HA1	AA1	
RH2	■		y	y	y	y	y	RH1
PH2		■	y	y	y	y	y	PH1
HH2	y	y	■	y	y	y	y	HH1
RA2	*	*	y	■				RA1
PA2	*	*	y		■			PA1
HA2	*	*	y			■		HA1
AA2	*	*	y				■	AA1
	RH2	PH2	HH2	RA2	PA2	HA2	AA2	

Figure 3.25: Scheffe test results for a single factor ANOVA of varying control methods vs. radial distance from needle tip to target. 'y' represents a statistical difference in means with a confidence greater than 95%, '*' means a confidence between 85% and 95%, and a blank space means a confidence lower than 85%.

The difference in angle between tip and base created by finite torsional stiffness was more pronounced in this experiment than in previous experiments reported in this chapter (though it was still manageable by a human), due a phantom tissue that prioritized transparency over low-friction characteristics.
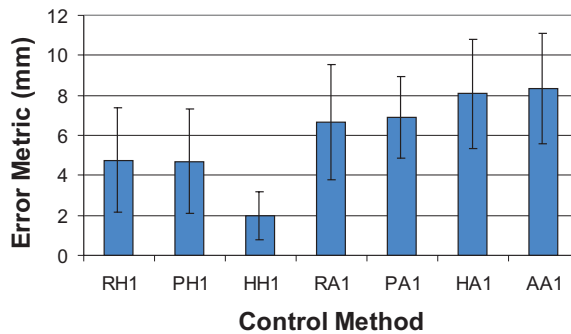
Figure 3.26: Mean and standard deviation of the radial distance from needle tip to target for various combinations of control methods to reach Target 1.

106
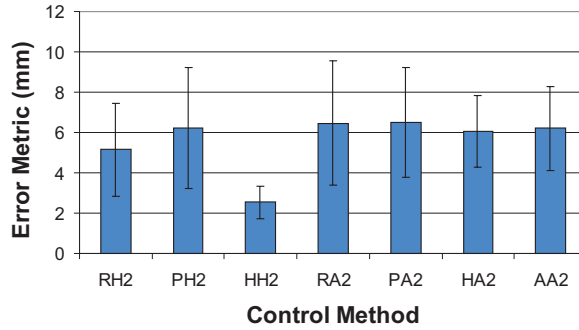
Figure 3.27: Mean and standard deviation of the radial distance from needle tip to target for various combinations of control methods to reach target 2.

Targeting Accuracy

To evaluate user targeting performance, we performed a single-factor, one-way, random-effects ANOVA. The independent variable was the control method used and the dependent variable was the error metric. This enables a statistical comparison of improvement in user performance of our targeting tasks. Figure 3.25 presents the statistical significance of pairwise comparisons, determined using a Scheffe test. Figures 3.26 and 3.27 show the average and standard deviation of the targeting error resulting from the various control methods. The columns AA1 and AA2 represent the fully automated case, where the computer controlled both rotation and insertion of the needle open loop.

The clearest result of these experiments is that the new v^2 control law enabled users to target more accurately than any other controller. This validates our hypothesis that a controller inspired by mouse ballistics can improve teleoperated needle steering accuracy over more traditional rate and position control methods. We attribute this increase in accuracy to the seamless scaling between rapid movements

and fine positioning control of the v^2 control law. Using rate control, users often accidentally deviated very early in the trial from the correct family of possible trajectories too significantly to recover before reaching the target depth. Conversely, using position control, users navigated successfully to the area near the target, but were incapable of fine-tuning their position within this area. This is as one would expect for the linear position and rate control mappings, in contrast to the nonlinear mapping of v^2 control.

The data also shows that human control of needle spin can be statistically significantly more accurate than fully automated open-loop control. We attribute this to human compensation for a number of sources of uncertainty in needle tip position that produce variation in trials with the same input joint angle profiles. Among these factors are (1) inhomogeneity of the phantom tissue (present to some degree despite it being cast from a single batch of Super Soft Plastic), (2) initial deflection of the needle upon "popping through" the rubber surface (the "nuisance parameters" described in section 3.3.5), and (3) small errors in calibrating the initial zero rotation angle of the bevel tip. Under open loop control, all of these sources of error cause deviations from the expected needle endpoint. As one would expect, the human reduces the effect of these sources of error by servoing the system toward the target.

User Strategy for Task Completion

As described above, Target 2 was achieved in the fully automatic trials by generating an 'S' shape by making a single 180° rotation of the bevel angle half way through the insertion. It is interesting to note that most human subjects tended to
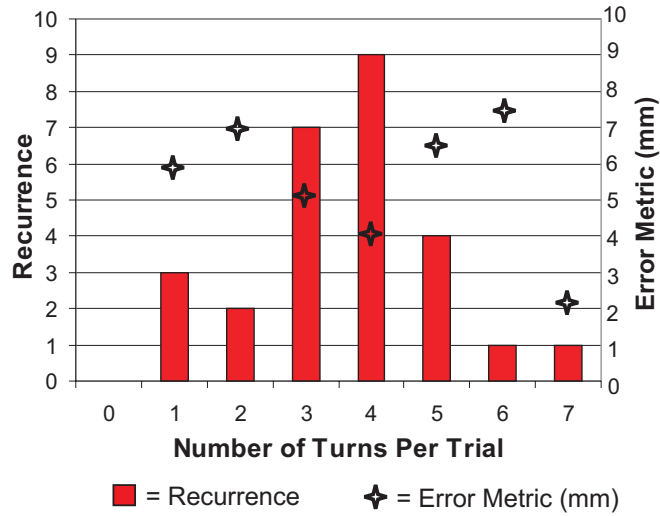
Figure 3.28: (Left Axis) Histogram of the number of users performing n turns. (Right Axis) The average radial distance from the needle to tip to the target point for users performing a specific number of turns.

use insertion strategies composed of 3 to 5 180° turns when attempting to reach the same target point as shown on the histogram in Figure 3.28. Figure 3.29 shows several example user paths taken to reach the target, as well as one open-loop computer controlled trial.

3.5 Discussion

We have presented design considerations for needle steering, a pair of kinematic models that describe needle trajectory, and a teleoperative control scheme expected to speed clinical adoption of steerable needles. Experiments and statistical analysis verify that the two-parameter "bicycle" model describes the needle behavior better than a single-parameter "unicycle" model. The path predicted by the two-parameter model is in close agreement with experimental data, but there remain several points
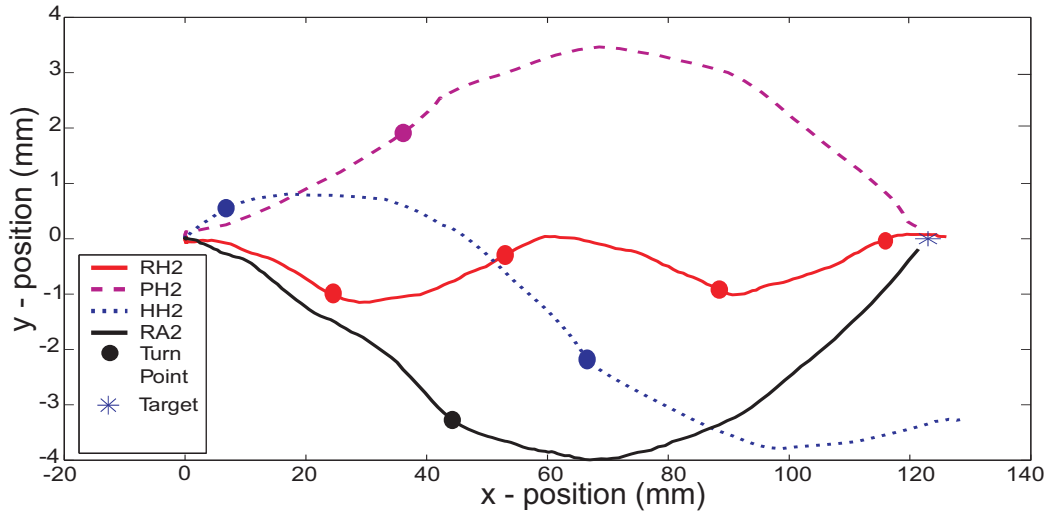
Figure 3.29: Users applied different strategies for reaching Target 2. Most users invoked more axial spin of the needle than the computer-controlled case. Note that the axes above are not equally scaled.

to consider for future improvements of the model, and future enhancements to experimental procedures. One is the modeling assumption that the needle and tissue be matched so that the needle shaft follows the tip as it does when 21–22 guage Nitinol needles are steered through the Sim-Test simulated muscle material.

If the needle and tissue are not as well "matched" for steering (e.g. the same needle is used with softer tissue), simulations indicate that the shape of the needle path will change [7]. One solution is to change needle shaft properties by choosing a material with less flexural rigidity (e.g. plastic materials, perhaps), or to increase tip size with respect to shaft size [59, 60]. However, even without changing shaft properties, our model in well matched needle/tissue combinations may still provide a basis for control. It can be incorporated into finite element models (FEM) of tissue to predict the needle path in softer tissues [7]. In [7], our model provides an idea of where the needle tip will deflect as it severs nodes of the FEM tissue mesh. The

basic model can also be used for planning in conjunction with dynamic programming for unmatched needle/tissue combinations [10]. While the model and experiments in the matched setting described in Section 3.3.5 provide a first step toward analytical representations of needle shape in an unmatched setting, future research is needed in this area. Even in the absence of such analytical representations, our model may be useful for higher rate control than is currently possible with FEM techniques, since they are often computationally intensive.

It may also be possible to build other possible physical effects into the basic structure of our model. One physical consideration is that the trajectory of an actual needle intuitively ought to be at least once-differentiable. Both the bicycle and unicycle models will be once-differentiable as long as the needle insertion does not stop when the bevel is reoriented (that is, $u_1 = 0$ while $u_2 \neq 0$). The unicycle is once-differentiable for any combination of u_1 and u_2, but for the bicycle model, if rotation happens without simultaneous linear insertion, a small "kink" (the non-tangent circles mentioned in Section 3.3.1) will result. While a kink seems intuitively unlikely for an embedded needle, it may have physical significance for the trajectory of the channel cut by the needle with respect to relaxed tissue geometry after needle withdrawal (see Figure 3.30). Thus, further research is needed to evaluate the physical significance of such a "kink" from various perspectives.

Another physical consideration is that needles have finite torsional stiffness. As the flexural rigidity of the needle shaft is reduced to enhance steering, torsional rigidity will also likely decrease. We have considered possible modifications to our basic kinematic model that may help remove smooth kinks and take torsional stiffness into

Figure 3.30: Trajectories cut through Supersoft Plastic phantom tissue, after needle withdrawal (and corresponding tissue relaxation). Note the kink near the middle of the runs, where the needle was rotated 180°.

account. The models described in Section 3.3, both have the following body velocity structural form, amenable to numerical integration via Equation 3.9:

$$V_{ab}^b = \begin{bmatrix} 0 & 0 & u_1 & \kappa u_1 & 0 & u_2 \end{bmatrix}^T, \tag{3.27}$$

where u_1 is the insertion velocity and u_2 is the shaft rotation velocity. One possible way to modify this model is through alternative descriptions of the parameters, and another is to add new parameters.

To account for torsional stiffness, it may be useful to add a new parameter, for example $\omega_{\text{tip}} = \alpha u_2$, where α may be a nonlinear function of time and/or arc length that appropriately captures the effects of friction and torsional stiffness. The human controlling the rotational degree of freedom in our experiments (as described in Section 3.3.5) compensated for torsional stiffness effects by rotating the needle base further than the desired tip rotation. Both torque information sensed at the fingers and visual observations of the needle tip may have been useful to the human to keep the needle in plane. To enable automation of this, one area of device improvement we will pursue is utilizing available torque sensing in the telescoping support drive design. Torque sensing will be useful for torsional compliance modeling and incorporation into control systems.

It must be emphasized that it is not clear whether this compensation for torsional

stiffness will be necessary in live tissues. They contain inherent lubrication (blood), and we expect them to have far less friction with the needle shaft than is observed in rubber phantoms. It is also possible to reduce friction by using various gels (containing water or other liquid) as the phantom tissue, presumably more closely replicating the interaction between the needle and human tissue. However, as mentioned previously these gels must have sufficient strength to prevent the needle shaft from shearing through them. A possible means of preventing shear even in lower strength gels may be to embed fibers in the gel. This may also more closely replicate some fibrous human tissues.

Steering directly in in vivo or ex vivo tissues introduces many new phenomena that may be modeled or compensated for using control, including membrane pop-through effects, as well as tissue inhomogeneity and anisotropy. While these may be challenging to model, they do not appear to preclude steering needles using bevel-tip forces. Figure 3.31 shows a fluoroscope image of a needle inserted into bovine muscle. It is clear that bending still occurs in this more realistic environment. It not known precisely what other effects will be seen in live tissues, but it is possible that some of these effects may enhance bevel-tip steering by allowing tighter curvatures to be realized, while others may reduce curvature. Experimentally, it will also be useful to track tissue deformation in three dimensions, perhaps using fiducial markers embedded in the phantom. We note that, to the best of our knowledge, no previous needle insertion modeling work (see Section 3.1) has recorded 3D needle insertions in real or phantom tissues that include bending, steering, or tissue deformation.

There may also exist useful alternative descriptions of needle trajectory in terms
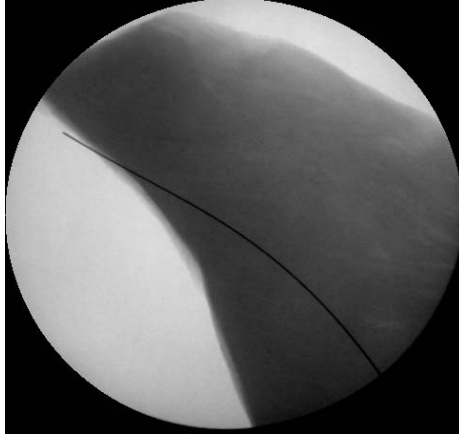
Figure 3.31: This fluoroscope image demonstrates that a 0.6 mm diameter Nitinol bevel-tip needle can steer through bovine muscle. While moving from homogeneous rubber phantoms to real tissue introduces new modeling challenges, this image shows that bevel-based steering is not limited to homogeneous rubber phantoms.

of more general differential equations. As suggested by collaborators Chirikjian and Kim [176], the general form might be

$$M\ddot{V}_{ab}^b + C\dot{V}_{ab}^b + KV_{ab}^b = U, \tag{3.28}$$

where M, C, K are constant matrices including general parameters, and U is an input body velocity, which can be a function of time and/or arc length.

Investigating these modified and alternative descriptions of needle kinematics is an area for future work, that will be pursued if they begin to show significant advantages over current models. When investigating new models, it will be critical to ensure that the model does not over-fit the data for a particular set of experiments. The model should be general and applicable to various needles and tissues, but without undue complexity or redundancy. To ensure this, a statistical analysis of model parameters such as the one carried out in this chapter when comparing unicycle and bicycle models is critical. Such an analysis was useful in development of the bicycle model,

where it highlighted the coupling between wheel base and front wheel angle.

In the clinical setting, the use of a control system with image feedback, as well as the ability to replan in real-time during insertion are expected to mitigate the need for a perfect, patient-specific model. As we draw nearer to clinical application of needle steering, we will seek a practical balance between a priori path planning based entirely on models, rapid replanning during insertion, and control through image feedback. Until such control methods exceed the accuracy of humans, teleoperation will be a key enabler of clinical needle steering. Even after controllers exceed human capabilities, it may still be desirable to allow the human teleoperative control over the invasive degree of freedom (insertion), for safety, liability, and clinical acceptance reasons. The computer can then control the steering of the needle by servoing needle axial rotation to direct it to the target point. This is perhaps the best possible practical compromise for initial clinical application of steerable needles.

3.6   Conclusions

Needle steering has many advantages over current clinical practice, in which needles follow only nominally straight-line trajectories and there is no means of compensating for errors induced by imperfect alignment, tissue deformation, etc. Steering flexible needles using a bevel tip has the potential to enable accurate, dexterous targeting for percutaneous medical procedures in a manner that minimizes tissue deformation and damage. The first step in steering a needle to a desired location is to design actuation units and needles suitable for bevel steering. In this chapter, we

presented two different actuation unit designs, a compact friction drive system, and a larger base-actuated telescoping drive system that included force/torque sensing. We addressed the challenges in creating a complete experimental setup for needle steering by describing considerations in choice of needle and phantom tissue materials, bevel rotation calibration, and stereo computer vision tracking. Experimental results showed that bevel angle affects steering. "Sharper" needles appear better in terms of maximum curvature, and curvature increased monotonically with reduction in bevel angle between $80°$ and $5°$, the most extreme angles easily producible by hand. We also found that the speed of needle insertion in the Sim-Test material had no discernible effect on steering. This may change with phantom tissues that more accurately represent other tissue types and different aspects of living human tissue, since tissue deformation may be more significant.

This experimental and design work laid the foundation for the kinematic analysis of the needle trajectory included in this chapter. We introduced a 6-DOF nonholonomic model based on steering due to bevel-tip asymmetry. We demonstrated that our model accurately predicts the path of a compliant needle through phantom tissue when the needle and tissue are appropriately matched. A Nitinol needle and rubber phantom qualitatively similar to human muscle provide an example of a matched pair. In particular, we demonstrated by statistical analysis that a two-parameter bicycle model describes the needle steering behavior statistically significantly better than a one-parameter unicycle model. As discussed in Section 3.5, more detailed kinematic models, together with improved experimental methods, are expected to enable accurate 3D needle control for a wider variety of tissue and needle parameters.

To facilitate clinical acceptance and to provide a standard by which to judge the success of model-based controllers, we developed a teleoperation system which allows the radiologist to remain "in the loop" during the procedure. We conducted human subjects experiments to evaluate targeting accuracy in phantom tissue for three steerable needle control methods: teleoperation of both insertion and spin, teleoperation of insertion with open-loop-controlled spin, and open-loop control of both insertion and spin. A mouse ballistics inspired v^2 control law for insertion resulted in statistically significantly better targeting accuracy. Targeting accuracy also generally improved with increasing number of degrees of freedom of human (teleoperation) control, due to human compensation for perturbations from unmodeled effects.

The work presented in this chapter has been published in [121, 143, 175–177], and relevant portions are patent pending [180]. This work (especially the kinematic model) has and continues to facilitate a broader study to improve the accuracy of needle targeting for clinical and research applications. It has formed the basis for many ongoing and future research activities (by both our research group and others), including:

- Integration of needle steering models into simulations that account for large tissue deformation and select optimal entry points and entry angles [7].

- Kinematic model enhancements that account for the effects of small deformation of the ambient tissue, and smooth the "kink" described in this chapter [109].

- Applying stochastic theory to account for uncertainty from tissue inhomogeneity and other sources of error [137]. In this work, the Euler-Maruyama method

is applied to generate the ensemble of reachable states of the needle tip, and inverse kinematics methods originally developed for hyperredundant and binary manipulators are applied with probability density information to generate plans.

- Viewing needle planning as Dubins car planning problem (with no reversal) and formulating planning as a Markov decision process solved via dynamic programming. Paths are planned that maximize the probability of reaching the target in the presence of uncertainty and large deformation [6, 10].

- Creating a Stochastic Motion Roadmap [12] by sampling collision-free states in the configuration space in conjunction with the Markov decision process mentioned above. This technique was demonstrated to produce significantly higher probabilities of success compared to traditional shortest-path plans.

- Path planning for steering needles around obstacles (e.g. bones, delicate structures, etc.) in order to acquire targets not previously accessible in two [6, 7, 10] and three [57] dimensions.

- Applying nonlinear observer-based, closed-loop control and dimensionality reduction to achieve planned needle motion based on optical image feedback [96, 97].

- Using force sensing to steer needles with the aim of minimizing unwanted deflection [3].

- Designing needles with larger tips and smaller shafts to enhance steerability, and experimentally demonstrating that duty cycling can be used to reduce in-
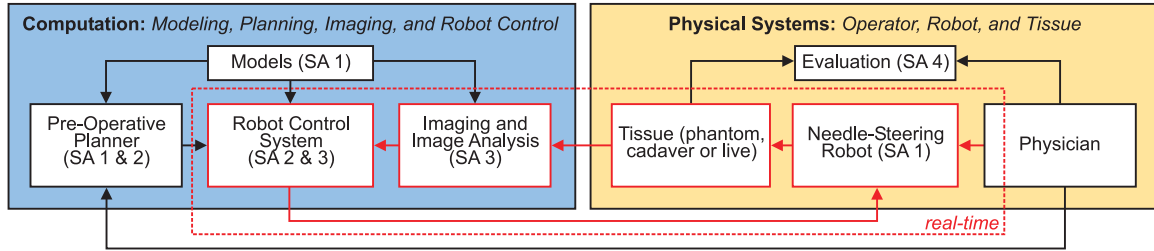
Figure 3.32: A conceptual block diagram of a complete, automated needle steering system. This system concept has been collaboratively developed by all JHU and UC Berkeley collaborators. Nonholonomic models presented in this chapter enable ongoing research in planning, control, and sensing, as well as work toward improving basic models and needle designs. On the physical side is the robot (e.g. those described in this thesis), the patient, and physician who monitors and/or teleoperatively controls the procedure, defines system objectives, and evaluates results.

plane curvature (creating very small out of plane helices) as the model in this chapter predicts [59, 60].

The goal of all of the above research is to develop a complete clinical system for needle steering combining medical image feedback, control, and planning to enhance needle placement accuracy human tissues under typical clinical conditions. The conceptual block diagram for the complete system, which has been developed collaboratively by all JHU and Berkeley collaborators, is shown in Figure 3.32. There remains much work yet to be done in each of the above research areas as well as the design, kinematic modeling, and teleoperation topics presented in this chapter. However, as indicated by the list above, a large literature of successful research results is emerging from our research group, collaborators, and others that have adopted our bevel-steering technique. Combined with initial alignment algorithms like the Virtual RCM of Chapter 2, bevel-steered needles appear poised to make important clinical contributions in the near future.

Moving forward, it is expected that a system combining the beneficial aspects of not only bevel steering, but also the alternative needle steering methodologies described in Section 3.1 (lateral force/torque application and/or curved elements) is expected to be even more powerful. One curved element design that holds great promise for enhancing steering by working in concert with bevel steering is the active cannula (the topic of the following chapter). Creating a combined system is straightforward; steerable needles can be deployed through active cannulas. Inspired by the dexterity and curved trajectories of steerable needles, active cannulas generalize steering by making it not depend on soft tissues media. Chapter 4 describes active cannulas, and a future unified dexterity system is further discussed in Chapter 5.

Chapter 4

Active Cannulas

We have developed a new class of thin dexterous continuum robot called active cannulas. An active cannula is a remotely actuated device with the potential to traverse narrow and winding environments without relying on "guiding" environmental reaction forces. These features seem ideal for medical procedures requiring passage through narrow openings to access air-filled cavities such as the throat and lung. Composed of telescoping concentric precurved elastic tubes, active cannulas are actuated at the base by the axial translation and rotation of component tubes. They derive bending actuation not from tendon wires or other external mechanisms, but from elastic tube interaction in the backbone itself, permitting high dexterity and small diameters. A consequence of the design is that dexterity improves with miniaturization. Active cannulas may also enhance patient safety because their inherent compliance mitigates potential trauma from inadvertent tool-tissue collision.

This chapter introduces the active cannula design and explores the hypothesis that overall cannula shape locally minimizes stored elastic energy, and examines the

significance of modeling torsional effects in addition to bending effects. This energy model enables analytical prediction of bifurcation in the energy landscape as a function of actuator positions, which matches experimental observations and provides a means for calibration. Additionally, the model predicts feature and tip positions of our prototype active cannula, providing another independent calibration method. We experimentally show close agreement of the two calibration methods, and that fit parameter values lie near expected ranges derived from tube physical characteristics. Using the energy model, we present a framework for the kinematics of multi-link active cannulas via energy minimization and Lie group theory. Experimental results validate the kinematic framework and demonstrate that modeling torsional effects is essential to predict active cannula bifurcation behavior and physical shape. These studies form a design and theoretical foundation for realizing the promise of active cannulas to reach minimally invasively into previously inaccessible locations in the human body. Some results in this chapter have been published in [178,179] and relevant portions are patent pending [181]. This chapter is also currently in preparation for archival journal publication [174,182].

4.1 Motivation and Related Work

Minimally invasive surgical (MIS) techniques have profoundly changed interventional medicine in recent years, reducing trauma and speeding healing. However, MIS remains applicable to only a small fraction of all surgeries. Many intervention sites lack viable minimally invasive alternatives because instruments simply cannot reach

them. These sites may require navigating entry pathways that are narrow and/or contain complex 3D bends, requiring the surgical tool to "turn corners". Also important (for most surgical tooling payloads) is that the tool maintain a degree of dexterity after reaching the surgical site.

These constraints render confined surgical sites off limits to current commercial surgical robots, as well as manual MIS tools. Standard clinical designs for both are characterized by relatively large diameters (typically 5–10 mm), rigid shafts, and (in the case of manual tools) lack of end effector dexterity.

These considerations motivate active cannulas, MIS devices that are thinner and more dexterous than existing alternatives. Active cannulas are a new class of miniature continuum robot that derive bending actuation not from tendon wires or other external mechanisms, but from elastic interaction of curved tubes that form the "backbone" of the device. This makes them sufficiently flexible and shapable to traverse bends and corners to access confined anatomical locations.

4.1.1   Medical Motivation

A number of clinical applications may substantially benefit from active cannulas. Active cannulas have been specifically proposed as solutions for a variety of clinical scenarios. These include fetal surgery [65], steering needles in soft tissues [118] and cardiac applications [145], transnasal skull base surgery [178], and transgastric surgery [178]. Several specific clinical areas in which active cannulas could improve surgical outcomes are as follows.

Head and Neck Surgery. Standard surgical treatment of many lesions in the head and neck requires traumatic dissection through layers of tissue, beginning with skin, muscle, bone, and any other structures between the surface of the patient and the surgical site. A surgeon must open enough space to allow his or her hands to enter – or at least to permit free motion of straight tools through holes wide enough for complex maneuvers (such as suturing). Despite all the care, effort, and skill the surgeon can bring to bear, the limited dexterity and flexibility of current surgical tools renders many of these procedures quite damaging to healthy tissue resulting in scarring and lengthly recovery periods.

Bio-Sensor Delivery. To effectively perform their function, most bio-sensors must be delivered to diseased tissue deep inside the body, or a sample must be collected for external analysis. Active cannulas are expected to be capable of deploying a wide range of bio-sensors, including stereotactic position (e.g. magnetic trackers), molecular [170], electrical impedance [5, 113, 170], contactless mechanical impedance [98], and optical luminescent [192] sensors, and it is reasonable to expect many more varieties of bio-sensor to be developed in the coming years. A delivery mechanism that can carry such sensors into confined spaces in the body will enhance their utility.

Skull Base/Sinus Surgery. Performed endoscopically through the nose [85, 102], treatment of lesions at the base of the skull (either inside or outside the brain cavity) is challenging because tools lack the dexterity to bend around and through small openings in the sinus cavities. To access various surgical sites, many healthy structures must also be removed. These include the nasal turbinates, which normally purify inhaled air and aid olfaction [142], and they cannot be reconstructed. Two specific

surgical sites that cannot be reached using straight tools are the areas behind the carotid arteries (near the base of the eye), and the frontal sinus cavities (reaching around a bone located directly behind the bridge of the nose) [151].

Throat Surgery. Treating lesions located deep in the throat currently requires large incisions. One reason for this is to enable suturing, which inside the larynx improves healing, reduces scar tissue, and thereby improves laryngeal function and sound production [47, 63, 188]. The throat provides an obvious avenue for MIS, but suturing down the throat requires more dexterity than current commercial tools can provide. Rigid tool motion is severely limited because tools must travel long distances through an 11 mm diameter tube (a laryngoscope). These considerations have also motivated another continuum robot designed for throat surgery [149] that is discussed in detail in Section 4.1.2. An active cannula should similarly provide the dexterity necessary for suturing down the throat, allowing many more minimally invasive treatments, with improved patient outcomes.

Lung Surgery. Going further down the airways into the lung is particularly important because the alternative access paths requiring opening the chest are traumatic. As the tool progresses, bronchi become progressively smaller until they terminate in bronchioles smaller than 1 mm in diameter. Thus, very thin steerable tools like active cannulas are needed to progress deep into the lung via the throat. It is also possible to insert needles between the ribs into the lung, but this approach runs the risk of deflating the lung. The advantage of this entry pathway is that tools traverse a shorter distance to reach the target. This entry path also requires dexterity, since only specific entry positions and orientations are permitted by the ribs. Control of

tool path after insertion begins is likely necessary for accurate tip positioning. Active cannulas are expected to be particularly beneficial in enabling MIS in the lung, through either the percutaneous (between rib) access path or via the less invasive but more technologically challenging throat entry path.

Radiofrequency Ablation. In this procedure, electrodes are deployed at the surgical site, and painless radiofrequency energy (similar to microwave heat) is transmitted to the tissue. This kills cells in order to treat a number of diseases, including cancerous tumors in the liver and kidney. The active cannula can improve the accessibility of small targets or targets in challenging locations for radiofrequency ablation.

Transgastric, and Fetal Surgery. The active cannula is also well-suited to transgastric surgery, where tools enter the stomach via the mouth, then exit the stomach and accomplish surgery in the abdominal cavity. Here, the active cannula idea provides a way to maintain dexterity even while tools traverse long distances through geometrically complex entry paths. Another interesting application is fetal surgery inside the womb, which is often not possible with straight tools because they must pass through two pivot points: one at the skin of the mother, and one at the wall of the uterus.

In many of the above applications, initial free-space cannula models (to date, only free-space models exist) will need to be coupled with tissue models. However, free-space models alone should be sufficient for applications characterized by air-filled passageways, such as surgery in the throat and lung. Each active cannula application will require customization of the design, and we foresee a family of both hand-held and robotically actuated active cannulas tailored to meet various clinical

126

needs. Hand-operated cannulas are clearly the most rapid path to clinical adoption, while a fully robotic cannula could be used as a slave in a teleoperated system. Nearly all foreseeable applications will require an accurate forward kinematic description of active cannula shape as a function of joint angles (translations and rotations of component tubes). Most will also require differential kinematics so that points on the robot can be moved as desired via joint velocities. Such a model serves not only as a starting point for more complex cannula/tissue interaction modeling, but is also directly applicable in free space within anatomy as in the throat and airways.

4.1.2   Related Work

Hand-held laparoscopic MIS tools generally consist of long, stiff, cylindrical shafts with small tools (grippers, scissors, etc.) on the distal end. Important robotically enabled advancements in MIS tool design include the addition of a wrist to manipulate an end effector (enhancing dexterity), and the use of robots to register the tool to an endoscope image (making a teleoperated system easier to use), e.g. [77]. Commercial teleoperated surgical robotics typically have 5–10 mm straight, rigid tools equipped with small wire or push-rod actuated wrists. While no universally agreed upon analytical wrist optimization framework for surgical robots currently exists, preliminary analytical methods indicate that snake-like wrists have advantages over traditional jointed wrist designs [32, 61].

Independent of wrist design, a major limitation of existing MIS tools is that they are constrained to pivot at the body entry point. While optimal port placement
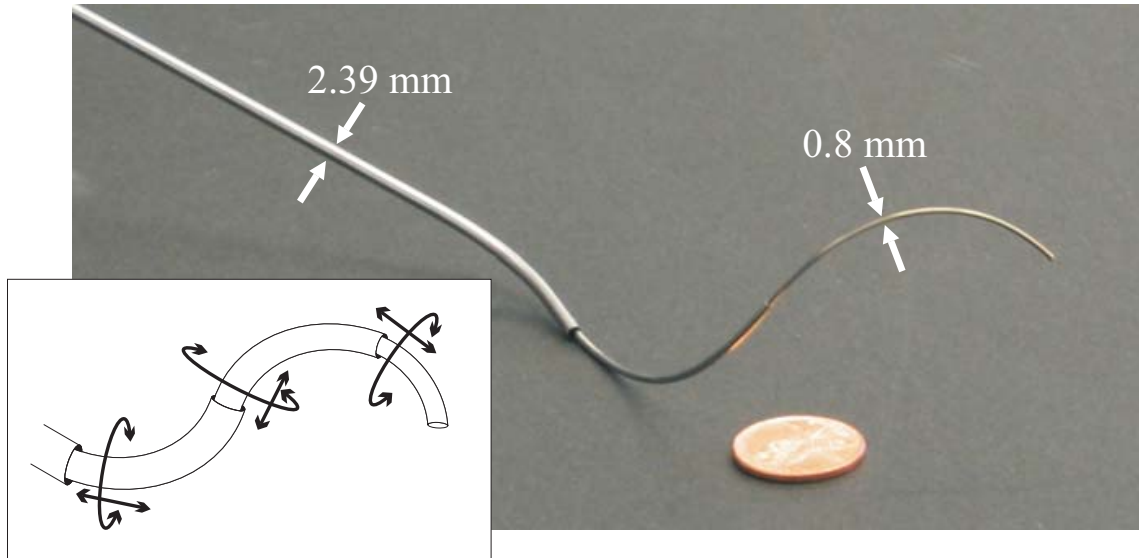
Figure 4.1: A prototype active cannula made of superelastic Nitinol tubes. The inset line drawing indicates the active cannula's degrees of freedom.

seeks to allow reasonable workspace volume under this constraint [4,31], there is little flexibility in port placement when accessing surgical sites through natural orifaces (e.g. throat or nostrils), which often offer the least invasive entry paths. This motivates a move away from straight rigid tools toward actively shapable flexible instruments.

Active cannulas change shape using precurvature of superelastic component tubes that can extend telescopically and rotate axially with respect to one another (Figure 4.1). While the location of actuation is similar to catheters (at the base, outside the body), active cannulas use a fundamentally different means of steering within the body and thus are not catheters. Catheters use blood vessel reaction forces to direct them down desired branches. In contrast, active cannulas require no tissue reaction forces, deriving steering from internal moments tubes apply to one another.

As described in detail in Chapter 3, recently several groups have successfully applied similar base actuation strategies to steer needles through soft tissue. The key

distinction between active cannulas and steerable needles is that active cannulas do not require a tissue medium in order to steer. This does not preclude their use as steerable needles (when coupled with tissue models). Various steerable needle designs can even be deployed through active cannulas (e.g. those in Chapter 3), if desired.

Active cannulas can can also be classified as continuum robots, since they are essentially miniature serial robot arms composed of variable curvature prismatic links. Within the context of continuum robots, active cannulas are unique in their use of the backbone itself to transmit bending forces. Continuum robots typically use an initially straight elastic backbone, which is bent by forces applied through external mechanisms like wires (e.g./ [45,80]), flexible push rods [149], or pneumatic actuators (e.g. [36, 95, 159]). While these external mechanisms advantageously permit direct control of curvature, they limit miniaturization. This motivates our desire to build bending actuation directly into the backbone itself.

Several designs with some similarity to active cannulas have been published recently. Loser [118], under the advisement of Russell Taylor at Johns Hopkins University, developed a steerable needle composed of two fully overlapping precurved cannulas that could be rotated (but not translated) with respect to one another in order to change needle curvature. Subsequently, Taylor [147] conceived a design where tubes translate and rotate with respect to one another, and considered several medical applications (Figure 4.2). A design similar to active cannulas was proposed by Furusho et al., who describe a "Curved Multi-Tube" (CMT) also with two curved cannulas that rotate but do not translate, through which a needle is deployed [65, 167], as well as a conceptual design sketch of a device very similar to the steerable needle of [132]
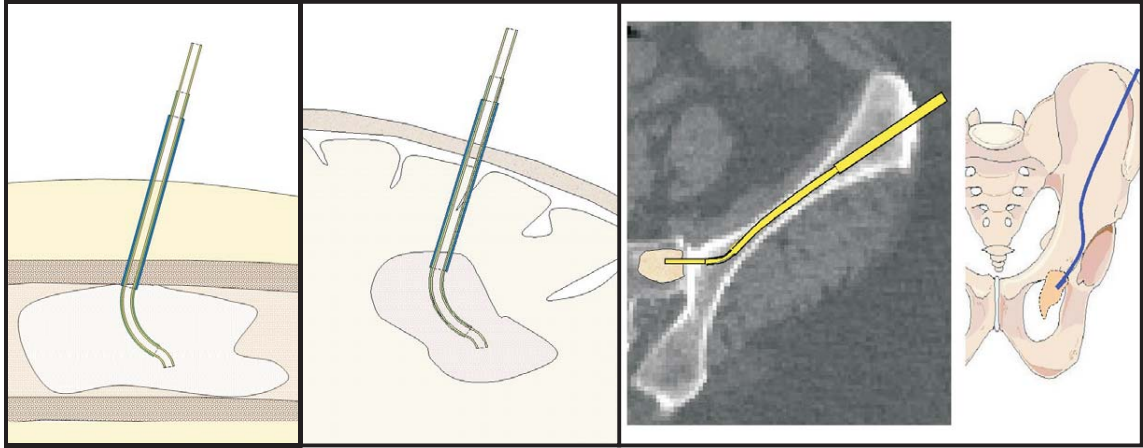
Figure 4.2: Potential steerable, bending cannula applications considered in JHU / Technion proposal in March 2002 [147]. (Left) Bone cancer ablation, (Center) brain biopsy or therapy delivery, (Right) inside-the-bone access paths. Images courtesy of Prof. Russell Taylor.

described below. CMT modeling has thus far assumed infinite flexural rigidity of each outer tube (compared to all those inside it), as well as infinite torsional rigidity. Okazawa et al. describe a steerable needle with a stiff outer cannula and a single flexible curved interior wire that can extend and rotate to control steering magnitude and direction as the needle is pushed into tissue [132]. Daum patented a deflectable needle assembly that deploys a curved "catheter" through a rigid outer cannula [48]. As far as the author is aware, this design has not yet been brought to market and no experimental results or models using the concept have yet been published.

Beam-mechanics-based models accounting for the effects of both translation and rotation of component tubes were first presented in [178, 179] by our group and [145] by Pierre Dupont and colleagues at Boston University. Developed concurrently yet completely independently, these models are strikingly similar. Though parametrized slightly differently, both describe arcs of concentric segments of curved elastic tubes

as a function of base angles of rotation. Both do so through computing the equilibrium of applied moments, under similar assumptions. One difference between the two studies is torsion, which is assumed negligible in [145], but included in transmission (the straight segments beginning at the actuators and ending at the start of precurved tube regions) in [178,179]. Without torsional compliance, the kinematics of an active cannula can be expressed in closed form. Including torsion in transmission leads to transcendental equations that must be numerically solved. While a framework for multi-link forward and inverse kinematics without torsion has been formulated [146], it has not yet been experimentally validated. Thus, our objectives in the following sections are to a derive multi-link kinematic framework that includes torsion, to determine model parameters via calibration, and to experimentally assess the accuracy and descriptive capability of models with and without torsion. We then use the kinematic model to derive the differential kinematics of an active cannula. First, however, we address the design of actuation mechanisms for active cannulas.

4.2 Actuation Unit Design Considerations

Control of active cannula joint variables (translations and rotations of component tubes) requires a suitable manual or robotic device. This section describes a modular differential drive robotic design, as well as a manual system with locking handles and manual encoding. It is anticipated that a manual solution may be most useful for initial clinical trials when coupled to a planner that outputs instructions to the human operator for the required sequences and quantities of motion of each joint variable.

However, a robotic solution will ultimately increase cannula functionality, enabling coordinated, simultaneous motions of the many input degrees of freedom.

4.2.1 Differential Drive

Each tube in the active cannula design requires two degrees of freedom of actuation – linear translation and axial spin. A suitable actuation unit must be capable of tightly gripping each tube and allowing other tubes to pass through it. It must also be capable of rapid movements as well as enough force output to overcome tube interaction forces and environmental reaction forces.

Design Specifications

We estimated that the actuation mechanism should be capable of 20 N linear force at a speed of 15.24 cm/sec (6 in/sec), based on qualitative observations of hand-operated active cannula prototypes. These rapid joint potions represent cannula velocities much faster than the usual speed with which surgical tools are manipulated, and thus they are expected to be higher than necessary in actual clinical active cannula use. However, a large margin between normal and maximum output capability is desirable in a robotic system when possible. In terms of rotation, the maximum torque necessary to spin large, stiff tubes (2.4 mm diameter) was estimated at 15.4 mNm based on measurements from initial prototypes. The end effector load specification was estimated at 300 g at a distance of 5 cm normal to the axis of the tube base. This was qualitatively judged to be well above the level of forces normally applied with devices of similar size in surgery, based on the author's experience. An additional
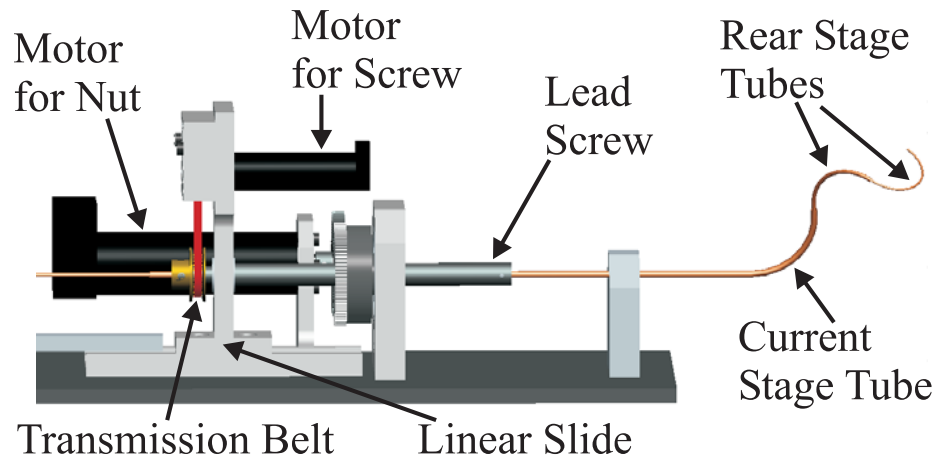
Figure 4.3: CAD drawing of differential drive actuation unit for one tube.

147 mNm of actuation torque is required for this load specification. The desired rotational speed specification was 3.33 rev/sec.

Design Concept

A design capable of achieving the above specifications is the differential drive shown in Figure 4.3. The modular design is built around a lead screw, where both screw and nut are independently actuated. A hole is drilled through the screw, and an active cannula tube is fixed to the screw via a collet at the forward end of the screw. One motor actuates the nut threaded onto the screw. Spinning this nut alone causes linear translation of the tube. The second motor actuates the lead screw itself via a belt drive. Actuating this second motor alone causes the lead screw (and thus the precurved tube) to rotate, while also translating. Rotating both motors simultaneously (the first motor compensates for the translation of the second) causes pure rotation. Copies of this modular differential drive can be used to actuate each

tube. Figure 4.4 shows a 3-tube actuation unit prototype.

Sizing Components

The power required to achieve the linear design specifications above (20 N at 15.24 cm/sec) is 3.048 W. Thus, we chose a 10 W, 25 mm Maxon RE series DC brushed motor (#118743) to actuate the nut and thus cause lead screw linear translation. To achieve the required speed and force given this motor, a variety of lead screw pitch and motor gearhead combinations are possible. We selected a 0.5 in/turn lead screw pitch from the range of standard 3/8 inch ACME screw pitches (1.0–0.0625 in/turn from Nook Industries, Inc.). This selection was made both for efficiency (inversely related to pitch), and because it sets the required motor gearhead near a standard value (4.4:1). There is also a 85:84 gear ratio between the motor gear and the gear affixed to the lead screw nut, a consequence of available stock sizes. The manufacturer specifies that this lead screw requires 0.101 inch-pounds of torque to achieve one pound of output force, and that its efficiency is 79%. Thus (neglecting friction and at motor stall), the actuation unit is capable of applying a linear force of 224 N. Further, (again neglecting friction) the speed when applying 20 N will be 21.0 cm/sec. The 500 count quadrature encoder resolves position with this system to 0.00143 mm.

A smaller and lighter motor is desirable to actuate the lead screw directly, because this motor must translate with the tube base. Torque and speed specifications described previously (162.4 mNm and 3.33 rev/sec) yield a power of 3.4 W. Thus we chose a 4.5 W 16 mm Maxon RE series DC brushed motor (#118730). Using a 19:1 gearhead, with a 2:1 gear ratio on the pulleys of the toothed-belt transmission
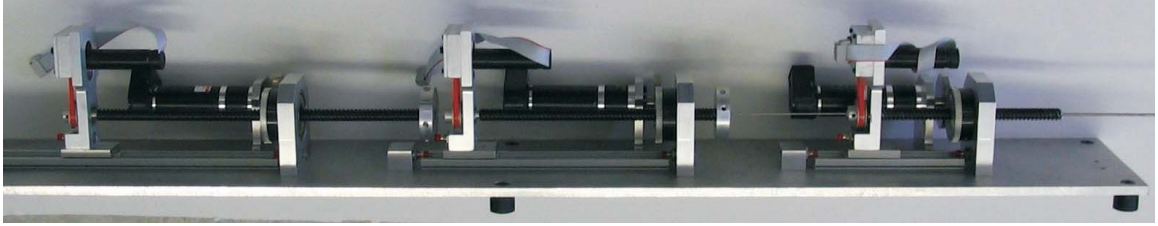
Figure 4.4: Photo of a three tube, six-DOF actuation unit prototype.

between motor and lead screw implies that the system is capable of 1094.4 mNm at stall, and 200 rev/sec while applying 162.4 mNm. The 512 count quadrature encoder resolves position to 0.00463°.

4.2.2 Manual Actuation Mechanism

The manual actuation mechanism (used for the experiments described in Section 4.6) provides acrylic disc handles affixed to tube bases as shown in Figure 4.5. Radial lines etched on the discs every 10° enable manual axial rotation to desired angles. The linear translations of the discs can be set using a 1 mm resolution ruler etched onto the acrylic support structure. Spring-loaded locking pins can fix wheel positions in both degrees of freedom.

4.3 Cannula Design and Mechanics

The active cannula shown in Figure 4.1 is made of three precurved Nitinol tubes, with a largest section diameter of 2.4 mm, tapering to a smallest section diameter of 0.8 mm. Forward kinematics an active cannula is a description of complete de-
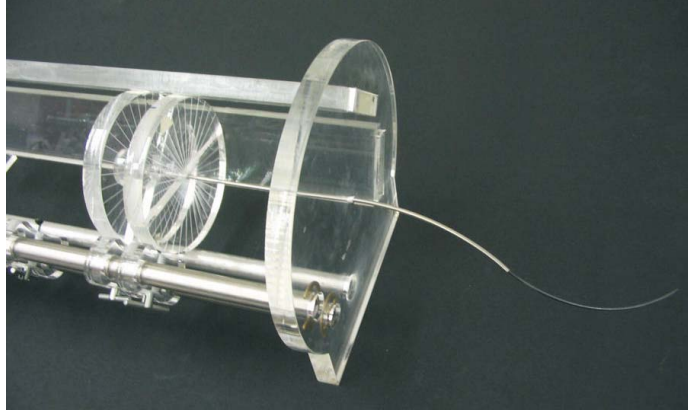
Figure 4.5: Manual actuation mechanism. Both tube and wire have circular input handles etched to encode rotation and the support structure features a linear ruler etched to encode translation. Spring pin locking mechanisms hold wheels at desired linear and angular positions.

vice shape in terms of joint variables: component tube linear positions and rotations. This requires a model of how precurved tubes cause one another to bend. The one "link" model developed this section maps from the axial rotation angles of concentric curved tubes to their common equilibrium curvature and bending plane. The modeling process also provides various design insights, notably curvature limits to prevent self-plastic deformation of cannula component tubes. The main (experimentally validated) assumptions in this model are that tubes can be considered to directly apply moments to one another, and that (due to circular component tube precurvatures) those moments can be considered constant along the length of a link.

All previous studies of active cannulas and similar needle designs mentioned in Section 4.1.2 have been restricted to component tubes that have a straight transmission with a circular constant curvature section at one end [48,65,118,145,146,178,179]. While this is also our primary concern in this paper, we note that the models presented here are in principle general enough to account for component tubes with
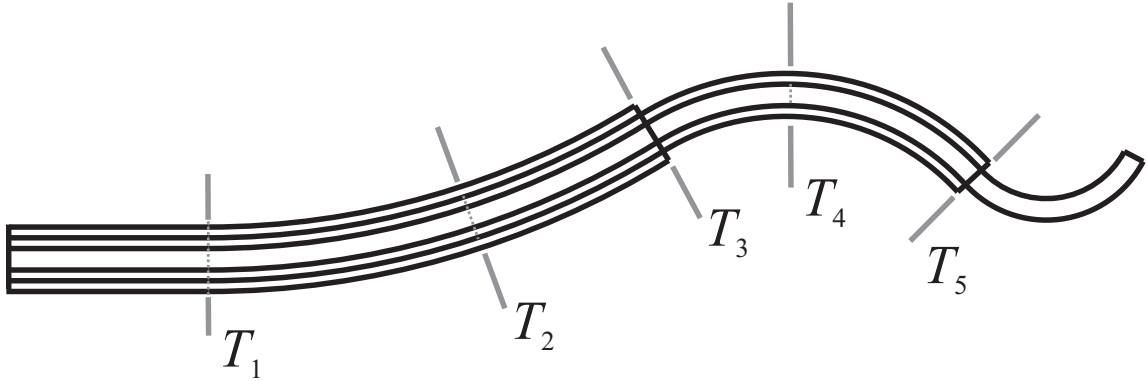
Figure 4.6: The "links" or regions of unique overlap of a 3–tube cannula composed of tubes like those in Figure the upper image of Figure 4.7. Links start and end at transition points, and the jth link is between T_j and T_{j+1}. In this configuration, the largest tube transitions from straight to the left of T_1 to curved to the right. The same is true of the middle tube at T_2 and the smallest tube at T_4.

multiple constant curvature and straight sections along their lengths, as illustrated in Figure 4.7, via increasing the number of transition points and thus the number of links considered.

4.3.1 Active Cannula Features

There are several particularly noteworthy theoretical and practical features of active cannulas. In comparison to many previous continuum robot designs, active cannulas can be smaller and incorporate more bending sections. While it is often challenging to add additional bending sections to other continuum robot designs, an important feature of the active cannula is that additional sections can be easily added by increasing the number of tubes.

The central idea of the active cannula is the precurvature of the component tubes. Considering only circular precurvature (as we do in this chapter) simplifies analysis
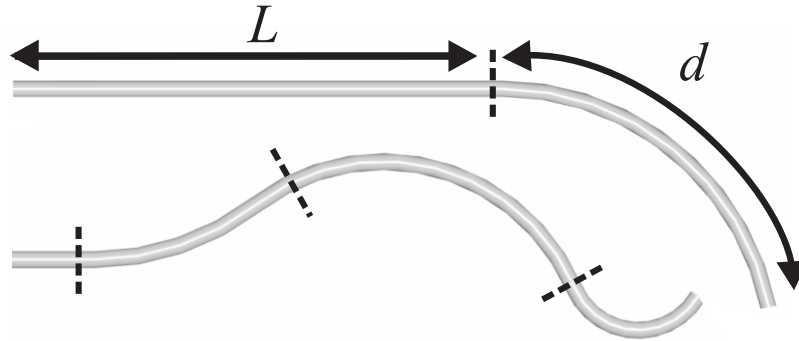
Figure 4.7: (Top) Tubes used in all active cannula studies to date (including this dissertation), consist of a straight transmission of length L, with a constant curvature section of length d at one end. (Bottom) Our models presented here are in principle general enough to account for piecewise circular/straight tubes with multiple transition points.

and design. However, we note that other variable curvature shapes may be suited to specific surgical interventions, and may even be customized individually to meet patient-specific operative goals.

While prototype active cannulas discussed in this chapter are all made from Nitinol (e.g. Figure 4.1) we note that active cannulas may be made of any elastic material, including plastics. Desirable characteristics are materials that can sustain high strain without damage, and have high torsional rigidity compared to their flexural rigidity. However, Nitinol also has additional potential benefits that have not yet been exploited. While the prototype active cannulas described in this paper make use of only the superelastic properties of Nitinol, it is worth noting that if suitable heat transmission mechanisms are used, the design may be able to simultaneously take advantage of both the superelastic and shape memory effects of Nitinol.

Features of the active cannula design that seem particularly appealing are that miniaturization *enhances* dexterity (smaller tube diameters permit larger precurva-

tures as discussed in Section 4.3.3), and that compliance is tunable through design (adjusting individual tube stiffnesses by choosing wall thickness, diameters, preformed shapes, and/or material properties), as well as configuration. Compliance (whether intentionally tuned or not) is inherent in the design, and is expected to enhance active cannula safety, reducing potential tissue damage in the event of inadvertent cannula/tissue contact.

It is often convenient to model snake-like robots as a mathematical curve (e.g. a series of circular arcs [94], or more general curves). Robot kinematics is approximated, more or less accurately depending on the robot and the configuration, as the curve. However, with the active cannula's circular precurvatures, and provided model assumptions drawn from experimental observation [145, 178] are accurate, no approximation is needed. The active cannula will actually be a series of circular arcs. Further, when representing many other continuum robot designs as a mathematical curve, it can be quite challenging to fully describe the effect of physical joint limits, and the robot may inadvertently damage itself [93]. The properly designed active cannula (Section 4.3.3) is not subject to this danger, since it combines both elastic elements and force transmission elements directly into the extensible backbone. Active cannulas have no joint limits and no danger of self-damage anywhere in their configuration spaces. Any joint limits that are present are an artifact of a specific actuation unit design, and actuation units can in principle be constructed to allow as much motion as desired, as is the case with our prototype (the lead screws can be lengthened).

4.3.2 Precurvature Limits

The selection of the initial curvature to be preset into each tube is an important design consideration. Without specific clinical requirements, smaller radii of precurvature are generally desirable, since they enable the cannula to negotiate tighter turns within anatomy. However, if the radii of precurvature are chosen too small, the cannula may damage itself (plastically deforming one or more of its component tubes) at certain positions in its configuration space.

While some medical interventions may not require access to the full configuration space (for example, one or more tubes may not be required to perform 360° rotations) and thus permit smaller radii of curvature, it is generally desirable to design tube precurvatures to eliminate the possibility of active cannula self-damage. This is accomplished by ensuring that the maximum strain in all component tubes is maintained within the elastic region for all possible robot configurations.

While fatigue life is another factor that can limit maximum curvature in continuum robots, active cannulas are intended to be disposable medical devices. This possible due to their mechanical simplicity. Bulk costs of Nitinol tubing are also low enough to make disposable active cannulas an economically feasible and attractive option. Thus, the cycle-life of an individual active cannula will be low, and fatigue is not expected to be a limiting factor in active cannula curvature design. Thus, material recoverable strain is expected to be the limiting factor in choosing active cannula precurvatures.

Since superelastic materials can sustain high strain without plastic deformation,
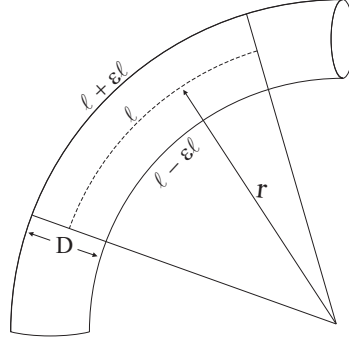
Figure 4.8: Relationship between tube wall length changes and strain.

we selected Nitinol (a superelastic alloy of nickel and titanium) as the material for the tubes in our initial prototype. Nitinol has been reported to sustain recoverable strains of as much as $\varepsilon = 11\%$ [56], but most estimates place recoverable strain near 8%.

For small diameter tubes, this corresponds to a large curvature, or equivalently a small radius of curvature. Figure 4.8 shows a small section of initially straight tube that has been curved into a circular shape by an external force distribution (not pictured). The midline length is ℓ, as are the initial lengths of the top and bottom surfaces of the tube. When the initially straight tube is bent into the circular shape shown, the top and bottom surfaces are lengthened and shortened, respectively, by a fraction ε of their initial length. The arc length ℓ of a section of radius r and angle ϕ is given by $\ell = r\phi$. The arc length of the bottom surface of the tube is thus given by

$$\ell - \varepsilon\ell = \left(r - \frac{D}{2} \right) \phi. \tag{4.1}$$

Substituting $\frac{\ell}{r}$ for ϕ and simplifying, we arrive at an expression for the radius of

curvature as a function of strain,

$$r = \frac{D}{2\varepsilon} \quad \text{or equivalently,} \quad \kappa = \frac{2\varepsilon}{D}. \tag{4.2}$$

Thus, using 8% strain ($\varepsilon = 0.08$) and a 1 mm tube, the minimum possible circular radius around which it is possible to deflect a straight Nitinol tube without plastic deformation is 6.25 mm.

The situation differs slightly when straightening an initially curved tube (rather than curving an initially straight tube). In this case, the bottom surface begins shorter than the top surface, and so reaches its strain limit first. Accounting for this requires a minor modification to the above analysis, and one can show that the minimum radius of curvature is now

$$r = \frac{D}{2\varepsilon} + \frac{D}{2} \quad \text{or equivalently,} \quad \kappa = \frac{2\varepsilon}{D(1 + \varepsilon)}. \tag{4.3}$$

Note that since ε is small, $\frac{D}{2} << \frac{D}{2\varepsilon}$. Thus, there will generally be little difference (in terms of curvature limit) between straightening an initially curved tube or curving an initially straight tube.

However, in either case the curvature of the tube is inversely proportional to tube outer diameter D. Thus, smaller tubes can sustain higher preset curvatures. This means that as the design is miniaturized, it will be able to reach around tighter corners, enhancing its dexterity. Tradeoffs for enhancing dexterity in this manner may be a reduction in stiffness and/or size of the central working channel.

Other design considerations may necessitate choosing a curvature somewhat less than this maximum value. For example, finite torsional stiffness means that if a tube is expected to smoothly rotate 360° within another tube (with acceptable elasticity

release near bifurcation, as described in Sections 4.4–4.5), one may have to choose a curvature less than the theoretical maximum for each tube.

Another possible design criteria for curvatures is to choose them to preclude cannula self-damage. Generally one or more tubes in the active cannula will have to bend back upon itself (further than straight) to "negative curvature". To evaluate the design implications of this (Section 4.3.4), we must first examine the effect of precurved coplanar tubes on one another.

4.3.3 In-Plane Beam Mechanics

If several precurved tubes are placed concentrically, their curvatures will "interfere" with one another, causing bending and making the combined shape different from the natural rest shape of individual tubes. It is this interference effect, combined with both rotation and extension–retraction of the tubes, that we use to change the shape of the active cannula. To describe the complete shape of the active cannula, we must first develop a model for the shape of a single "link" composed of several overlapping concentric curved tubes. Provided the model assumption that tubes can be considered to directly apply moments to one another is valid (the rationale for which is described below), each link will be a circular arc with an associated curvature and plane. The circularity of links has been experimentally observed in that circular arcs are capable of closely fitting images of active cannula shape [145, 178], lending support to the idea that tubes can be considered to directly apply moments to one another.
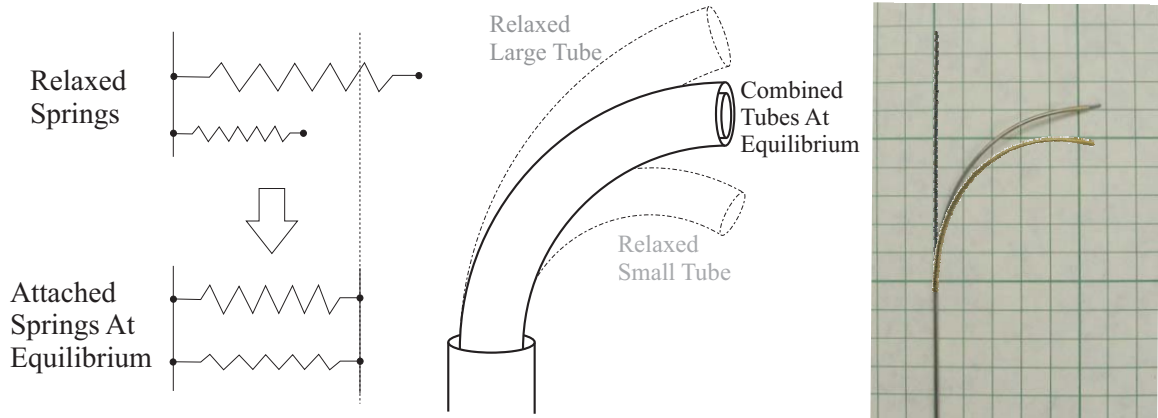
Figure 4.9: (Left) Parallel spring position equilibrium. (Middle) Analogous curved tube equilibrium. Dashed lines indicate natural tube curvatures, solid lines show the effect of placing tubes inside one another. (Right) Photograph of experiment. Initially straight wire and initially curved tube shapes are superimposed on a photograph of the combined wire and tube.

Figure 4.9 shows the effect of concentric tubes of different precurvatures on one another in the planar case. Here, the tubes have not been axially rotated with respect to one another and their natural curvature planes are aligned. The Bernoulli-Euler beam equation describes the instantaneous curvature of a beam with respect to arc length as

$$\kappa = \frac{d\phi}{ds} = \frac{M}{EI},\tag{4.4}$$

where ϕ is the angle measured from the tangent vector, s is arc length, M is the moment applied to a differential element, E is the Modulus of Elasticity (Young's Modulus), and I is the cross-sectional moment of inertia.

Using circular preset tube curvatures permits an idealization of the beam equation. Because the curvature is constant for each tube, the tube will apply a constant moment on the tubes exterior to or within it, namely

$$M = EI\Delta\kappa.\tag{4.5}$$

144

If the tubes are axially aligned so that they naturally curve in the same plane, Equation 4.5 is analogous to Hooke's law for a linear spring, i.e. "$F = K\Delta X$", as illustrated in Figure 4.9. In the analogy, the bending stiffness, EI, of a tube corresponds to the spring constant, the moment, M, corresponds to the linear force, and curvature, κ, is a "position" variable. Just as we can describe the equilibrium position of linear springs of different lengths and stiffnesses when connected in parallel by a force balance, we can describe the resultant curvature of two overlapping tubes whose natural planes of curvature are aligned by

$$\kappa = \frac{E_1 I_1 k_1 + E_2 I_2 k_2}{E_1 I_1 + E_2 I_2} \quad \text{or} \quad \kappa = \frac{\sum_{i=1}^{n} E_i I_i k_i}{\sum_{i=1}^{n} E_i I_i} \tag{4.6}$$

for n tubes, where k_i are the preformed curvatures of the individual tubes. This model is verified experimentally in Section 4.3.5.

4.3.4 Design Implications of Tube Interaction

Rotating one tube 180° with respect to the other is analogous to attaching a linear spring to the other side of the wall, so that its initial position is now $-x$ ($-\kappa$ for the tube). Thus, the equilibrium position of the more compliant of the two springs will, in general, be on the opposite side of zero from where it begins. For the tubes, this corresponds to bending further than straight (further than zero curvature). We can define $\Delta\kappa_{\max}$ for each tube as $\Delta\kappa_{\max} = \kappa_o - \min(\kappa_{eq})$. The minimum κ_{eq} will occur when all other tubes are rotated 180° with respect to the tube in question. The $\Delta\kappa_{\max}$ values for each tube must be kept at or below the bounds in Equation 4.3, to prevent the possibility of plastic deformation in any tube for all possible active

cannula configurations.

4.3.5 In-Plane Experimental Validation

We experimentally validated the in-plane beam mechanics model Equation 4.6 using curved Nitinol tubes and straight wires as shown in Figure 4.9. Table 4.1 illustrates our results. The Nitinol tubes were plastically deformed to an initial curvature k_i. The wires were initially straight, with $k_i = 0$. Photographs of each tube was taken against the 5 mm grid both before and after wires were inserted. The best-fit circle was then determined manually by examining the photographs and adjusting the diameter of a fitting circle until it closely matched the curvature in the photograph. We estimated the error associated with fitting a circle in this way to be 10% of the actual circle radius. It would be preferable to have Nitinol preshaped by the manufacturer in the desired circular shape, but this would have added significant cost at the very small quantities used in this study. It is also be possible to heat set a curvature into straight Nitinol tubes after purchase, but this is a delicate process. Nitinol requires a specific heat-time profile that is strongly dependent in small changes in composition of the alloy to set a shape while retaining superelasticity.

Tube			Wire		Combined	
ID	OD	κ	OD	κ	r meas	r pred
(mm)	(mm)	(1/mm)	(mm)	(1/mm)	(mm)	(mm)
0.622	0.800	0.044	0.430	0	26.0	25.5
0.965	1.27	0.020	0.800	0	62.5	61.2
1.47	1.78	0.021	1.30	0	75.5	72.8
2.01	2.39	0.028	1.60	0	49.8	50.5

Table 4.1: Verification of Bernoulli-Euler based beam mechanics model.
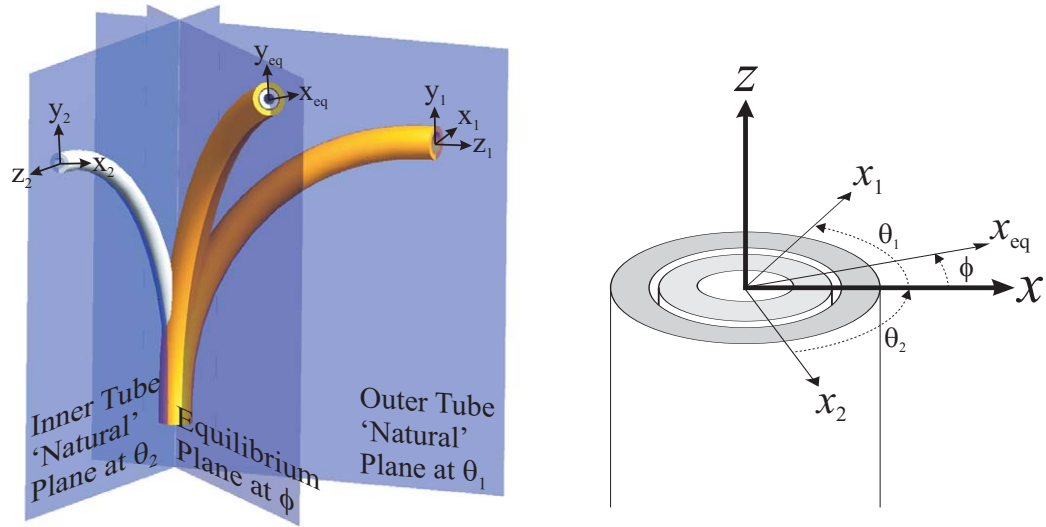
Figure 4.10: (Left) If two concentric curved tubes are axially rotated with respect to one another, they will reach a minimum energy equilibrium between their individual or 'natural' planes. They will also begin to straighten from the curvature they would exhibit with aligned natural planes. (Right) Cross-sectional view of tubes at link base. Assuming torsional rigidity this is also the cross section anywhere along the link.

4.3.6   Axial Tube Rotation

When curved tubes are rotated axially, their natural planes of curvature are no longer aligned and the direction of the bending moments they apply changes. In addition to bending moments, a torsional moment is also generated by such motion. We will begin in this section by considering bending only, and proceed to incorporate torsion to the model in Section 4.3.8.

Beam Mechanics Model with Rotation

Intuitively, if two precurved tubes with same stiffness (EI) and initial curvature k are placed within one another and rotated 90° with respect to one another, one would expect the plane of the combined tubes to be directly between their natural planes,

at 45°. One would also expect them to straighten out somewhat, since at 180° they ought to be completely straight. This is illustrated in Figure 4.10. If the tubes do not have the same stiffness, then the combined plane should shift toward the stiffer tube.

This intuition can be formalized in terms of the beam mechanics described earlier. Tubes whose natural planes are rotated with respect to one another exert a moment on one another about their respective x axes, caused by their initial precurvature about this direction. Figure 4.10 shows a cross-sectional view of the tubes inside one another. The tubes are rotated by angles θ_i, and the equilibrium plane angle is ϕ.

As before, each tube applies $M = EI(\Delta\kappa)$, but now this moment has two component projections on the base frame x and y axes. Assuming torsional rigidity, the component projections are the same for the x and y axes of any copy of the base frame slid along the link in the z direction. Summing the moments about x and y yields

$$\chi = \frac{\sum_i E_i I_i k_i \cos\theta_i}{\sum_i E_i I_i} \quad \text{and} \quad \gamma = \frac{\sum_i E_i I_i k_i \sin\theta_i}{\sum_i E_i I_i}, \tag{4.7}$$

respectively.

Assuming infinite torsional rigidity, Equation 4.7 would be sufficient to describe the shape of a complete active cannula made up of several such links (as described in Section 4.4). However, since these are superelastic tubes, torsional deformation will occur. It will be particularly important in the straight transmission sections of the tubes that lie between the actuators and the first curved link, since these transmissions are long relative to the curved section lengths.
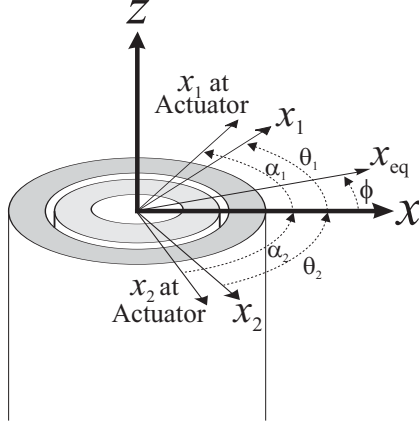
Figure 4.11: When transmissional torsion is included, actuator inputs are no longer equivalent to link base angles for each tube.

4.3.7 Transmissional Torsion

If transmissional torsion between actuators and the first curved link is included in the model, link-base tube angles (θ_i) will no longer be the same as actuator input angles (α_i). The cross section of the tubes will then be as shown in Figure 4.11.

4.3.8 Flexural and Torsional Elastic Energy

To determine link base angles, we will use a minimum energy strategy (Section 4.4.2). Doing so requires expressing the total energy of the cannula using both bending and torsional terms. The elastic energy of a beam of length ℓ in pure bending is

$$U_{\text{bend}} = \int_0^{\ell} \frac{M(s)^2}{2EI} ds. \tag{4.8}$$

When the moment is constant along the length of the beam, this reduces to

$$U_{\text{bend}} = \frac{EI\ell}{2} \Delta\kappa^2. \tag{4.9}$$

Torsional energy for a beam is given by

$$U_{\text{tors}} = \int_0^L \frac{\tau(s)^2}{2GJ} ds, \tag{4.10}$$

where τ is torque applied, G is the shear modulus, J is the polar moment of iner-
tia. When torque is constant along the length of the beam (as it is for the straight
transmission sections), and the angle between ends of the beam is $\alpha - \theta$, this reduces
to

$$U_{\text{tors}} = \frac{GJ}{2L}(\alpha - \theta)^2. \tag{4.11}$$

In contrast to bending moments, torsional moments generated by tube interaction
will not be constant along the curved links, as they are in the straight transmissions.
The above energy relationships facilitate the energy method used for kinematics in
the next section.

4.4 Kinematics Via Minimum Energy

The kinematics of continuum and hyperredundant robots are often decomposed
into two mappings. One is from actuator (joint) space to arc parameters (curvature,
plane, and length of each section), while the other is from arc parameters to Cartesian
positions of the robot. We follow a similar strategy in the analysis of the active
cannula. The first mapping (Sections 4.4.1 and 4.4.2) is generally robot-specific,
since the type of actuators and design of the robot strongly influence how actuators
affect arc parameters. The mapping from arc parameters to shape (Section 4.4.3), on
the other hand, is common to all robots that can be modeled as piecewise constant
curvature.

The shape of an active cannula is defined by a sequence of unique overlap regions ("links") between transition points T_j, as shown in Figure 4.6. Each of these links remains circular both by assumption and observation [145,178], although the bending plane and curvature change as tubes are axially rotated. Thus, an active cannula has piecewise constant curvature, consisting of a series of constant curvature links, each tangent to adjacent links.

4.4.1   Determining Link Lengths

The first step in describing the shape of an active cannula is determining the number of links and link lengths. These are defined by component tube transition point locations, which are functions of tube preshaped geometry (Figure 4.7) and translational "joint" positions of tube bases. These combine to create a sequence of links between transition points as shown in Figure 4.6. For the 3–tube active cannula illustrated (where each tube has a straight transmission followed by a single circular arc), there are 5 curved links. More generally, n tubes result in $2n - 1$ links (or $2n$, if an initial straight link is included). The length of some links reach zero when transition points align. It is straightforward to determine the lengths of the links in the cannula, given actuator displacements and component tube geometries.

For the example in Figure 4.6, the lengths of the m (in this case five) regions of overlap $\ell_j, j \in \{1, \ldots, m\}$ are given by the actuator translational positions of the n
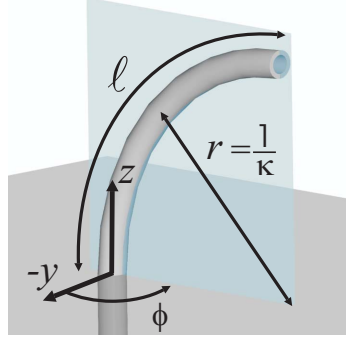
Figure 4.12: The arc parameters of a link of curved tube consist of curvature (κ), equilibrium plane angle (ϕ), and arc length (ℓ_j), respectively.

tubes $\rho_i, i \in \{1, \ldots, n\}$, and the lengths of the curved portion d_i of each tube as,

$$\ell_1 = \rho_2 - \rho_1, \qquad \ell_4 = \rho_2 + d_2 - \rho_3,$$

$$\ell_2 = \rho_1 + d_1 - \rho_2, \quad \ell_5 = \rho_3 + d_3 - \rho_2 - d_2. \qquad (4.12)$$

$$\ell_3 = \rho_3 - \rho_1 - d_1,$$

A general procedure easily amenable to software implementation for determining all ℓ_j

is to sort transition points in terms of arc length, with link lengths given by differences

between adjacent transition points. We also note that if component tubes themselves

have more than one transition point, additional active cannula links are the result.

4.4.2   From Joint Space to Arc Parameters

Active cannula joint space is parametrized by axial translations, ρ, and rotations,

α, applied at the base of each tube, namely $q = (\rho_1, \alpha_1, \ldots, \rho_n, \alpha_n)$. In what follows,

the subscript $i \in \{1, \ldots, n\}$ refers to tube number, while $j \in \{1, \ldots, m\}$ refers to

link number. Cannula links are circular segments described by the arc parameters

curvature, plane, and arc length (κ, ϕ, and ℓ), as shown in Figure 4.12. The mapping

from q to ℓ was described in the previous section, while the mapping from q to (κ, ϕ) can be accomplished by generalizing the single-link model described above, as follows.

Attach a coordinate frame, T_j, at the base of the link by sliding a copy of the cannula base frame along the backbone (without rotation about z) to the base of the link. The model then yields x and y curvature components for the link in the link frame as

$$\chi_j = \frac{\sum_i E_i I_i k_{i,j} \cos \theta_{i,j}}{\sum_i E_i I_i} \quad \text{and} \quad \gamma_j = \frac{\sum_i E_i I_i k_{i,j} \sin \theta_{i,j}}{\sum_i E_i I_i},$$

respectively. The sums over $i \in \Lambda_j$ only include the tubes that overlap the jth link. Since the intrinsic (preformed) curvature is piecewise constant along each tube, $k_{i,j}$ denotes the intrinsic curvature of the ith tube in the jth link. Note that these values change as a function of the actuator translations, because the overlapping regions change as described above, i.e. $k_{i,j} = k_{i,j}(\rho)$. E_i is the elastic modulus, I_i is the cross-sectional moment of inertia, and $\theta_{i,j}$ is the axial i^{th} tube angle about the jth link frame z axis. There is a direct relationship between curvature components and arc parameters, namely

$$\phi_j = \tan^{-1}\left(\frac{\gamma_j}{\chi_j}\right), \quad \text{and} \quad \kappa_j = \sqrt{\chi_j^2 + \gamma_j^2}. \tag{4.13}$$

Neglecting torsional compliance completely (that is, assuming infinite torsional rigidity), $\theta_{i,j} = \theta_{i,0} \equiv \alpha_i$ for all j, which results in a direct symbolic mapping (Equation 4.13) from actuator space to arc parameters for each link. However, when transmissional torsion is included, $\theta_{i,1}$ no longer equals actuator input α_i, because the straight transmission will "wind up" as torque is applied at the actuators. Since transmissions are generally long compared to curved sections, we assume that tubes

can be modeled as infinitely torsionally stiff beyond T_1, implying that $\theta_{i,j} = \theta_{i,1} \equiv \psi_i$, for all $j > 1$. With these definitions, applying Equations 4.9 and (4.11 in all directions for all tubes yields the total elastic energy stored in the system,

$$
U(\psi_1, \ldots, \psi_n) = \underbrace{\sum_{i=1}^{n} \frac{G_i J_i}{2L_i} (\alpha_i - \psi_i)^2}_{\text{transmission torsion}}
$$

$$
+ \underbrace{\sum_{j=1}^{m} \sum_{i \in \Lambda_j} \frac{E_i I_i \ell_j}{2} (\chi_j - k_{i,j} \cos(\psi_i))^2}_{x \text{ direction bending}}
$$

$$
+ \underbrace{\sum_{j=1}^{m} \sum_{i \in \Lambda_j} \frac{E_i I_i \ell_j}{2} (\gamma_j - k_{i,j} \sin(\psi_i))^2}_{y \text{ direction bending}}, \quad (4.14)
$$

where G is the shear modulus, J is the polar moment of inertia, L is the length of straight transmission between actuator and curved section of tube, and as mentioned previously $i \in \Lambda_j$ are the tubes present in the jth link.

We assume that actuator inputs influence the system "adiabatically" in the sense that as we move the actuators, the system remains at a local minimum energy. Thus the angles at the end of the straight transmission $(\psi_1, \ldots, \psi_n)$ are always assumed to be at a local minimum of Equation 4.14.

As we describe in Section 4.5, there can be multiple stable local minima of Equation 4.14. Thus the forward kinematics, given the actuator states, is not necessarily a unique mapping. The particular minimum of Equation 4.14 in which the robot finds itself is dependent on the path traversed through through joint space to reach current joint angles.

To obtain the minimum of the energy function Equation 4.14, one can solve for the critical points where the gradient equals zero. This leads to a set of transcendental
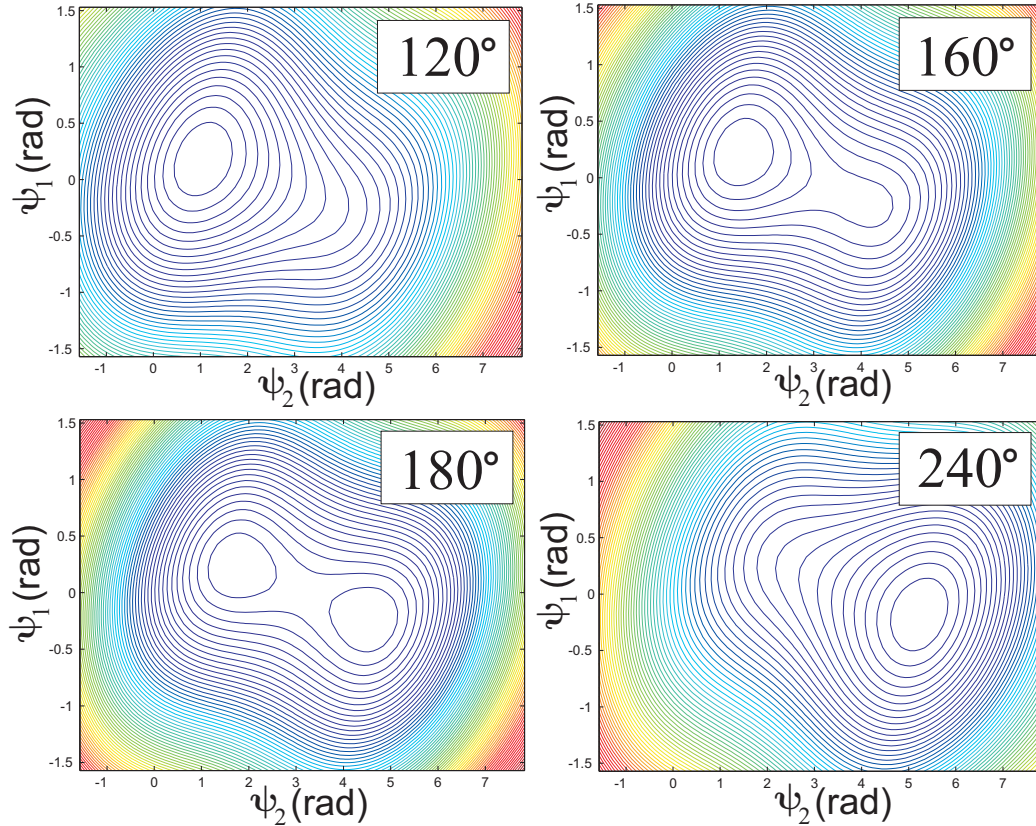
Figure 4.13: Contour plots of the energy landscape as the angular difference between the tube bases is increased. Angular difference between the base inputs of the two tubes is listed in the upper right corner of each plot. For small angular differences, there is only one global minimum. As the angular difference approaches 180°, two appear. Beyond 180°, the new minimum becomes the global minimum, and eventually the only minimum. These plots are for the 'partial overlap' experiment in Section 4.6 and are made using nominal parameter values.

equations, which can be solved numerically using a variety of techniques, including Newton's method.

4.4.3 End Effector Pose

The shape of the cannula is defined by the arc parameters and the product of exponentials formula. Using the notation of Chapter 3 (i.e. [123]), the joint twists

associated with arc parameters are,

$$\xi_\phi = \begin{bmatrix} 0 & 0 & 0 & 0 & 0 & 1 \end{bmatrix}^T \quad \text{and} \quad \xi_j = \begin{bmatrix} 0 & 0 & 1 & \kappa_j & 0 & 0 \end{bmatrix}^T. \tag{4.15}$$

The full kinematics of the mechanism is then given by the product of exponentials formula,

$$g = \prod_{j=1}^{m} e^{\left(\widehat{\xi_\phi}(\Delta\phi_j)\right)} e^{\left(\widehat{\xi_j}\ell_j\right)} \tag{4.16}$$

where $\Delta\phi_j = \phi_j - \phi_{j-1}$ and $g \in SE(3)$ is the transformation from cannula base to tip. Thus, each cannula link contributes a pair of exponentials to the overall kinematics, and the pairs are written left to right in order of increasing link number.

4.5 The 3–Link Case

For the remainder of this chapter we consider the specific case of three links, which corresponds to the prototype with which we perform experimental validation and parameter fitting in Sections 4.6.3 and 4.6.4. For $n = 2$ we have $m = 2n - 1 = 3$ regions of overlap, only the middle of which contains two curved tubes. In this case the energy (Equation 4.14) is

$$U(\psi_1, \psi_2) = \frac{c_1}{2}(\alpha_1 - \psi_1)^2 + \frac{c_2}{2}(\alpha_2 - \psi_2)^2 + \ell_2 c_3 \left(\frac{k_1}{2k_2} - \cos(\psi_1 - \psi_2) + \frac{k_2}{2k_1} \right) + \frac{\ell_1}{2} c_4 k_1^2,$$

where $c_1 = \frac{G_1 J_1}{L_1}, c_2 = \frac{G_2 J_2}{L_2}, c_3 = \frac{E_1 I_1 E_2 I_2 k_1 k_2}{E_1 I_1 + E_2 I_2}$, and $c_4 = \frac{E_1 I_1 E_2 I_2}{E_1 I_1 + E_2 I_2}$. The gradient with respect to ψ is then

$$\nabla U = \begin{bmatrix} -c_1(\alpha_1 - \psi_1) + \ell_2 c_3 \sin(\psi_1 - \psi_2) \\ -c_2(\alpha_2 - \psi_2) - \ell_2 c_3 \sin(\psi_1 - \psi_2) \end{bmatrix} = 0, \tag{4.17}$$

156

where the unknowns are (ψ_2, ψ_1), and (α_1, α_2) are the inputs.

Adding the two Equations in 4.17 yields $\psi_2 = \frac{c_1}{c_2}(\alpha_1 - \psi_1) + \alpha_2$, which when substituted back into Equation 4.17 yields

$$\psi_1 - \alpha_1 = \ell_2 b_1 \sin(\alpha_2 + b_2\alpha_1 - (1 + b_2)\psi_1), \tag{4.18}$$

where

$$b_1 = \frac{c_3}{c_1} \quad \text{and} \quad b_2 = \frac{c_1}{c_2}. \tag{4.19}$$

The transcendental Equation 4.18 can be approximately solved using a variety of techniques. Here, we use a 5th order Taylor expansion of the sine term about the most recent available previous value of ψ_1. We note that in practice on a robotic system, a close approximation for the true value of ψ_1 about which to expand is readily available, because generally the robot will only move a small amount between computer servo cycles. We choose the real root of the resulting polynomial that is closest to the previous value as the solution. While this procedure worked well for our data set (there always appeared to be one, and only one, non-complex root), a more careful solution of Equation 4.17 that is guaranteed to find all possible critical points as well as resolve the path-dependence issue is a topic left to future study. In the context of the current work, we found it sufficient to frequently inspect visually the roots returned, and to evaluate Equation 4.18 with the ψ_1 value obtained to ensure that the numerical values of the left and right hand sides are approximately equal.
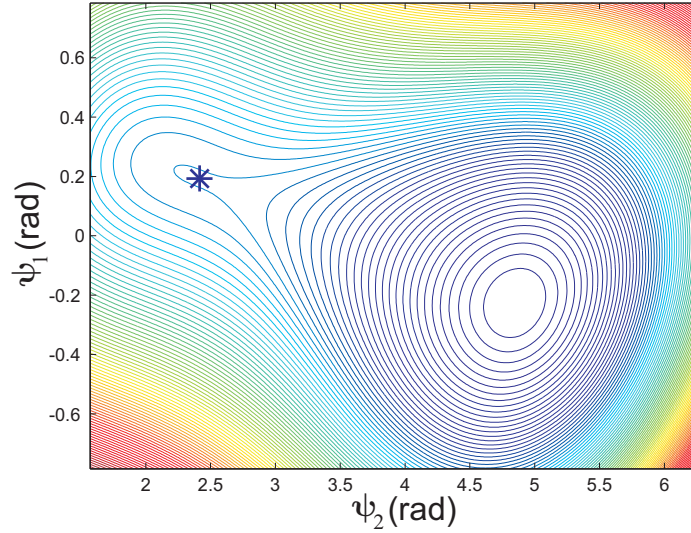
Figure 4.14: Contour plot of the energy function at the bifurcation point. The * denotes the position of the system (from Equations 4.21 and 4.22) just before bifurcation to a new minimum.

4.5.1 Bifurcation and "Snapping"

For small actuator angle differences $(\alpha_2 - \alpha_1)$, there is a unique global minimum of the Equation 4.14 with respect to ψ. As the difference between actuator input angles approaches 180°, a bifurcation in the energy landscape in the torsion angles (ψ_1, ψ_2) introduces two spurious critical points: a saddle and local minimum (see Figure 4.13). As the actuator input difference approaches 180° from below, the new minimum deepens, and the minimum in which the system rests rises, until at $(\alpha_2 - \alpha_1) = 180°$ the heights of the minima are equal. Just beyond an actuator difference of 180°, the spurious minimum actually becomes the global minimum, but the system remains in the original local minimum due to the "torsional windup" history effect. As the input angle difference continues to increase, the system remains in the local minimum until it reaches another bifurcation, at which point the local minimum disappears, leaving

158

only the global minimum above 180°. At this point the system "snaps" to the global minimum, releasing built-up torsional energy.

At a bifurcation point, the local minimum and saddle merge. This effect happens when the Hessian is singular (concavity changes) while simultaneously the gradient is zero (critical point). This is illustrated in Figure 4.14. The Hessian is singular when

$$\det\left(\frac{\partial^2 U}{\partial \psi^2}\right) = c_1 c_2 + (c_1 + c_2)\ell_2 c_3 \cos(\psi_1 - \psi_2) = 0. \tag{4.20}$$

Combining this with the zero gradient constraint (Equation 4.17), it is possible (for a fixed α_1) to solve for the ψ_1, ψ_2 and input α_2 at which the bifurcation occurs. These are given by

$$\psi_1 = \frac{1}{c_1}\sqrt{(\ell_2 c_3)^2 - \left(\frac{c_1 c_2}{c_1 + c_2}\right)^2}, \tag{4.21}$$

$$\psi_2 = \psi_1 + \cos^{-1}\left(-\frac{c_1 c_2}{\ell_2 c_3(c_1 + c_2)}\right), \tag{4.22}$$

$$\alpha_2 = \sqrt{(\ell_2 \beta)^2 + \cos^{-1}\left(\frac{1}{\ell_2 \beta}\right)}, \tag{4.23}$$

where the bifurcation parameter $\beta = -c_3/c_2 - c_3/c_1$. In Section 4.6.3 we experimentally determine input angles that cause bifurcation, and use the closed-form expression of Equation 4.23 to facilitate bifurcation parameter fitting.

4.6 Experiments and Parameter Fitting

Two types of experiments were undertaken to evaluate the ability of the model discussed above to capture cannula shape, bifurcation behavior, and endpoint position. A second goal of these experiments was to calibrate the active cannula, estimating model parameters.
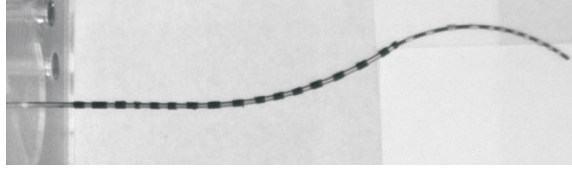
Figure 4.15: Experimental photo from one of the stereo cameras showing the cannula with fiducial markers.

4.6.1 Materials and Sensing

The manual actuation unit described in Section 4.2.2 was used for these experiments. Acrylic handles were affixed to the base of a 2.39 mm outside diameter (OD) and 2.01 mm inside diameter (ID) Nitinol tube, and 1.60 mm diameter Nitinol wire. The tube has a a 93.5 mm straight transmission and a 92.3 mm curved section created via plastic deformation with a curvature of 0.0099/mm. The wire has a 218.5 mm straight transmission and an 85 mm long circular curved section created via plastic deformation with a curvature of 0.0138/mm.

Fiducial markers (bands of black tape) were placed along the cannula for stereo triangulation as shown in Figure 4.15. The position of these fiducials were sensed using a stereo vision system composed of two calibrated Sony XCD-X710 firewire cameras running at a resolution of 1024×768 pixels. One source of error in this data collection procedure is the accuracy of manual point selection in images, which is estimated at 2 pixels or 0.6 mm. Another is fiducial size (they are not perfect points), causing small differences in intended selection locations. We estimate fiducial dimensions to introduce error of no more than the diameter of the wire itself (1.6 mm). Thus our overall vision system measurement error is estimated at approximately 2.2 mm.

4.6.2 Parameter Estimates from Physical Quantities

Writing model parameters in terms of basic material properties and measured dimensions is the first step in determining reasonable physical expectations of parameter values. This can be accomplished by combining Equation 4.19 with the formula for cross-sectional inertia of a circular section ($I = \frac{\pi}{64}(OD^4 - ID^4)$), and the relationships between shear and bending quantities ($J = 2I$ and $E = 2G(1 + \nu)$ where ν is Poisson's ratio), to produce

$$b_1 = \frac{E_2 I_2 L_1 k_1 k_2 (1 + \nu_1)}{E_1 I_1 + E_2 I_2}, \quad b_2 = \frac{E_1 I_1 L_2 (1 + \nu_2)}{E_2 I_2 L_1 (1 + \nu_1)}. \tag{4.24}$$

Reasonable parameter ranges for b_1 and b_2 can be deduced from the uncertainty in each quantity upon which they depend. Nitinol dimensions are specified by the manufacturer (Nitinol Devices and Components, Inc.) to ± 0.0010 inch, while the elastic modulus E is reported as 41–75MPa. Poisson's ratio is not quoted, but is often taken to be approximately 0.35 for Nitinol. It has also been noted that plastic deformation can increase Poisson's ratio for Nitinol to 0.5 or more [186], so we will assume a range of 0.30–0.55. Measurement errors in straight transmission lengths are estimated to be 1 mm, and measurement accuracy of curvature was estimated at 10% (Section 4.3.5). Applying error propagation, the variance in parameters b can be determined by [1]

$$\Omega_b = J_{b\varsigma} \, \Omega_\varsigma \, J_{b\varsigma}^T \tag{4.25}$$

where Ω_ς is a diagonal matrix of variances in each quantity upon which b depends (denoted by the ς), and $J_{b\varsigma}$ is the Jacobian between parameters and quantities containing

---

[1]For the sake of estimating parameter variances, we assume that physical parameter ranges are equally-scaled variances.

error $\left(J_{b\varsigma} = \frac{\partial b}{\partial \varsigma} \right)$. The square roots of the diagonal entries of Ω_b yield the variance in parameter values, based on the uncertainty in the physical quantities upon which they depend. These yield a b_1 range of 3.36–7.06 and a b_2 range of 3.14–8.45. A similar calculation for the bifurcation parameter $(\beta = -b_1(b_2 + 1))$ yields a range for β of -41.45 – -29.41. These ranges provide a basis for comparison with fitted parameter values produced by the calibration procedures described below.

4.6.3 Bifurcation Point Experiment

To experimentally determine the bifurcation parameter β for the cannula, the tube was fixed in place and the wire was rotated until the bifurcation angle was reached, at which time the cannula visibly "snapped" to the new global minimum. This was done for twelve linear translational positions in 5 mm increments for ℓ_2 from 82.3 to 27.3 mm. A sampling of this data is shown in Table 4.2. Note that the input angle at which bifurcation occurs is always more than 180°, and often significantly more. This illustrates the torsional windup that occurs in active cannulas. The β parameter was fit to this data using Matlab's `nlinfit`, which computes a nonlinear regression using least squares. Using this procedure, we estimated β at -44.91, with a 95% confidence interval of ± 2.02, which is which is near (though slightly above) the ranges described in Section 4.6.2. In Section 4.6.4 we explain how unmodeled effects should be expected to increase experimental β in this type of experiment, but we first determine β again in Section 4.6.4 through a different procedure that uses data more uniformly distributed over cannula workspace.

ℓ_2 (mm)	82.3	72.3	62.3	52.3	42.3	32.3	27.3
α_2 (deg)	295	283	265	240	225	205	200

Table 4.2: Sample experimental bifurcation angles for various lengths of curved tube/wire overlap

An important feature of active cannula bifurcation behavior is that it ceases to occur for some values of β. For a given cannula with fixed curvatures, this corresponds to a minimum length of curved tube overlap. Below this length, the energy landscape always has a single global minimum and thus it is not possible to simultaneously satisfy Equations 4.17 and (4.20. Using $\beta = -44.91$, the predicted ℓ_2 from Equation 4.23 is 22.3 mm (the value at which $\cos^{-1}\left(\frac{1}{\ell_2\beta}\right)$ becomes undefined). Minima at slightly larger ℓ_2 values will be very near one another (and very near 180°), and friction will also mask very small bifurcation motions. These effects cause a first discernible experimental cannula bifurcation at $\ell_2 = 27.3$ mm, only slightly higher than the bifurcation experiment predicted value.

It is also possible to view the point at which bifurcation ceases as a design tool. Cannula curvatures can be selected so that bifurcation is prevented even for complete overlap. For fixed curvatures, we will further explore ℓ_2 prediction comparison to calibrated parameter values using shape data.

4.6.4 Shape Experiment

Using the stereo camera system described above and with the base of the tube fixed, cannula shape information was captured for multiple angles at two distinct linear positions of the base of the wire. One, called the "full overlap" position caused

$\ell_1 = 10$ mm (tube curved, wire straight), $\ell_2 = 82.3$ mm (both curved), and $\ell_3 = 2.7$ mm (tube ended, only curved wire present). The other, called the "partial overlap" position caused $\ell_1 = 48.0$ mm, $\ell_2 = 44.3$ mm, and $\ell_3 = 40.7$ mm, with the same tube and wire combinations in each link. For the full overlap case, 15 input angles were applied at 20° increments from 0° to 280°. For the partial overlap case, 11 input angles were applied at 20° increments from 0° to 200°.

Using data collected from these experiments, we fit b_1 and b_2. The transformation between the stereo camera coordinate frame and a frame fixed at the base of the cannula was first estimated using point cloud registration [15]. Images of a 15 mm checkerboard pattern (with corners at known physical locations with respect to the cannula base frame) were captured. Sixteen corners on the checkerboard were triangulated with the stereo vision system. Since the points were coplanar, this registration was only expected to provide a rough estimate of the frame transformation. Thus six "nuisance parameters" (a 3–vector for position and a 3–vector for orientation with magnitude of rotation encoded as length) describing the cannula base frame were included in the calibration procedure, and initialized with the results from the point cloud registration.

Parameter fitting was accomplished using Matlab's `fmincon`, with angular nuisance parameter bounds set to $\pm\ 0.349^2$, from initial estimates. The objective function was the sum of Euclidean distances from experimental to theoretical 1) tip position (Equation 4.16), 2) outer tube endpoint (Equation 4.16 up to link $m - 1$), and 3)

---

[2] This is equivalent of $\pm 20°$ converted to radians. However, since magnitude is also encoded in these variables, this bound cannot be strictly thought of as an angle.

position of fiducial band nearest the cannula base (a fixed distance along the straight cannula transmission between T_0 and T_1). The optimization rapidly converged to $b_1 = 7.92$ and $b_2 = 4.11$ from a wide range of initial b_1 and b_2 values. Nuisance parameters showed only small changes during optimization, with cannula base frame orientation moving 4.4° while position of the base tape fiducial translated 1.1 mm. These small changes in nuisance parameters are reasonable given the coplanar data used to compute our initial frame transformation estimate. Average tip error was reduced from 10.1 mm (22.10 mm max) with no fitting to 3.0 mm (8.76 mm max) with fitting. Given estimated measurement error of 1 mm in individual tube straight and curved lengths, and the estimated 2.2 mm error in vision system data, a final average tip error of 3 mm appears reasonable.

Furthermore, the fitted b_2 was within the range determined in section 4.6.2, while b_1 was near it. The energy bifurcation parameter they imply ($\beta = -40.49$) is also now within the reasonable parameter range. Small differences in β compared to the bifurcation experiment (which produced $\beta = -44.91$) are the results one would expect from unmodeled torsional deformation (in the curved regions) and unmodeled friction. Both would serve to increase the bifurcation experiment estimate of β. In that experiment all data is from the edge of workspace where the highest possible cannula internal forces occur. The shape experiment used data more uniformly distributed over the workspace. If effects of friction and unmodeled torsion cause a 5.4% reduction in each experimental bifurcation angle (Table 4.2), this would account for the difference in β. Further, $\beta = -40.49$ generates the prediction that bifurcation will cease at $\ell_2 = 24.7$ mm, only 2.6 mm less than the experimental value ($\ell_2 = 27.3$ mm
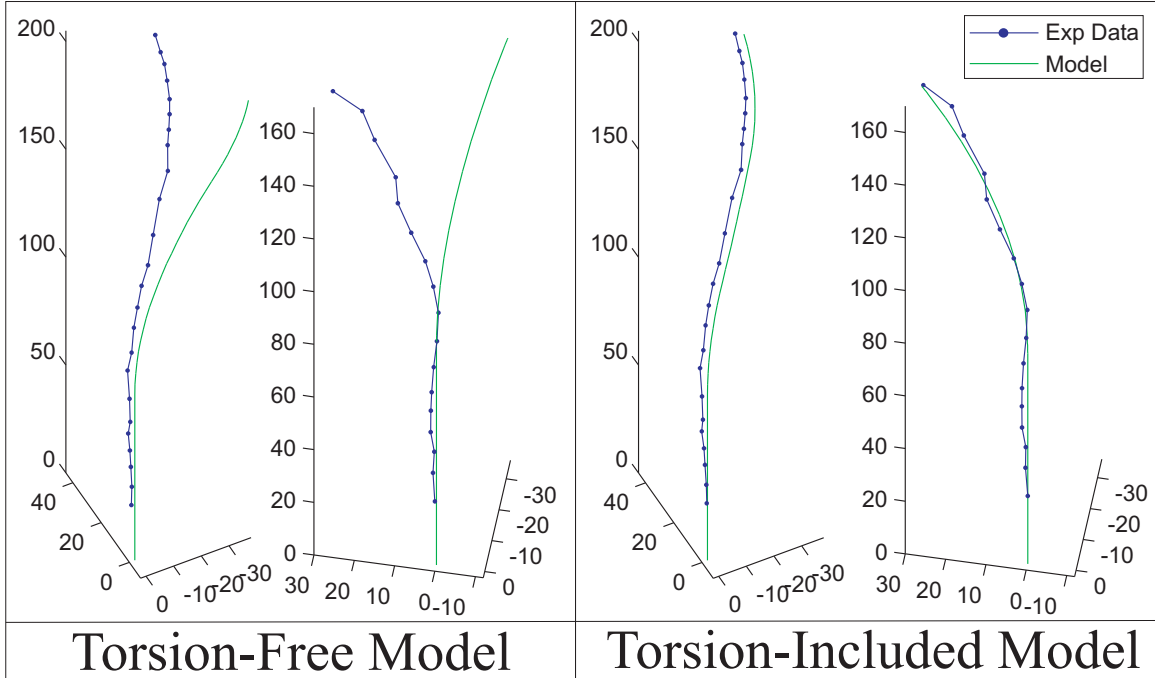
Figure 4.16: Shown above are the final angle of the partial and full overlap positions (200° and 280° respectively), the data points with the greatest overall tip error for each case above. The overlaid model predictions clearly show that torsion is a vital part of an accurate active cannula kinematic model.

found in 4.6.3), and slightly closer than the $\ell_2 = 22.3$ determined in the bifurcation experiment.

4.6.5   The Importance of Torsion

As we have described in this paper, including torsion in active cannula models leads to transcendental equations. Because of this (as outlined in Section 4.1.2), models have been proposed in the literature that assume infinite torsional rigidity and treat active cannula kinematics as a pure beam bending problem. While this is analytically attractive, our experimental results indicate that assuming infinite torsional rigidity precludes accurate prediction of active cannula shape. Without

torsion, there is only one model parameter present in the kinematic model (Equation 4.13), namely the ratio of tube flexural rigidities ($B = \frac{E_1 I_1}{E_2 I_2}$). The feasible range for B using the tolerances described in Section 4.6.2 is 0.630–4.33.

Applying the same fitting procedures described in Section 4.6.4 to the torsionless case, we first determined a tip error of 24.78 mm (54.32 mm maximum). We then fit model and frame nuisance parameters and found convergence over a wide range of initial values to $B = 3.98$, nuisance angle = 36.93°, and nuisance distance = 1.11 mm. Average tip error was reduced to 13.60 mm (31.48 mm maximum). Thus, tip errors remain large for the torsionless model even with calibration. Further, the angular nuisance parameters changed significantly during the optimization, resulting in highly inaccurate predictions of overall cannula shape throughout the workspace.

To explore the possibility that nuisance parameters were not well suited for torsionless calibration, we also applied calibration procedures to the torsionless model while holding the nuisance parameters fixed values known to give approximately correct frame transformations. Fixing nuisance parameters at initial estimates from Arun's method, we optimized B alone and determined a value of 3.59. This resulted in average tip error of 23.50 mm (53.94 mm max). The other approximately correct set of nuisance parameters available are the calibrated values found for the torsion-included model in Section 4.6.4. Holding nuisance parameters fixed at these values, we determined $B = 3.98$. This resulted in an average tip error of 22.20 mm (52.39 mm maximum).

All of the above efforts to calibrate torsionless active cannula models result in tip errors remaining large. This indicates that active cannula models that do not

include torsion are structurally insufficient for making accurate predictions of our experimental active cannula shape. They also cannot predict bifurcation behavior, since infinite torsional rigidity implies that tube angles are equal to base input angles at all points along the cannula. Results are illustrated visually in Figure 4.16 for values in the middle of the feasible range and using the initial frame estimate. If the cannula design were modified to use a different material with higher torsional rigidity for straight transmissions, the torsionless model may be more successful. However, doing so would be challenging from a prototype manufacturing standpoint. For our current all-Nitinol prototype, inability to account for torsional windup in the torsionless model makes it inaccurate except in a small neighborhood of $(\alpha_2 - \alpha_1) = 0$.

4.7 Differential Kinematics

Given active cannula forward kinematics (see Section 4.4.3) we wish to compute the spatial Jacobian, J_{st}^s, satisfying

$$V_{st}^s = J_{st}^s(q)\dot{q}. \tag{4.26}$$

We will begin by deriving the Jacobian for one link, and then use this as the building block to derive the complete active cannula Jacobian.

4.7.1 Single-Link Jacobian

The forward kinematics of a single link (omitting j and st subscripts for clarity) is given by

$$g = e^{\left(\widehat{\xi_\phi}\phi\right)}e^{\left(\widehat{\xi}\ell\right)}, \tag{4.27}$$

where, ξ_ϕ and ξ are given by Equation 4.15 and the spatial velocity is

$$\widehat{V}_{st}^s = \dot{g}g^{-1} = \left(\sum_{\iota=1}^{N}\frac{\partial g}{\partial q_\iota}\dot{q}_\iota\right)g^{-1} = \sum_{\iota=1}^{N}\left(\frac{\partial g}{\partial q_\iota}g^{-1}\right)\dot{q}_\iota,$$

for N joint variables. Inserting the definition of g, we arrive at

$$\widehat{V}_{st}^s = \sum_{\iota=1}^{N}\left[\left(\frac{\partial}{\partial q_\iota}e^{\left(\widehat{\xi_\phi}\phi\right)}\right)e^{\left(\widehat{\xi}\ell\right)} + e^{\left(\widehat{\xi_\phi}\phi\right)}\left(\frac{\partial}{\partial q_\iota}e^{\left(\widehat{\xi}\ell\right)}\right)\right]g^{-1}\dot{q}_\iota.$$

Since ξ_ϕ is constant, this simplifies to

$$\widehat{V}_{st}^s = \sum_{\iota=1}^{N}\left[\widehat{\xi}_\phi\frac{\partial\phi}{\partial q_\iota}g + e^{\left(\widehat{\xi_\phi}\phi\right)}\left(\frac{\partial}{\partial q_\iota}e^{\left(\widehat{\xi}\ell\right)}\right)\right]g^{-1}\dot{q}_\iota. \tag{4.28}$$

Since ξ varies with q_ι, its derivative is somewhat more complicated, but can be written in terms of an infinite series of nested Lie brackets [136]:

$$\frac{\partial}{\partial q_\iota}e^{\left(\widehat{\xi}\ell\right)} = \mathrm{dexp}_{\left(\widehat{\xi}\ell\right)}\left(\frac{\partial}{\partial q_i}\left(\widehat{\xi}\ell\right)\right)e^{\left(\widehat{\xi}\ell\right)}$$

where,

$$\mathrm{dexp}_A(C) := C + \frac{1}{2!}[A, C] + \frac{1}{3!}[A, [A, C]] + \ldots,$$

and

$$[A, C] := AC - CA.$$

The specific matrices we are interested in here are

$$\widehat{\xi}\ell = \begin{bmatrix} \widehat{e_1}\alpha & e_3\ell \\ 0 & 0 \end{bmatrix} \quad \text{and} \quad \left(\widehat{\xi}\ell\right)' = \begin{bmatrix} \widehat{e_1}\alpha' & e_3\ell' \\ 0 & 0 \end{bmatrix},$$

where $\alpha = \kappa\ell$ and $'$ denotes a derivative with respect to q_ι. Note that $\left(\widehat{\xi}\ell\right)$ and $\left(\widehat{\xi}\ell\right)'$ do not commute, so dexp cannot be simplified in the same manner as was possible

for the ξ_ϕ derivative. However, it can be simplified by algebraic manipulation to form sine and cosine series as follows. Writing out a few terms of dexp yields

$$\text{dexp}_{(\widehat{\xi\ell})}((\widehat{\xi\ell})') = \begin{bmatrix} \widehat{e_1}\alpha' & e_3\ell' \\ 0 & 0 \end{bmatrix} + \frac{1}{2!}\begin{bmatrix} 0 & \widehat{e_1}e_3\gamma \\ 0 & 0 \end{bmatrix} +$$

$$\frac{1}{3!}\begin{bmatrix} 0 & \widehat{e_1}^2\alpha e_3\gamma \\ 0 & 0 \end{bmatrix} + \frac{1}{4!}\begin{bmatrix} 0 & \widehat{e_1}^3\alpha^2 e_3\gamma \\ 0 & 0 \end{bmatrix} + \ldots, \quad (4.29)$$

where $\gamma = \alpha\ell' - \alpha'\ell = \kappa\ell\ell' - \kappa'\ell\ell - \kappa\ell'\ell = -\kappa'\ell^2$. The upper right entry of this matrix can now be manipulated to obtain trigonometric series:

$$e_3\ell' + \left(\frac{1}{2!}\widehat{e_1} + \frac{1}{3!}\widehat{e_1}^2\alpha + \frac{1}{4!}\widehat{e_1}^3\alpha^2 + \ldots\right)e_3\gamma$$

$$= e_3\ell' + \left[\left(\frac{1}{2!} - \frac{1}{4!}\alpha^2 + \frac{1}{6!}\alpha^4 \pm \ldots\right)\widehat{e_1} + \left(\frac{1}{3!}\alpha - \frac{1}{5!}\alpha^3 + \frac{1}{7!}\alpha^5 \pm \ldots\right)\widehat{e_1}^2\right]e_3\gamma$$

$$= e_3\ell' + \frac{1}{\alpha^2}\left[(-\cos(\alpha) + 1)\widehat{e_1} + (-\sin(\alpha) + \alpha)\widehat{e_1}^2\right]e_3\gamma$$

$$= e_3\ell' + \frac{1}{\alpha^2}\left[(\cos(\alpha) - 1)e_2 + (\sin(\alpha) - \alpha)e_3\right]\gamma.$$

Applying this in Equation 4.29 results in

$$\text{dexp}_{(\widehat{\xi\ell})}((\widehat{\xi\ell})') = \underbrace{\begin{bmatrix} \widehat{e_1}\alpha' & \left(\ell' + \frac{\gamma(\sin(\alpha)-\alpha)}{\alpha^2}\right)e_3 + \frac{\gamma(\cos(\alpha)-1)}{\alpha^2}e_2 \\ 0 & 0 \end{bmatrix}}_{\widehat{A_\iota}},$$

which was the desired result needed in Equation 4.28, yielding

$$\widehat{V}_{st}^s = \sum_{\iota=1}^N \left[\widehat{\xi}_\phi\phi'g + e^{(\widehat{\xi_\phi\phi})}\widehat{A_\iota}e^{(\widehat{\xi\ell})}\right]g^{-1}\dot{q}_i. \quad (4.30)$$

Moving g^{-1} inside the sum, and converting to twist coordinates (taking the $^\vee$ of both sides), yields the spatial Jacobian in terms of arc parameter derivatives:

$$V_{st}^s = \underbrace{\begin{bmatrix} a_1 \mid \ldots \mid a_N \end{bmatrix}}_{J_{st}^s}\dot{q}, \quad (4.31)$$

where

$$a_\iota = \begin{bmatrix} \kappa' \sin(\phi)(\cos(\kappa\ell) - 1)/\kappa^2 \\ -\kappa' \cos(\phi)(\cos(\kappa\ell) - 1)/\kappa^2 \\ \ell' - \kappa'(\sin(\kappa\ell) - \kappa\ell)/\kappa^2 \\ \cos(\phi)\,(\kappa'\ell + \ell'\kappa) \\ \sin(\phi)\,(\kappa'\ell + \ell'\kappa) \\ \phi' \end{bmatrix}, \quad \kappa \neq 0.$$

If $\kappa = 0$ then $\xi = [e_3 \; 0]^T$ and $\frac{\partial}{\partial q_\iota} e^{(\widehat{\xi}\ell)} = \widehat{\xi}\ell' e^{(\widehat{\xi}\ell)}$. In this case, $a_\iota = [0 \; 0 \; \ell' \; 0 \; 0 \; \phi']^T$.

Only one final modification, to account for nonzero initial base angle, is needed to make this result general. When applying the above formula to a multi-link robot, each link will have an initial angle from the previous link. Thus, we must substitute $(\phi_j - \phi_{j-1})$ for ϕ in the expressions above. In summary,

$$a_\iota = \begin{bmatrix} \kappa' \sin(\phi_j - \phi_{j-1})(\cos(\kappa\ell) - 1)/\kappa^2 \\ -\kappa' \cos(\phi_j - \phi_{j-1})(\cos(\kappa\ell) - 1)/\kappa^2 \\ \ell' - \kappa'(\sin(\kappa\ell) - \kappa\ell)/\kappa^2 \\ \cos(\phi_j - \phi_{j-1})\,(\kappa'\ell + \ell'\kappa) \\ \sin(\phi_j - \phi_{j-1})\,(\kappa'\ell + \ell'\kappa) \\ \phi'_j - \phi'_{j-1} \end{bmatrix}, \kappa \neq 0 \qquad a_\iota = \begin{bmatrix} 0 \\ 0 \\ \ell' \\ 0 \\ 0 \\ \phi'_j - \phi'_{j-1} \end{bmatrix}, \kappa = 0,$$

$$(4.32)$$

and

$$V^s_{st} = \underbrace{\begin{bmatrix} a_1 \mid \ldots \mid a_N \end{bmatrix}}_{J^s_{st}} \dot{q}. \qquad (4.33)$$

4.7.2 Arc Parameter Derivatives

In the preceding section we derived the Jacobian $J(\ell', \kappa', \phi')$ for an active cannula link in terms of arc parameter derivatives (with respect to joint variables). We now compute these arc parameter derivatives. Recalling from the discussion in Section 4.4.1 and the example (Equation 4.12) that $\ell(\rho)$ will be a simple algebraic function (between discrete changes as transition points pass one another), its derivative will be straightforward to compute, as shown in the examples in Section 4.7.4.

The expressions for ϕ and κ (Equation 4.13) are more complex. However, if the system evolves adiabatically (as was our assumption in forward kinematics) such that it remains at local minimum of Equation 4.14

$$\psi^* := \operatorname*{argmin}_{\psi} U(\psi),$$

then we can apply the chain rule as follows,

$$\frac{\partial \kappa_j}{\partial q} = \frac{\partial \kappa_j}{\partial \psi^*} \frac{\partial \psi^*}{\partial q}$$

and similarly for ϕ_j. The derivatives of κ_j and ϕ_j with respect to ψ^* are straightforward computations given (4.13).

We take derivatives of ψ^* with respect to q as follows. Given the adiabatic assumption and Equation 4.14, we have $\nabla U = F(q, \psi^*) = 0$, and

$$D_q F = D_1 F + (D_2 F)(D_q \psi^*) = 0.$$

If the Hessian $(D_q \psi^*)$ is invertible,

$$D_q \psi^* = -(D_2 F)^{-1}(D_1 F).$$

Thus

$$\kappa'_j = \frac{\partial \kappa_j}{\partial \psi} \left(-\frac{\partial F}{\partial \psi^*} \right)^{-1} \frac{\partial F}{\partial q_i} \quad \text{and} \quad \phi'_j = \frac{\partial \phi_j}{\partial \psi} \left(-\frac{\partial F}{\partial \psi^*} \right)^{-1} \frac{\partial F}{\partial q_i}. \tag{4.34}$$

4.7.3   Multi-Link Jacobian

Given the single-link Jacobian from Section 4.7.1, and the arc parameter deriva-tives in Section 4.7.2, it is straightforward to compute the Jacobian for a multi-link active cannula. All that is necessary is to express the individual link Jacobians in the spatial frame by applying relevant adjoint transformations,

$$J^s_{st} = J_1 + \text{Ad}_{g_{01}} J_2 + \text{Ad}_{g_{02}} J_3 + \ldots, \tag{4.35}$$

where J_j is the jth link Jacobian computed via Equation 4.33 and the individual arc parameter derivatives discussed in the previous section.

4.7.4   Examples: The 3–Link Case

We will consider two examples of the 3–link case, including an initial straight link at the base of each. The first example is when the curved portions of the tubes do not intersect, while the second is when they do. The example with no curve overlap is illustrated in figure 4.17.
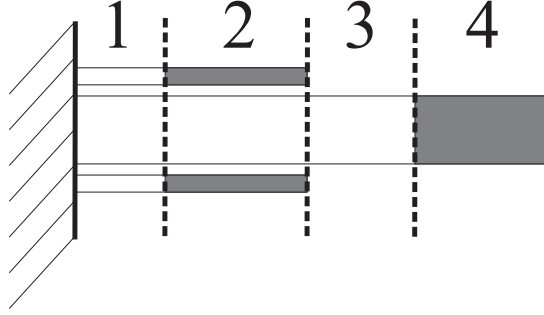
Figure 4.17: Diagram of a 2–tube, 3–link active cannula, with an initial straight base link. Shaded regions indicate where the tubes are curved. In this example curved sections do not overlap. At the wall shown, $\rho = 0$.

	Link 1	Link 2	Link 3	Link 4
ℓ	$\rho_1 - d_1$	d_1	$\rho_2 - d_2 - \rho_1$	d_2
κ	0	$\frac{E_1 I_1 k_1}{E_1 I_1 + E_2 I_2}$	0	k_2
ϕ	0 (arbitrary)	$\psi_1 = \alpha_1$	0 (arbitrary)	$\psi_2 = \alpha_2$

Table 4.3: Table of arc parameters for the case where curved portions of tubes do not overlap (Figure 4.17).

Here, the inner tube has been extended far enough out of the outer tube that its curved section (shaded region) has completely passed the curved section of the outer tube. The zero translational positions (ρ) of both tubes are when their tips align with the wall from which they protrude. Table 4.3 shows the arc parameters for this cannula. Recall that d denotes length of the curved sections, and α the angular actuator input.

Since κ and ℓ are constant for every link in this configuration, arc parameter

derivatives are simple, as are the individual link Jacobians, namely

$$J_1 = \begin{bmatrix} 0 & e_3 & 0 & 0 \\ 0 & 0 & 0 & 0 \end{bmatrix} \quad J_2 = \begin{bmatrix} 0 & 0 & 0 & 0 \\ e_3 & 0 & 0 & 0 \end{bmatrix}$$

$$J_3 = \begin{bmatrix} 0 & -e_3 & 0 & e_3 \\ -e_3 & 0 & 0 & 0 \end{bmatrix} \quad J_4 = \begin{bmatrix} 0 & 0 & 0 & 0 \\ 0 & 0 & e_3 & 0 \end{bmatrix}.$$

The situation is a bit more complex when curved regions overlap, because the curved sections now interact, forcing tubes to bend and also store torsional energy as a function of joint variables. Figure 4.18 illustrates this configuration and Table 4.4 gives arc parameter expressions. Working through the arc parameter derivatives in Section 4.7.2 produces the following:
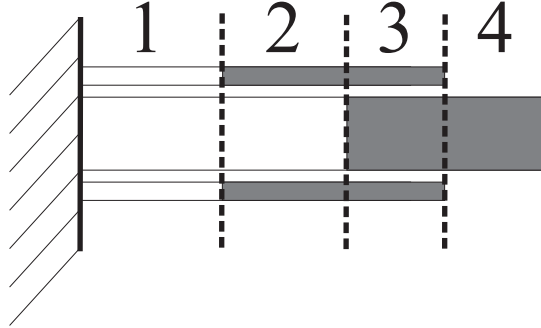
Figure 4.18: Diagram of a 2–tube, 3–link active cannula with overlapping curved sections. Shaded regions indicate where the tubes are curved.

	Link 1	Link 2	Link 3	Link 4
ℓ	$\rho_1 - d_1$	$\rho_2 - d_2 - (\rho_1 - d_1)$	$\rho_1 - (\rho_2 - d_2)$	$\rho_2 - \rho_1$
κ	0	C_1	(see below)	k_2
ϕ	0 (arbitrary)	ψ_1^*	(see below)	ψ_2^*

Table 4.4: Table of arc parameters for example with overlapping curved sections. Here $C_1 = \frac{E_1 I_1 k_1}{E_1 I_1 + E_2 I_2}$ and $C_2 = \frac{E_2 I_2 k_2}{E_1 I_1 + E_2 I_2}$.

The expressions for κ_3 and ϕ_3 are

$$\kappa_3 = \sqrt{\left(C_1 \cos(\psi_1) + C_2 \cos(\psi_2)\right)^2 + \left(C_1 \sin(\psi_1) + C_2 \sin(\psi_2)\right)^2}$$

$$\phi_3 = \tan^{-1}\left(\frac{C_1 \cos(\psi_1) + C_2 \cos(\psi_2)}{C_1 \sin(\psi_1) + C_2 \sin(\psi_2)}\right).$$

From Equation 4.5 we have

$$\nabla U = F = \begin{bmatrix} -(\alpha_1 - \psi_1) + (\rho_1 - \rho_2 + d_2)b_1 \sin(\psi_1 - \psi_2) \\[2mm] -\frac{1}{b_2}(\alpha_2 - \psi_2) - (\rho_1 - \rho_2 + d_2)b_1 \sin(\psi_1 - \psi_2) \end{bmatrix} = 0.$$

Computing the relevant matrices from Equation 4.34, we obtain

$$\frac{\partial F}{\partial \psi} = \begin{bmatrix} 1 + (\rho_1 - \rho_2 + d_2)b_1 \cos(\psi_1 - \psi_2) & -(\rho_1 - \rho_2 + d_2)b_1 \cos(\psi_1 - \psi_2) \\[3mm] -(\rho_1 - \rho_2 + d_2)b_1 \cos(\psi_1 - \psi_2) & \frac{1}{b_2} + (\rho_1 - \rho_2 + d_2)b_1 \cos(\psi_1 - \psi_2) \end{bmatrix}$$

$$\frac{\partial F}{\partial q} = \begin{bmatrix} -1 & b_1 \sin(\psi_1 - \psi_2) & 0 & -b_1 \sin(\psi_1 - \psi_2) \\[3mm] 0 & -b_1 \sin(\psi_1 - \psi_2) & -\frac{1}{b_2} & b_1 \sin(\psi_1 - \psi_2) \end{bmatrix}$$

For link 1, the derivatives are simply $\frac{\partial \ell_1}{\partial q} = [0\ 1\ 0\ 0]$, $\frac{\partial \kappa_1}{\partial q} = [0\ 0\ 0\ 0]$, and $\frac{\partial \phi_1}{\partial q} = [0\ 0\ 0\ 0]$, which are the same as in the non-overlapping case above. For link 2, $\frac{\partial \ell_2}{\partial q} = [0\ -1\ 0\ 1]$, $\frac{\partial \kappa_2}{\partial \psi} = [0\ 0]$, and $\frac{\partial \phi_2}{\partial \psi} = [1\ 0]$. For link 3, $\frac{\partial \ell_3}{\partial q} = [0\ 1\ 0\ -1]$,

$$\frac{\partial \kappa_3}{\partial \psi} = \begin{bmatrix} \frac{2C_1 \cos(\psi_1)(C_1 \sin(\psi_1)+C_2 \sin(\psi_2))-2C_1(C_1 \cos(\psi_1)+C_2 \cos(\psi_2))\sin(\psi_1)}{2\sqrt{(C_1 \cos(\psi_1)+C_2 \cos(\psi_2))^2+(C_1 \sin(\psi_1)+C_2 \sin(\psi_2))^2}} \\[4mm] \frac{2C_2 \cos(\psi_2)(C_1 \sin(\psi_1)+C_2 \sin(\psi_2))-2C_2(C_1 \cos(\psi_1)+C_2 \cos(\psi_2))\sin(\psi_2)}{2\sqrt{(C_1 \cos(\psi_1)+C_2 \cos(\psi_2))^2+(C_1 \sin(\psi_1)+C_2 \sin(\psi_2))^2}} \end{bmatrix}^T,$$

and

$$\frac{\partial \phi_3}{\partial \psi} = \begin{bmatrix} \frac{C_1(C_1+C_2 \cos(\psi_1-\psi_2))}{C_1^2+2C_2 \cos(\psi_1-\psi_2)C_1+C_2^2} & \frac{C_2(C_2+C_1 \cos(\psi_1-\psi_2))}{C_1^2+2C_2 \cos(\psi_1-\psi_2)C_1+C_2^2} \end{bmatrix}.$$

For link 4, $\frac{\partial \ell_4}{\partial q} = [0\ -1\ 0\ 1]$, $\frac{\partial \kappa_4}{\partial \psi} = [0\ 0]$, and $\frac{\partial \phi_4}{\partial \psi} = [0\ 1]$.

In summary, the Jacobian for the active cannula can be written in closed form, despite the lack of closed form forward kinematics.

4.8 Discussion

This chapter has presented kinematic and differential kinematic modeling of active cannulas. The modeling process produced a number of design tools which are summarized here in the context of a general design methodology. This is a methodology proposed for developing customized active cannulas for specific medical scenarios, and it also illustrates opportunities for future research. In approaching customization of active cannulas for a new clinical application, the general design steps are:

- *Study Clinical Objectives, Generate Design Specifications.* The designer of a customized active cannula must first translate clinical objectives into a set of design specifications. Important considerations include the payload, diameter, stiffness, and workspace required to accomplish the surgical goal. Often, doctors cannot provide specific engineering constraints. What they can provide are medical images, and detailed descriptions of the various tasks the customized cannula must perform. Physicians can also provide qualitative validation of the performance of prototypes relative to their desired objectives for the tool. Thus, it will often be necessary to iteratively develop and test prototypes. The design tools presented in this thesis provide a basis for guiding this iterative design process.

- *Consider Payload and End Effector Actuation.* One important consideration is the surgical end effector (payload) the active cannula must carry to accomplish its objectives. Examples of possible end effectors include a gripper or biopsy collection mechanism (possibly actuated by a push-pull Nitinol rod in the central

working channel), an optical fiber for visualization or energy delivery, a cautery electrode, etc. Active cannulas with no end effector will also be useful for suction. To assess the effect of end effectors on active cannula kinematics and differential kinematics, one must determine what additional forces they apply to the cannula either during actuation, or through their weight. For many possible end effectors (e.g. electrocautery wires, optical fibers), these effects are expected to be negligible. Such payloads may be included straightforwardly in the models presented in this dissertation – they will simply add an additional straight cylinder (0 mm ID tube) that spans all active cannula links.

- *Determine Maximum Tool Diameter.* The maximum diameter possible for the given surgical application will influence the maximum number of possible tubes, which affects the stiffness and workspace of the cannula. In soft tissues, for example, the maximum desirable diameter would likely be similar to commercial radiofrequency ablation needles (13-14 gauge or 2.4–2.1mm). Similar largest diameters (with smaller inner tubes) would also likely be applicable in the lung, given the 4 mm diameter of conventional bronchoscopes. However, miniaturized active cannulas will also be useful for microsurgery applications such as within the eye, and a wrist similar to an active cannula is currently being explored for this application at Columbia University [183].

- *Evaluate Stiffness.* The required stiffness of the active cannula for the surgical objective will likely be best investigated experimentally. To determine the force that the active cannula must apply, one can instrument existing tools (e.g.

during open procedures). In general, active cannula stiffness will be dependent on the direction of applied force, as well as the workspace position of the active cannula. The displacements and forces at the end effector can be related using a generalized form of Hooke's law, namely,

$$W = K \cdot \xi, \tag{4.36}$$

where W is the wrench applied to the tip of the active cannula, and ξ is the resulting differential displacement of the end-effector frame, and K is the configuration-dependent 6×6 compliance matrix of the active cannula. Determining K analytically is a topic for future research. Until this is accomplished, it will be useful to assess active cannula stiffness experimentally, using prototypes to interact with anatomical models and ex vivo examples of the desired surgical site. Active cannula stiffness can be adjusted by modifying a number of parameters including (1) tube diameters, (2) tube wall thicknesses, (3) tube material (changing the elastic modulus), or (4) using a more favorable part of the active cannula workspace of a better angle of approach. Items 1-3 affect the flexural rigidity of the active cannula. With regard to workspace, using a configuration where active cannula tubes are nearly retracted will stiffen the structure. Also, since active cannula stiffness will be different for different directions of force application, it is also possible to adjust stiffness by changing the angle of approach to the target site. Thus, it will also be important to evaluate the active cannula workspace to assess the feasible directions of approach, and how they are affected by choice of tube precurvature.

- *Explore Workspace Requirements.* The active cannula workspace dimensions can be calculated using the forward kinematics described in this thesis. The Jacobian also permits determination of Active Cannula manipulability via condition number calculation. An example workspace for the prototype in Figure 4.1 is shown in Figure 4.19. When customizing an active cannula for a specific medical objective, one must ensure that the workspace meets the size and dexterity requirements of the application. Fully characterizing active cannula workspace is a topic for future study, as are determining the effects of anatomical constraints. In these studies, the access path must also be taken into account, particularly in scenarios like the lung, where the cannula must traverse a an introductory path like the throat and airways to access the area of interest.

- *Study Bifurcations.* In some medical applications it may be useful to design active cannulas to preclude bifurcation. The analysis of bifurcation in this thesis provides the necessary tools to test whether a given active cannula design (set of tube sizes, properties, and precurvatures) will exhibit bifurcation. In some applications (e.g. when the active cannula is embedded in soft tissue) it will likely be useful to design the cannula to preclude bifurcation, so as not to apply undue force or impulse to tissue. In other applications (e.g. where the cannula has to turn a sharp corner) it may be useful to design a cannula with bifurcation, particularly when the cannula only needs to access the portion of the configuration space that does not trigger this bifurcation.

- *Consider Control Interface.* It is also important to consider the user command

180
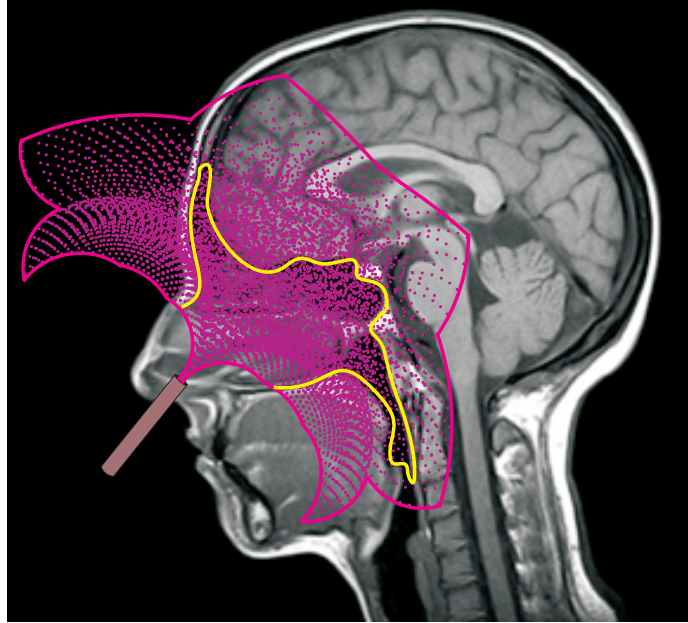
Figure 4.19: The workspace of the prototype active cannula shown in Figure 4.1, shown in comparison to the human head to illustrate relative size. This workspace was generated under the assumption that outer tubes are much stiffer than inner ones. It was made by evenly discretizing the joint space and computing forward kinematics for all joint combinations. Applying the results of this thesis to calculate workspace limits and manipulability in the presence of tube flexibility is a topic for future work, as is analyzing the effect of tissue-imposed geometric constraints on active cannula workspace.

interface for the active cannula, which will differ for various surgical applications. In some scenarios (e.g. deployment in the lung or a body cavity) it may be useful to teleoperatively control the active cannula. In others, (e.g. applications more similar to traditional needle placement) it may be useful to use the active cannula as a CAD-CAM device to automatically servo the tip to the desired location. It will also be important to consider for a given application whether manual or robotic actuation is appropriate. Manual actuation will be most suited for rapid regulatory approval, but a robotic solution will permit coordinated motions of all active cannula joints.

- *Select Guidance Method.* The active cannula will often be used under some form of image guidance. This imaging may be optical, or from a medical imaging source such as Ultrasound, flouroscopy, CT, MRI, etc. Which imaging method to use will depend on the clinical objective and the type of information required. For example, if the active cannula is deployed in soft tissue, Ultrasound guidance may be appropriate, whereas in free space applications (e.g. lung) an imaging method such as fluoroscopy may be most useful.

During the design of a customized active cannula, it will be important to continuously test and iterate with the above considerations in mind to arrive at a suitable or optimal design.

Among the future extensions to the modeling work in this dissertation are the extension of our models to account for arbitrarily preshaped tubes, and incorporating torsional effects in curved sections. Arbitrarily shaped tubes will permit patient-specific active cannulas to be constructed whose shapes are specifically designed based on patient anatomy from preoperative medical images. Note that the models presented here are useful for computing the forward kinematics for piecewise constant precurvature tubes with arbitrarily many pieces. Thus, the models presented in this dissertation can be applied fairly generally, by approximating even general tube curvatures as many short constant curvature sections. However, continuous representations will likely be more accurate and are currently under development. Such continuous representations are also expected to more naturally account for torsion in curved sections of the cannula.

Frictional effects are also present in a system like the active cannula. However, they are not a dominant effect in the experimental prototype used in this chapter. This assertion is based on qualitative observation of the cannula, which does not exhibit significant hysteresis or stick-slip behavior, even without lubrication. Further support is provided by the previously noted observation that experimental and theoretical bifurcation parameters would match if friction accounted for only a 5.4% difference in experimentally observed bifurcation angles. However, it is possible that with active cannulas of different designs (e.g. smaller inter-tube tolerances) frictional effects may become more pronounced. In this case, it will be possible to at least partially account for friction by reducing the torsional spring constant. This is because the effects of reduced torsional stiffness and friction will be similar to one another in that both will contribute to lag in tip angle with respect to base input angle of the tube.

The overall goal of a robot like the active cannula is to become part of a surgical robotic system such as the CAD-CAM or Surgical Assistant systems mentioned in Chapter 1. As mentioned there, the active cannula blurs the distinction between the two, since it can be used as either depending on application requirements. In a CAD-CAM application, the active cannula could be useful for working with an imager to automatically place the tool tip at a desired location in the body through a curved trajectory. It would also provide the degrees of freedom necessary to compensate for unmodeled effects (e.g. external perturbing forces on straight needles) that can lead to tip error with traditional straight tools. In a Surgical Assistant application, an active cannula could be teleoperated as shown in Figure 4.20. The closed-form

Jacobian presented in this dissertation is expected to be useful in both CAD-CAM and Surgical Assistant applications to enable velocities to be commanded at not only the end effector but also various other points along the active cannula backbone.
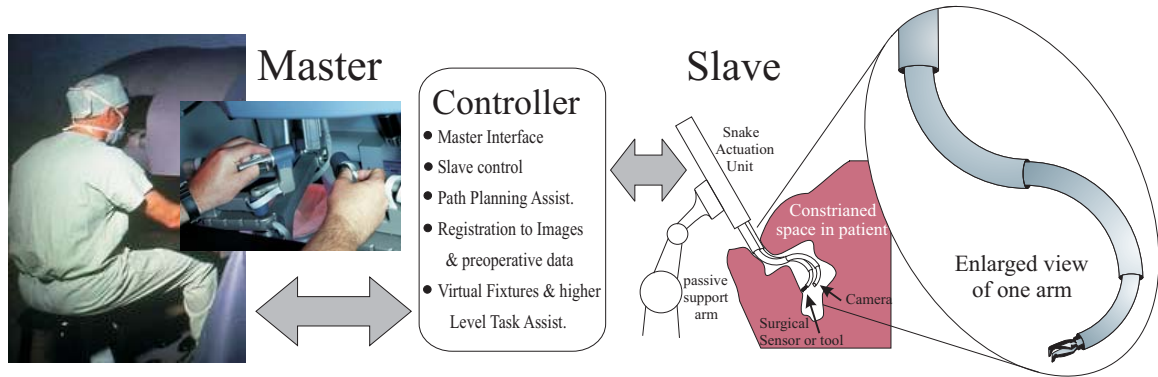
Figure 4.20: Active cannulas have the potential to become new slave robots in a teleoperated Surgical Assistant system. In this capacity, they may enable access to locations that cannot be reached with traditional slave robotic tools which are characterized by larger diameters and straight shafts.

4.9 Conclusion

Miniature flexible robots like active cannulas are a means to bring the benefits of MIS to difficult-to-reach locations in the human body while enhancing patient safety. By building precurvature into the tubes that form the backbone, active cannulas can be small in diameter, have many curved links with little mechanical complexity, and exhibit improved dexterity with miniaturization. They do this using high bandwidth actuation (DC motors) rather than slower heat or electrically activated materials (e.g. shape memory effects).

This chapter provides design, modeling, analysis, and experimental results that are foundational steps toward realizing the potential of active cannulas in medicine

and beyond. Actuation unit considerations, analysis relating tube elastic deformation limits to precurvatures, and tools to characterize and (if desired) prevent bifurcation behavior are among the design contributions presented. Beam mechanics-based models of cannula link shape were derived and generalized into a framework for forward kinematics of multi-link cannulas. This framework is closed form in the torsionless case, and it was shown how torsion can be included through energy minimization. The importance of torsion and the accuracy of the model were evaluated experimentally and parameters were fit through two complementary calibration procedures that agree well with expected parameter ranges calculated from material property tolerances and physical geometry. Experimental results lead to the conclusion that when modeling active cannulas, torsion must be taken into account for accuracy in describing cannula shape, and to make models structurally capable of predicting observed bifurcation behavior.

Despite the inclusion of torsion giving rise to transcendental equations in kinematics that are not closed form (though numerically solvable), differential kinematics can be written in closed form, even with torsion included. The (experimentally validated) assumption that cannula shape locally minimizes stored elastic energy facilitates the closed-form derivation of differential kinematics.

The modeling results pose some interesting challenges for future active cannula designs and applications. One is to solve various robotics problems for active cannulas (e.g. motion planning, inverse kinematics, etc.) in an analytically more complex setting without the aid of closed-form kinematics. Another is to approach the problem from a design perspective and try to create active cannulas that more closely

185

approximate torsionless kinematics, perhaps by constructing them from innovative materials (e.g. with internal windings as in flexible drive shafts).

The results presented in this chapter lay the foundation for active cannula design and control, and have been published in [178, 179] and relevant patents applied for [181]. The work presented here is also currently in preparation for archival journal publication [174, 182]. Building on these studies, it is expected that active cannulas will become a diverse family of both robotic and manual surgical devices. A fully robotic teleoperated active cannula might also incorporate algorithms (currently under development at JHU and elsewhere) on cooperative assistance algorithms embedded in the controller, as well as motion scaling and tremor cancellation. Eventually, a complete system may also assist in path planning, and incorporate information from preoperative medical images into the surgery. Thus, active cannulas appear to be a means of bringing the many advantages normally associated with computer-assisted surgery to currently inaccessible surgical sites.

Chapter 5

Conclusions and Future Work

This dissertation has explored tool manipulation and dexterity enhancements for medical robotic systems. The motivating challenges that drove these endeavors include (1) combining the accuracy and precision of machines with the judgment and skill of clinicians, (2) reducing the trauma of surgery by providing minimally invasive alternatives to open procedures, (3) providing new ways of reaching challenging targets to reduce the number of conditions considered "untreatable" or "inoperable", and (4) making deployment of medical robotic systems more feasible in challenging clinical environments where machines must interact with (often demanding) human operators, and maintain accuracy under uncertain conditions.

5.1 Virtual RCM

Toward these ends, Chapter 2 dealt with algorithms to make robotic tool manipulation systems easier to calibrate and use in the clinical setting, that also facilitate

rapid prototyping of research systems to manipulate new kinds of tools. The main result was the Virtual RCM algorithm which can be carried out using image-based robot pose measurement (or other tracking system), requires little calibration, does not require encoding (allowing encoders to potentially become redundant safety features), can tolerate unknown transformations (e.g. passive positioning arms) in the kinematic chain, and does not require the tool to be coincident with a mechanically enforced RCM. The proof-of-concept prototype system achieved 0.78 mm translation and 1.4° rotational accuracy using a tracker with 2.54 mm RMS error, and did so rapidly (within approximately one second of motion).

Since initial development, the Virtual RCM has been used in conjunction with 3D Ultrasound reconstructed from tracked 2D Ultrasound [20, 23]. It has also been successfully demonstrated phantom studies, proven to be capable of greater accuracy than a surgeon who employed current clinical gold-standard technique, and successfully used in animal studies [18, 19]. Thus, it has demonstrated its usefulness under realistic clinical conditions.

Future goals in Virtual RCM research include replacing the tracker with a CTF scanner or other image-based pose sensing device. It would also be useful to demonstrate experimentally the theoretical features of the algorithm noted in Chapter 2, namely that it can be accomplished with a robot whose wrist axes do not intersect, and that it can be accomplished on an unencoded robot whose Cartesian stages are not orthogonal. In terms of algorithmic enhancements, it will be useful to account for target and treatment volume uncertainties into our algorithm to choose an initial alignment with the best probability of delivering the treatment to the desired target

indicated by the doctor. Segmentation and planning software should also be included in the system to assist the doctor with choosing the target and initial entry trajectory optimally. As active cannulas and steerable needles move toward clinical trials, the Virtual RCM will be useful for positioning them prior to deployment.

5.2 Steerable Needles

Chapter 3 addressed design and modeling of bevel-based needle steering, which can correct for uncertainties like tissue motion, deformation, and inhomogeneity, as well as steer around obstacles. Features of a successful bevel-tip needle steering system were described, including actuation, needle, phantom tissue, and tip tracking considerations. We modeled needle tip trajectory as a nonholonomic system that executes a series of constant curvature arcs described using Lie group theory, and determined by actuator input profiles. To facilitate clinical acceptance and to provide a standard by which to judge the success of model-based controllers, we developed a teleoperation system which allows the radiologist to remain "in the loop" during the procedure.

Since its initial development, the nonholonomic model and experimental testbed described in Chapter 3 has facilitated many further needle steering results. These include closed-loop, model-based control [3, 96, 97], path planning with uncertainty and/or in the presence of obstacles [6, 7, 10, 12, 57, 137], and needle design to enhance curvature [59, 60]. See Section 3.6 for a more detailed description of these recent results.

Future goals in needle steering research include further design and analysis of bevel tip effects, including modeling and experiments evaluating such design possibilities as including a kink a short distance from the tip, or using a tip that is larger than the shaft. Further experiments in ex vivo and live animal tissues will be necessary to determine the accuracy and suitability of existing models, controllers, and planners in biological tissues. Integration of steerable needles with various imaging modalities is an area of future work, including such challenges as sensing the 6-DOF pose of the tip from image data or making use of lower dimensional sensing by using observers. In such studies a key point will be to determine the optimal levels of control vs. rapid replanning.

5.3 Active Cannulas

The active cannulas described in Chapter 4 achieves steerable needle-like trajectories without reliance on reaction forces from the soft-tissue medium. A key insight of active cannulas is that it is possible to achieve greater curvature at smaller size by making use of precurvature rather than initially straight structures, and the design becomes more dexterous with miniaturization. We developed several general design tools for component tube precurvature selection as well as actuation systems, which can be used to eliminate the possibility of cannula self-damage and/or bifurcation, or to achieve other application-specific design goals. Beam mechanics-based models of cannula link shape were derived and generalized into a framework for forward kinematics of multi-link cannulas that is closed form in the torsionless case and tran-

scendental in the torsion-included case. Experiments demonstrated the importance of torsion modeling and the accuracy of the model, verifying that cannula shape locally minimizes stored elastic energy. It was also shown that, despite the inclusion of torsion giving rise to transcendental equations in kinematics, differential kinematics can still be written in closed form.

Active cannulas have great promise in medicine, and have received a great deal of recent interest [65, 145, 178, 179], and a similar design has recently proposed for use as a miniature robot wrist in an eye surgery system [183]. The work presented in this dissertation is the most physically realistic model describing active cannula kinematics, with the most extensive experimental validation, that has been published to date.

Future goals in active cannula research include modeling enhancements that will account for torsion in all parts of the robot and account for variable tube precurvatures, and also possibly the effects of friction (if necessary). Current and new models and calibration algorithms should be verified on cannulas with a large number of links to ensure that they remain as accurate as they are in the 3–link case. From a control standpoint, visual servoing algorithms will be useful to drive active cannulas automatically toward desired goals. The Jacobian derived in this dissertation will facilitate teleoperation, and derivation of the compliance matrix for active cannulas will facilitate using their flexibility combined with shape sensing to sense the forces and torques applied to the cannula by the environment. A workspace characterization will also be useful for design purposes, and path planning algorithms are needed to reach targets within the body. Constructing active cannulas from alternate materials such

as plastics may endow them with further beneficial properties. When considering all these research topics, it will be useful to choose a specific medical application and tailor the design to do a specific clinical task. Considerations and methods for doing so were discussed in Section 4.8. The most promising high-impact first application area (see Section 4.1.1 for others) appears to be the lung, where active cannulas will be able to reach deeper down bronchioles than is possible with current tools that access the lung via the throat. Active cannulas may thus provide a minimally invasive alternative the traumatic procedure of open-chest surgery.

5.4 A Unified Dexterity System

It is possible to combine nearly all of the currently available techniques for needle and needle-like robot dexterity into a single system. Such a system might consist of a robot utilizing the Virtual RCM (or other fulcrum enforcement method) to manipulate a straight stiff introduction tube the diameter of a large-gauge needle. This introduction tube would be the first stage of the device and would enter tissue only a short distance. By robotically controlling the forces and torques applied to the base of the introduction tube, the robot can use the "stiff needle" steering techniques described in Section 3.1.3. Stiff needle steering is achieved by using the needle (introduction tube) to controllably deform tissue, and offer a high degree of steerability near the tissue surface. An active cannula can be deployed from the tip of this introduction tube, providing the capability to traverse not only soft tissue media, but also air or liquid-filled cavities within the body. Finally, a flexible, steerable needle can

be deployed from the active cannula, steering either via bevel forces or other flexible steerable needle tip designs (alternatives were discussed in Section 3.1.3).

Such a "Unified" Dexterity System is expected to combine the most beneficial aspects of nearly all the needle and active cannula dexterity methods that have been developed to date. It would also permit a comparison between their relative merits in a variety of tissue types, clinical scenarios, and depth ranges. It would permit studies to determine exactly how complex a steering system needs to be (e.g. in some circumstances more than one or two steering methods may not produce better clinical outcomes). It would also provide current and future closed-loop controllers with more steerability, enabling them to converge to planned trajectories and targets within anatomically realistic distances. This dissertation has addressed many of the key pieces of such a system, as well as lain the foundation for optimization of dexterity enhancement systems for specific clinical interventions.

Appendix A

Needle Steering

Parameter Identification Data

The data expressed on the following tables are those used in Chapter 3 for fitting the model parameters of the unicycle and bicycle models. All "Single Bend" and "Double Bend" data were fit simultaneously.

Note: All data in the following tables in this appendix are expressed in centimeters.

"Single Bend" Data

Run 1		Run 2		Run 3		Run 4		Run 5		Run 6		Run 7		Run 8	
x	y	x	y	x	y	x	y	x	y	x	y	x	y	x	y
0.0	0.0	0.0	0.0	0.0	0.0	0.0	0.0	0.0	0.0	0.0	0.0	0.0	0.0	0.0	0.0
0.0	-0.3	0.0	-0.3	-0.1	-0.3	0.0	-0.3	-0.1	-0.3	-0.1	-0.3	0.0	-0.3	0.0	-0.3
0.0	-1.3	-0.2	-1.3	-0.2	-1.3	-0.3	-1.3	-0.3	-1.3	-0.2	-1.3	-0.1	-1.3	-0.1	-1.3
-0.1	-2.3	-0.3	-2.3	-0.5	-2.3	-0.5	-2.3	-0.5	-2.3	-0.5	-2.3	-0.2	-2.3	-0.2	-2.3
-0.2	-3.3	-0.4	-3.3	-0.7	-3.3	-0.7	-3.3	-0.8	-3.3	-0.7	-3.3	-0.4	-3.3	-0.5	-3.3
-0.3	-4.3	-0.8	-4.3	-1.0	-4.3	-1.0	-4.3	-1.3	-4.3	-1.1	-4.3	-0.7	-4.3	-0.8	-4.3
-0.5	-5.3	-1.0	-5.3	-1.4	-5.3	-1.3	-5.3	-1.6	-5.3	-1.5	-5.3	-1.1	-5.3	-1.1	-5.3
-0.8	-6.3	-1.5	-6.3	-1.9	-6.3	-1.5	-6.3	-2.0	-6.3	-1.9	-6.3	-1.5	-6.3	-1.5	-6.3
-1.0	-7.3	-1.8	-7.3	-2.4	-7.3	-2.2	-7.3	-2.4	-7.3	-2.4	-7.3	-1.9	-7.3	-1.8	-7.3
-1.4	-8.3	-2.2	-8.3	-3.0	-8.3	-2.6	-8.3	-3.1	-8.3	-3.1	-8.3	-2.3	-8.3	-2.3	-8.3
-1.8	-9.3	-2.7	-9.3	-3.6	-9.3	-3.2	-9.3	-3.8	-9.3	-3.6	-9.3	-2.9	-9.3	-2.8	-9.3
-2.3	-10.3	-3.2	-10.3	-4.3	-10.3	-3.7	-10.3	-4.4	-10.3	-4.4	-10.3	-3.5	-10.3	-3.3	-10.3
-2.8	-11.3	-3.8	-11.3	-5.1	-11.3	-4.3	-11.3	-5.2	-11.3	-5.2	-11.3	-4.2	-11.3	-4.0	-11.3
-3.5	-12.3	-4.4	-12.3	-6.0	-12.3	-5.1	-12.3	-6.2	-12.3	-6.1	-12.3	-5.0	-12.3	-4.5	-12.3
-4.2	-13.3	-5.1	-13.3	-7.0	-13.3	-5.8	-13.3	-7.2	-13.3	-7.2	-13.3	-6.1	-13.3	-5.2	-13.3
-5.0	-14.3	-5.9	-14.3	-8.1	-14.3	-6.7	-14.3	-8.3	-14.3	-8.3	-14.3	-7.3	-14.3	-6.1	-14.3
-6.0	-15.3	-6.8	-15.3	-9.3	-15.3	-7.8	-15.3	-9.8	-15.3	-9.8	-15.3	-8.9	-15.3	-6.9	-15.3
-7.0	-16.3	-8.0	-16.3	-10.9	-16.3	-9.0	-16.3	-11.5	-16.3	-11.6	-16.3	-10.6	-16.3	-7.7	-16.3
-8.3	-17.3	-9.1	-17.3	-12.5	-17.3	-10.4	-17.3	-13.5	-17.3	-13.5	-17.2	-13.0	-17.3	-8.7	-17.3
-9.7	-18.3	-10.6	-18.3	-13.3	-17.7	-12.0	-18.3	-14.2	-17.6			-13.3	-17.4	-10.1	-18.3
-10.8	-19.0	-11.6	-19.1			-12.3	-18.6							-10.7	-19.1

"Double Bend" Data									
Run 1		Run 2		Run 3		Run 4		Run 5	
x	y	x	y	x	y	x	y	x	y
0.0	0.0	0.0	0.0	0.0	0.0	0.0	0.0	0.0	0.0
0.0	-0.3	0.1	-0.3	0.1	-0.3	0.1	-0.3	0.0	-0.3
0.2	-1.3	0.2	-1.3	0.2	-1.3	0.2	-1.3	0.2	-1.3
0.3	-2.3	0.4	-2.3	0.3	-2.3	0.3	-2.3	0.3	-2.3
0.4	-3.3	0.7	-3.3	0.6	-3.3	0.5	-3.3	0.7	-3.3
0.9	-4.3	1.1	-4.3	0.9	-4.3	0.8	-4.3	1.0	-4.3
1.2	-5.3	1.4	-5.3	1.2	-5.3	1.2	-5.3	1.3	-5.3
1.6	-6.3	1.9	-6.3	1.6	-6.3	1.4	-6.3	1.9	-6.3
2.0	-7.3	2.3	-7.3	2.0	-7.3	1.9	-7.3	2.2	-7.3
2.2	-8.3	2.7	-8.3	2.3	-8.3	2.2	-8.3	2.5	-8.3
2.5	-9.3	3.0	-9.3	2.5	-9.3	2.3	-9.3	2.8	-9.3
2.7	-10.3	3.1	-10.3	2.8	-10.3	2.6	-10.3	3.1	-10.3
2.9	-11.3	3.3	-11.3	2.9	-11.3	2.8	-11.3	3.2	-11.3
3.1	-12.3	3.5	-12.3	3.0	-12.3	2.9	-12.3	3.3	-12.3
3.2	-13.3	3.6	-13.3	3.1	-13.3	3.0	-13.3	3.4	-13.3
3.1	-14.3	3.5	-14.3	3.2	-14.3	3.1	-14.3	3.5	-14.3
3.1	-15.3	3.4	-15.3	3.0	-15.3	3.1	-15.3	3.3	-15.3
3.0	-16.3	3.3	-16.3	2.9	-16.3	2.9	-16.3	3.2	-16.3
2.8	-17.3	3.2	-17.3	2.7	-17.3	2.8	-17.3	3.1	-17.3
2.7	-18.3	3.0	-18.3	2.4	-18.3	2.6	-18.3	2.9	-18.3
2.4	-19.3	2.7	-19.3	2.2	-19.3	2.5	-19.3	2.7	-19.3
2.2	-20.3	2.4	-20.3	2.0	-20.3	2.2	-20.3	2.4	-20.3
1.9	-21.3	2.1	-21.3	1.5	-21.3	1.9	-21.3	2.0	-21.3
1.5	-22.3	1.7	-22.3	1.2	-22.3	1.6	-22.3	1.7	-22.3
1.2	-23.3	1.1	-23.3	0.8	-23.3	1.2	-23.3	1.2	-23.3

Appendix B

Active Cannula

Parameter Identification Data

The data expressed on the following tables are those used in Chapter 4 for fitting the model parameters of the torsionless and torsion included active cannula models. "Partial Overlap" and "Full Overlap" data were used together for fitting, as were base, tip of outer tube, and tip of cannula positions, as described in Chapter 4.

Note: All linear data in the following tables in this appendix are expressed in millimeters.

	"Full Overlap" Condition					
	Tip Data			Base Data		
Angle (deg)	X	Y	Z	X	Y	Z
0	-94.4	24.2	701.6	-50.4	-96.0	654.3
20	-94.2	23.1	706.0	-50.6	-96.6	655.9
40	-92.3	22.3	708.7	-50.4	-96.0	654.3
60	-91.6	20.7	712.2	-50.4	-96.0	654.3
80	-89.9	19.5	714.9	-50.4	-96.0	654.3
100	-88.5	18.8	720.5	-50.5	-96.5	655.0
120	-85.9	18.1	723.3	-50.6	-97.0	655.7
140	-83.4	18.9	723.4	-50.4	-96.0	654.3
160	-80.9	17.8	729.1	-50.4	-96.0	654.3
180	-77.4	18.2	728.2	-50.3	-96.5	655.0
200	-74.5	18.2	731.1	-50.4	-96.0	654.3
220	-71.8	18.3	733.1	-50.4	-96.0	654.3
240	-68.2	19.1	731.2	-50.2	-96.0	654.3
260	-64.2	20.8	731.3	-50.2	-96.0	654.3
280	-60.4	23.0	729.5	-50.2	-97.1	653.8
290	-58.2	25.5	728.7	-50.2	-96.0	654.3

Homogeneous Transformation From Camera To Cannula Frame From Point Cloud Registration			
0.0857	-0.346	0.9343	-640.03
0.9963	0.0399	-0.0766	104.89
-0.0108	0.9374	0.3481	-113.19
0	0	0	1

	"Partial Overlap" Condition								
	Tip Data			Outer Tube Tip Data			Base Data		
Angle (deg)	X	Y	Z	X	Y	Z	X	Y	Z
0	-120.5	41.6	713.2	-84.3	31.6	702.2	-50.2	-96.3	654.1
20	-119.5	40.2	717.8	-83.4	31.1	703.0	-50.5	-96.1	652.4
40	-117.0	38.4	725.3	-82.9	29.1	707.6	-50.4	-97.0	655.7
60	-113.9	36.4	729.0	-82.3	28.7	711.1	-50.2	-96.0	654.3
80	-110.9	34.8	739.7	-81.0	28.2	713.5	-50.1	-95.7	652.6
100	-106.2	34.8	741.7	-79.8	27.7	714.6	-50.2	-96.0	654.3
120	-102.7	34.2	746.7	-78.7	27.8	716.8	-50.2	-96.7	654.0
140	-96.4	35.2	748.7	-76.6	27.9	718.2	-50.2	-96.0	654.3
160	-91.8	35.8	753.8	-75.2	27.9	718.2	-50.2	-96.3	654.1
180	-85.5	37.3	755.9	-73.3	27.4	719.5	-50.2	-96.2	653.3
200	-79.1	40.4	754.9	-72.7	27.5	722.1	-50.3	-96.5	655.0

Bibliography

[1] J. J. Abbott. *Virtual Fixtures for Bilateral Telemanipulation*. PhD thesis, Department of Mechanical Engineering, The Johns Hopkins University, August 2005.

[2] J. J. Abbott and A. M. Okamura. Stable forbidden-region virtual fixtures for bilateral telemanipulation. *ASME Journal of Dynamic Systems, Measurement, and Control*, 128:53–64, 2006.

[3] N. Abolhassani, R. V. Patel, and F. Ayazi. Minimization of needle deflection in robot-assisted percutaneous therapy. *International Journal of Medical Robotics and Computer Assisted Surgery*, 3:140–148, 2007.

[4] L. Adhami and E. Coste-Maniere. Optimal planning for minimally invasive surgical robots. *Transactions on Robotics and Automation*, 19(5):854–863, 2003.

[5] M. E. Allaf, D. Stoianovici, S. V. Jackman, and L. R. Kavoussi. A novel system for the confirmation of percutaneous renal access by electrical impedance measurements. *Journal of Endourology*, 12:S82, 1998.

[6] R. Alterovitz, M. Branicky, and K. Goldberg. Constant-curvature motion plan-

ning under uncertainty with applications in image-guided medical needle steering. In *Workshop on the Algorithmic Foundations of Robotics*, July 2006.

[7] R. Alterovitz, K. Goldberg, and A. Okamura. Planning for steerable bevel-tip needle insertion through 2D soft tissue with obstacles. In *IEEE International Conference on Robotics and Automation*, pages 1652–1657, 2005.

[8] R. Alterovitz, K. Goldberg, J. Pouliot, R. Taschereau, and I-C Hsu. Needle insertion and radioactive seed implantation in human tissues: Simulation and sensitivity analysis. In *IEEE International Conference on Robotics and Automation*, pages 1793–1799, 2003.

[9] R. Alterovitz, K. Goldberg, J. Pouliot, R. Taschereau, and I-C Hsu. Sensorless planning for medical needle insertion procedures. In *IEEE/RSJ International Conference on Intelligent Robots and Systems*, pages 3337–3343, 2003.

[10] R. Alterovitz, A. Lim, K. Goldberg, G. S. Chirikjian, and A. M. Okamura. Steering flexible needles under markov motion uncertainty. In *IEEE/RSJ International Conference on Intelligent Robots and Systems*, pages 120–125, August 2005.

[11] R. Alterovitz, J. Pouliot, R. Taschereau, I-C. Hsu, and K. Goldberg. Simulating needle insertion and radioactive seed implantation for prostate brachytherapy. In *Medicine Meets Virtual Reality*, pages 19–25, 2003.

[12] R. Alterovitz, T. Simeon, and K. Goldberg. The stochastic motion roadmap: A

sampling framework for planning with markov motion uncertainty. In *Robotics: Science and Systems*, 2007.

[13] V. Anderson and R. Horn. Tensor arm manipulator design. *ASME Transactions*, 67-DE-57(2):1–12, 1967.

[14] S. Aramaki, S. Kaneko, K. Arai, Y. Takahashi, H. Adachi, and K. Yanagisawa. Tube type micro manipulator using shape memory alloy (sma). In *International Symposium on Micro Machine and Human Science*, pages 115–120, 1995.

[15] K. S. Arun, T. S. Huang, and S. D. Blostein. Least-squares fitting of two 3-D point sets. *IEEE Transactions on Pattern Analysis and Machine Intellegence*, 9(5):698–700, 1987.

[16] M. Betke. *Learning and Vision Algorithms for Robot Navigation*. PhD thesis, Massachusetts Institute of Technology, 1995.

[17] J. C. Blasko, T. Mate, J. E. Sylvester, P. D. Grimm, and W. Cavanagh. Brachytherapy for carcinoma of the prostate: techniques, patient selection, and clinical outcomes. *Seminars in Radiation Oncology*, 12(1):81–94, 2002.

[18] E. M. Boctor. *Enabling Technologies for Ultrasound Imaging in Computer Assisted Intervention*. PhD thesis, Department of Computer Science, The Johns Hopkins University, October 2006.

[19] E. M. Boctor, M. Awad, G. Fichtinger, R. H. Taylor, and M. A. Choti. Development of a robotically-assisted 3D ultrasound system for radiofrequency ablation

of liver tumors. In *6th World Congress of the Hepato-Pancreato-Biliary Association*, 2004. Washington.

[20] E. M. Boctor, M. A. Choti, E.C. Burdette, and R. J. Webster III. 3DUS-guided robotic needle placement: An experimental evaluation. *International Journal of Medical Robotics and Computer Aided Surgery*, 2008. Submitted.

[21] E. M. Boctor, G. Fichtinger, R. H. Taylor, and M. A. Choti. Tracked 3D ultrasound in radio-frequency liver ablation. In *Proceedings of the SPIE*, volume 5035, pages 174–182, 2003.

[22] E. M. Boctor, G. Fischer, M. Choti, G. Fichtinger, and R. Taylor. Dual-armed robotic system for intraoperative ultrasound guided hepatic ablative therapy: A prospective study. In *IEEE International Conference on Robotics and Automation*, pages 2517–2522, 2004.

[23] E. M. Boctor, R. J. Webster III, M. A. Choti, R. H. Taylor, and G. Fichtinger. Robotically assisted ablative treatment guided by freehand 3D ultrasound. In *Computer Assisted Radiology and Surgery*, pages 503–508, 2004.

[24] E. M. Boctor, R. J. Webster III, H. Mathieu, A. M. Okamura, and G. Fichtinger. Virtual remote center of motion control for needle placement robots. In *Medical Image Computing and Computer-Assisted Interventions*, volume 2878 of *Lecture Notes in Computer Science*, pages 157–164. Springer-Verlag, 2003.

[25] E. M. Boctor, R. J. Webster III, H. Mathieu, A. M. Okamura, and G. Fichtinger.

Virtual remote center of motion control for needle-placement robots. *Journal of Computer Assisted Surgery*, 9(5):175–183, 2004.

[26] R. S. Boris, S. A. Kaul, R. C. Sarle, and H. J. Stricker. Radical prostatectomy: a single surgeon comparison of retropubic, perineal, and robotic approaches. *The Canadian Journal of Urology*, 14(3):3566–3570, 2007.

[27] J.-Y. Bouguet. Camera calibration toolbox for matlab. `http://www.vision.caltech.edu/bouguetj/calib_doc/index.html`. Last acessed May 2007.

[28] P. N. Brett, A. J. Harrison, and T. A. Thomas. Schemes for the identification of tissue types and boundaries at the tool point for surgical needles. *IEEE Transactions on Information Technology in Biomedicine*, 4(1):30–36, March 2000.

[29] P. N. Brett, T. J. Parker, A. J. Harrison, T. A. Thomas, and A. Carr. Simulation of resistance forces acting on surgical needles. *Proceedings of the Institution of Mechanical Engineers*, 211(4):335–347, 1997. Part H: Journal of Engineering in Medicine.

[30] I. Brouwer, J. Ustin, L. Bentley, A. Sherman, N. Dhruv, and F. Tendick. Measuring in vivo animal soft tissue properties for haptic modeling in surgical simulation. In *Medicine Meets Virtual Reality*, pages 69–74, 2001.

[31] J. W. Cannon, J. A. Stoll, S. D. Sehla, P. E. Dupont, R. D. Howe, and D. F. Torchina. Port placement planning in robot-assisted coronary artery bypass. *IEEE Transactions on Robotics and Automation*, 19(5):912–917, 2003.

[32] M. C. Cavusoglu, I. Villanueva, and F. Tendick. Workspace analysis of robotic manipulators for a teleoperated suturing task. *IEEE/RSJ International Conference on Intelligent Robots and Systems*, 4:2234–2239, 2001.

[33] G. S. Chirikjian. *Theory and Applications of Hyper-Redundant Robotic Manipulators*. PhD thesis, Department of Applied Mechanics, California Institute of Technology, 1992.

[34] G. S. Chirikjian. A general numerical method for hyper-redundant manipulator inverse kinematics. *IEEE International Conference on Robotics and Automation*, pages 107–112, 1993.

[35] G. S. Chirikjian. Hyper-redundant manipulator dynamics: A continuum approximation. *Advanced Robotics*, 9(3):217–243, 1995.

[36] G. S. Chirikjian. Kinematic synthesis of mechanisms and robotic manipulators with binary actuators. *Journal of Mechanical Design*, 117:573–580, 1995.

[37] G. S. Chirikjian and J. W. Burdick. An obstacle avoidance algorithm for hyper-redundant manipulators. In *IEEE International Conference on Robotics and Automation*, pages 625–631, 1990.

[38] G. S. Chirikjian and J. W. Burdick. Design and experiments with a 30 DOF robot. In *IEEE International Conference on Robotics and Automation*, pages 113–119, 1993.

[39] G. S. Chirikjian and J. W. Burdick. A modal approach to hyper-redundant

manipulator kinematics. *IEEE Transactions on Robotics and Automation*, 10(3):343–353, June 1994.

[40] G. S. Chirikjian and J. W. Burdick. Kinematically optimal hyper-redundant manipulator configurations. *IEEE Transactions on Robotics and Automation*, 11(6):794–806, December 1995.

[41] G. S. Chirikjian and J.W. Burdick. Parallel formulation of the inverse kinematics of modular hyper-redundant manipulators. *IEEE International Conference on Robotics and Automation*, pages 708–713, 1991.

[42] R. Cieslak and A. Morecki. Elephant trunk type elastic manipulator-a tool for bulk and liquid materials transportation. *Robotica*, 17:11–16, 1999.

[43] M. R. Cooperberg, D. P. Lubeck, M. V. Meng, S. S. Mehta, and P. R. Carroll. The changing face of low-risk prostate cancer: trends in clinical presentation and primary management. *Journal of Clinical Oncology*, 22(11):2141–9, 2004.

[44] J. J. Craig. *Introduction to Robotics: Mechanics and Control*. Addison Wesley, Reading, MA, 3rd edition, 1992.

[45] P. Dario, M. C. Carrozza, M. Marcacci, S. D'Attanasio, B. Magnami, and G. Megali O. Tonet. A novel mechatronic tool for computer-assisted arthroscopy. *IEEE Transactions on Information Technology in Biomedicine*, 4(1):15–29, 2000.

[46] P. Dario, C. Paggetti, N. Troisfontaine, E. Papa, T. Ciucci, M. C. Carrozza, and M. Marcacci. A miniature steerable end-effector for application in an integrated

system for computer-assisted arthroscopy. In *IEEE International Conference on Robotics and Automation*, pages 1573–1579, 1997.

[47] V. Datta, M. Mandalia, S. Mackay, A. Chang, N. Cheshire, and A. Darzi. Relationship between skill and outcome in the laboratory-based model. *Surgery*, 131(3):318–323, 2002.

[48] W. Daum. A deflectable needle assembly, 2003. Patent 6,572,593.

[49] B. L. Davies, R. D. Hibberd, W. S. Ng, A. G. Timoney, and J. E. Wickham. The development of a surgeon robot for prostatectomies. *Proc Inst Mech Eng.*, 205(1):35–38, 1991.

[50] A. Degani, H. Choset, A. Wolf, T. Ota, and M. A. Zenati. Percutaneous intrapericardial interventions using a highly articulated robotic probe. In *IEEE / RAS-EMBS International Conference on Biomedical Robotics and Biomechatronics*, pages 7 – 12, February 2006.

[51] J.-G. S. Demers, J. M. A. Boelen, and I. P. W. Sinclair. Freedom 6s force feedback hand controller. In *SPRO '98 IFAC Workshop on Space Robotics*, Montreal, Canada, October 19-22 1998.

[52] S. P. DiMaio and S. E. Salcudean. Needle insertion modeling and simulation. *IEEE Transactions on Robotics and Automation*, 19(5):864–875, 2003.

[53] S. P. DiMaio and S. E. Salcudean. Needle steering and model-based trajectory planning. *Medical Image Computing and Computer-Assisted Intervention*, pages 33–40, 2003.

[54] S. P. DiMaio and S. E. Salcudean. Interactive simulation of needle insertion models. *IEEE Transactions on Biomedical Engineering*, 52(7):1167–1179, July 2005.

[55] B. R. Donald. A search algorithm for motion planning with six degrees of freedom. *Artificial Intelligence*, 31(3):295–353, March 1987.

[56] Thomas W. Duerig, Alan R. Pelton, and Dieter Stockel. Superelastic nitinol for medical devices. *Medical Plastics and Biomaterials Magazine*, pages 30–43, March 1997.

[57] V. Duindam, K. Goldberg, S. Sastry, and R. Alterovitz. Geometric motion planning for bevel-tip flexible needles in 3d environments with obstacles. In *IEEE International Conference on Robotics and Automation*, 2008. (submitted).

[58] I. Ebeert-Uphoff and G. Chirikjian. Inverse kinematics of discretely actuated hyper-redundant manipulators using workspace densities. *IEEE International Conference on Robotics and Automation*, pages 139–145, 1996.

[59] J. A. Engh, G. Podnar, S. Khoo, and C. N. Riviere. Flexible needle steering system for percutaneous access to deep zones of the brain. *IEEE 32nd Annual Northeast Bioengineering Conference*, pages 103 – 104, 2006.

[60] J. A. Engh, G. Podnar, D. Kondziolka, and C. N. Riviere. Toward effective needle steering in brain tissue. *28th Annual International Conference of the IEEE Engineering in Medicine and Biology Society*, pages 559–562, 2006.

[61] A. Faraz and S. Payandeh. Synthesis and workspace study of endoscopic extenders with flexible stem, research report, experimental robotics laboratory. Simon Fraser University, Canada, http://www.ensc.sfu.ca/research/erl/med/. Last accessed 10/4/2005.

[62] Gabor Fichtinger, Theodore L. DeWeese, Alexandru Patriciu, Attila Tanacs, Dumitru Mazilu, James H. Anderson, Ken Masamune, Russell H. Taylor, and Dan Stoianovici. System for robotically assisted prostate biopsy and therapy with intraoperative CT guidance. *Academic Radiology*, 9(1):60–74, 2002.

[63] D. J. Fleming, S. McGuff, and C. B. Simpson. Comparison of microflap healing outcomes with traditional and microsuturing techniques: initial results in a canine model. *Ann Otol Rhinol Laryngol*, 110(8):707–712, 2001.

[64] Y. C. Fung. *Biomechanics: Mechanical Properties of Living Tissues, 2nd Edition.* New York: Springer-Verlag, 1993.

[65] J. Furusho, T. Katsuragi, T. Kikuchi, T. Suzuki, H. Tanaka, Y. Chiba, and H. Horio. Curved multi-tube systems for fetal blood sampling and treatments of organs like brain and breast. *Journal of Computer Assisted Radiology and Surgery*, pages 223–226, 2006.

[66] S. F. Gibson and B. Mirtich. A survey of deformable modeling in computer graphics. Technical report, MERL, TR-97-19, 1997.

[67] R. B. Gillespie, J. E. Colgate, and M. A. Peshkin. A general framework for

cobot control. *IEEE Transactions on Robotics and Automation*, 17(4):391–401, 2001.

[68] D. Glozman and M. Shoham. Flexible needle steering and optimal trajectory planning for percutaneous therapies. In C. Barillot, D.R. Haynor, and P. Hellier, editors, *Medical Image Computing and Computer Assisted Intervention*, volume 3217 of *Lecture Notes in Computer Science*, pages 137–144. Springer, 2004.

[69] D. Glozman and M. Shoham. Image-guided robotic flexible needle steering. *IEEE Transactions on Robotics*, 23(3):459–467, June 2007.

[70] P. Gorman, T. Krummel, R. Webster, M. Smith, and D. Hutchens. A prototype haptic lumbar puncture simulator. *Proceedings of Medicine Meets Virtual Reality*, pages 106–109, 2000.

[71] I. A. Gravagne. *Design, Analysis and Experimentation: the Fundamentals of Continuum Robotic Manipulators*. PhD thesis, Clemson University, 2002.

[72] I. A. Gravagne, C.D. Rahn, and I. D. Walker. Large-deflection dynamics and control for planar continuum robots. *IEEE/ASME Transactions on Mechatronics*, 8(2):299–307, June 2003.

[73] I. A. Gravagne and I. D. Walker. Kinematic transformations for remotely-actuated planar continuum robots. *IEEE International Conference on Robotics and Automation*, pages 19–26, 2000.

[74] I. A. Gravagne and I. D. Walker. On the structure of minimum effort solutions

with application to kinematic redundancy resolution. *IEEE Transactions on Robotics and Automation*, 19(6):855–863, December 2000.

[75] I. A. Gravagne and I. D. Walker. Manipulability, force, and compliance analysis for planar continuum robots. *IEEE Transactions on Robotics and Automation*, 18(3):263–273, June 2002.

[76] S. Guo, T. Fukuda, T. Nakamura, F. Arai, K. Oguro, and M. Negoro. Micro active guide wire catheter system - characteristic evaluation, electrical model and operability evaluation of micro active catheter. *IEEE International Conference on Robotics and Automation*, pages 2226–2231, 1996.

[77] G. S. Guthart and J. K. Salisbury. The Intuitive^{TM} telesurgery system: Overview and application. *IEEE International Conference on Robotics and Automation*, pages 618–621, 2000.

[78] Y. Haga, Y. Tanahashi, and M. Esashi. Small diameter active catheters using shape memory alloy. *Proceedings of IEEE Micro Elector Mechanical Systems*, pages 419–424, 1998.

[79] M. W. Hannan. *Theory and Experiments with an Elephants Trunk Robotic Manipulator*. PhD thesis, Department of Electrical and Computer Engineering, Clemson University, 2002.

[80] M. W. Hannan and I. D. Walker. Kinematics and the implementation of an elephant's trunk manipulator and other continuum style robots. *Journal of Robotic Systems*, 20(2):45–63, 2003.

[81] M. W. Hannan and I. D. Walker. Real-time shape estimation for continuum robots. *Robotica*, 23(5):645–651, 2005.

[82] S. J. Harris, F. Arambula-Cosio, Q Mei, R. D. Hibberd, B. L. Davies, J. E. Wickham, M. S. Nathan, and B. Kundu. The probot–an active robot for prostate resection. *Proceedings of the Institution of Mechanical Engineers*, 211(4):317–325, 1997.

[83] M. Hashimoto, T. Tabata, and T. Yuki. Development of electrically heated sma active forceps for laparoscopic surgery. *IEEE International Conference on Robotics and Automation*, pages 2372 – 2377, 1999.

[84] K. Hayashi, H. Abe, and M. Sato. *Data Book on Mechanical Properties of Living Cells, Tissues, and Organs*. New York: Springer, 1996.

[85] H. M. Hegazy, R. L. Carrau, C. H. Snyderman, A. Kassam, and J. Zweig. Transnasal endoscopic repair of cerebrospinal fluid rhinorrhea: A meta-analysis. *The Laryngoscope*, 110:1166–1172, 2000.

[86] L. Hiemenz, J. S. McDonald, D. Stredney, and D. Sessanna. A physiologically valid simulator for training residents to perform an epidural block. *Proceedings of the IEEE Biomedical Engineering Conference*, pages 170–173, 1996.

[87] S. Hirose. *Biologically Inspired Robots, Snake-Like Locomotors and Manipulators*. Oxford University Press, 1993.

[88] S. Hirose and S. Ma. Coupled tendon-driven multijoint manipulator. *IEEE International Conference on Robotics and Automation*, pages 1268–1275, 1991.

[89] S. Hutchinson, G. D. Hager, and P. Corke. A tutorial on visual servo control. *IEEE Transactions on Robotics and Automation*, 12(5):651–670, 1996.

[90] K. Ikuta, M. Tsukamoto, and S. Hirose. Shape memory alloy servo actuator system with electric resistance feedback and application for active endoscope. *IEEE International Conference on Robotics and Automation*, pages 427–430, 1988.

[91] G. Immega and K. Antonelli. The ksi tentacle manipulator. *IEEE International Conference on Robotics and Automation*, pages 3149–3154, 1995.

[92] A. Jemal, R. C. Tiwari, T. Murray, A. Ghafoor, A. Samuels, E. Ward, E. J. Feuer, and M. J. Thun. Cancer statistics, 2004. *CA Cancer J Clin*, 54(8), 2004.

[93] B. A. Jones, W. McMahan, and I. D. Walker. Practical kinematics for real-time implimentation of continuum robots. *IEEE International Conference on Robotics and Automation*, pages 1840–1847, 2006.

[94] B. A. Jones and I. D. Walker. Kinematics for multisection continuum robots. *IEEE Transactions on Robotics*, 22(1):43–55, Feb. 2006.

[95] B. A. Jones and I. D. Walker. Practical kinematics for real-time implementation of continuum robots. *IEEE Transactions on Robotics*, 22(6):1087–1099, Dec. 2006.

[96] V. Kallem, D. E. Chang, and N. J. Cowan. Task-induced symmetry and reduction in kinematic systems with application to needle steering. In *EEE/RSJ Intelligent Robots and Systems*, pages 3302–3308, 2007.

[97] V. Kallem and N. J. Cowan. Image-guided control of flexible bevel-tip needles. *IEEE International Conference on Robotics and Automation*, pages 3015–3020, 2007.

[98] M. Kaneko and T. Kawahara. Co-axis type non-contact impedance sensor. *IEEE International Conference on Robotics and Automation*, 1:709–714, 2004.

[99] A. Kapoor. *Motion Constrained Control of Robots for Dexterous Surgical Tasks*. PhD thesis, Department of Computer Science, The Johns Hopkins University, September 2007.

[100] A. Kapoor, N. Simaan, and P. Kazanzides. A system for speed and torque control of DC motors with application to small snake robots. *IEEE Conference on Mechatronics and Robotics*, 2004.

[101] A. Kapoor, N. Simaan, and R. Taylor. Suturing in confined spaces: Constrained motion control of a hybrid 8-DOF robot. *International Conference on Advanced Robotics*, pages 452–459, 2005.

[102] A. B. Kassam, C. Snyderman, P. Gardner, R. Carrau, and R. Spiro. The expanded endonasal approach: A fully endoscopic transnasal approach and resection of the odontoid process: Technical case report. *Operative Neurosurgery*, 57, 2005.

[103] I. Kassim, L. Phee, W. S. Ng, F. Gong, P. Dario, and C. A. Mosse. Locomotion techniques for robotic colonoscopy. *IEEE Engineering in Medicine and Biology Magazine*, 25(3):49–56, May/June 2006.

[104] H. Kataoka, T. Washio, M. Audette, and K. Mizuhara. A model for relations between needle deflection, force, and thickness on penetration. In W. Niessen and M. Viergever, editors, *Medical Image Computing and Computer Assisted Intervention*, volume 2208 of *Lecture Notes in Computer Science*, pages 966–974. Springer-Verlag, 2001.

[105] H. Kataoka, T. Washio, K. Chinzei, K. Mizuhara, C. Simone, and A. Okamura. Measurement of tip and friction force acting on a needle during penetration. In T. Dohi and R. Kikinis, editors, *Medical Image Computing and Computer Assisted Intervention*, volume 2488 of *Lecture Notes in Computer Science*, pages 216–223. Springer, 2002.

[106] A. E. Kerdok and R. D. Howe. A technique for measuring local internal mechanical properties of perfused solid organs. *ASME Summer Bioengineering Conference*, pages 945–946, 2003.

[107] O. Khatib. A unified approach for motion and force control of robot manipulators: The operational space formulation. *IEEE Journal of Robotics and Automation*, 3:43–53, 1987.

[108] R. Kikinis et al. 3D slicer: Medical visualization and processing environment for research. http://www.slicer.org/. MIT Artificial Intelligence Lab and the Surgical Planning Lab at Brigham & Women's Hospital. Accessed 16 January 2003.

[109] J. S. Kim. *A Group Theoretic and Statistical Mechanical Treatment of Chainlike*

Structures. PhD thesis, Department of Mechanical Engineering, The Johns Hopkins University, 2006.

[110] J. S. Kim and G. S. Chirikjian. Conformational analysis of stiff chiral polymers with end-constraints. *Molecular Simulation*, 32(14):1139–1154, December 2006.

[111] T. A. Krouskop, T. M. Wheeler, F. Kallel, B. S. Garria, and T. Hall. Elastic moduli of breast and prostate tissues under compression. *Ultrasonic Imaging*, 20(4):260–274, 1998.

[112] Y. S. Kwoh, J. Hou, E. A. Jonckheere, and S. Hayati. A robot with improved absolute positioning accuracy for CT guided stereotactic brain surgery. *IEEE Transactions on Biomedical Engineering*, 35(2):153–160, 1998.

[113] B. R. Lee, W. W. Roberts, D. G. Smith, H. W. Ko, J. I. Epstein, K. Lecksell, and A. W. Partin. Bioimpedance: Novel use of a minimally invasive technique for cancer localization in the intact prostate. *The Prostate*, 39(3):213–218, 1999.

[114] S. Lee, G. Fichtinger, and G. S. Chirikjian. Novel algorithms for robust registration of fiducials in ct and mri. *Journal of Medical Physics*, 29(8):1881–1891, 2002.

[115] C. Li and C. Rahn. Design of continuous backbone, cable-driven robots. *ASME Journal of Mechanical Design*, 124(2):265–271, 2002.

[116] Q. H. Li, L. Zamorano, A. Pandya, R. Perez, J. Gong, and F. Diaz. The application accuracy of the neuromate robot-a quantitative comparison with frame-

less and frame-based surgical localization systems. *Computer Aided Surgery*, 7(2):90–98, 2002.

[117] G. Lim, K. Park, M. Sugihara, K. Minami, and M. Esashi. Future of active catheters. *Sensors and Actuators*, 56(1-2):113–121, 1996.

[118] M. Loser. A new robotic system for visually controlled percutaneous interventions under X-ray or CT-fluoroscopy. Master's thesis, The Albert-Ludwig-University, Freiburg, Germany, September 2002.

[119] M. Mahvash and V. Hayward. Haptic rendering of cutting: A fracture mechanics approach. *Haptics-e: The Electronic Journal of Haptics Research (www.haptics-e.org)*, 2(3), 2001.

[120] S. A. Mayer. Ultra-early hemostatic therapy for intracerebral hemorrhage. *Stroke*, 34(1):224–229, 2003.

[121] J. Memisevic, R. J. Webster III, and A. M. Okamura. Design of a needle steering robot for minimally invasive surgery. *NSF REU poster at the Biomedical Engineering Society Fall Meeting*, October 13-16 2004. Philadelphia, PA.

[122] S. Mulier, Y. Ni, Y. Miao, A. Rosiere, A. Khoury, G. Marchal, and L. Michel. Size and geometry of hepatic radiofrequency lesions. *European Journal of Surgical Oncology*, 29(10):867–78, 2003.

[123] Richard M. Murray, Zexiang Li, and S. Shankar Sastry. *A Mathematical Introduction to Robotic Manipulation*. CRC Press, Boca Raton, FL, 1994.

[124] V. Mut, J. Postigo, E. Slawinski, and B. Kuchen. Bilateral teleoperation of mobile robots. *Robotica*, 20:213–221, 2002.

[125] E. K. Nakakura and M. A. Choti. Management of hepatocellular carcinoma. *Oncology*, 14(7):1085–1098, 2000.

[126] Y. Nakamura, A. Matsui, T. Saito, and K. Yoshimoto. Shape-memory-alloy active forceps for laparoscopic surgery. *IEEE International Conference on Robotics and Automation*, pages 2320–2327, 1995.

[127] H. W. Nienhuys and A.F. van der Stappen. A surgery simulation supporting cuts and finite element deformation. In W. J. Niessen and M. A. Viergever, editors, *Medical Image Computing and Computer-Assisted Intervention*, pages 145–152. Springer-Verlag, 2001.

[128] H. W. Nienhuys and A.F. van der Stappen. A computational technique for interactive needle insertions in 3D nonlinear material. *IEEE International Conference on Robotics and Automation*, pages 2061–2067, 2004.

[129] W. L. Nowinski and T. Poston. Curved surgical instruments and method of mapping a curved path for stereotactic surgery. US Patent 6,701,173, March 2 2004.

[130] R. Ohta. Results of R&D on catheter-type micromachine. *International Symposium on Micromechatronics and Human Science*, pages 5–12, 2001.

[131] A. M. Okamura. Methods for haptic feedback in teleoperated robot-assisted surgery. *Industrial Robot*, 31(6):499–508, 2004.

[132] S. Okazawa, R. Ebrahimi, J. Chuang, S. E. Salcudean, and R. Rohling. Hand-held steerable needle device. *IEEE/ASME Transactions on Mechatronics*, 10(3):285 – 296, 2005.

[133] M. D. O'Leary, C. Simone, T. Washio, K. Yoshinaka, and A. M. Okamura. Robotic needle insertion: Effects of friction and needle geometry. *IEEE International Conference on Robotics and Automation*, pages 1774–1780, 2003.

[134] K. Osuka and H. Kitajima. Development of mobile inspection robot for rescue activities: MIORA. *IEEE/RSJ International Conference on Intelligent Robots and Systems*, pages 3373–3377, 2003.

[135] E. Paljug, T. Ohm, and S. Hayati. The JPL serpentine robot: a 12-DOF system for inspection. *IEEE International Conference on Robotics and Automation*, pages 3143–3148, 1995.

[136] J. Park and W.-K. Chung. Geometric integration on euclidean group with application to articulated multibody systems. *IEEE Transactions on Robotics*, 21(5):850–863, 2005.

[137] W. Park, J. S. Kim, Y. Zhou, N. J. Cowan, A. M. Okamura, and G. S. Chirikjian. Diffusion-based motion planning for a nonholonomic flexible needle model. In *IEEE International Conference on Robotics and Automation*, pages 4611–4616, Barcelona, Spain, April 2005.

[138] J. Peirs, D. Reynaerts, H. Van Brussel, G. De Gersem, and H. T. Tang. Design

of an advanced tool guiding system for robotic surgery. *IEEE International Conference on Robotics and Automation*, pages 2651–2656, 2003.

[139] L. Phee, D. Accoto, A. Menciassi, C. Stefanini, M. C. Carrozza, and P. Dario. Analysis and development of locomotion devices for the gastrointestinal tract. *IEEE Transactions on Biomedical Engineering*, 49(6):613–616, 2002.

[140] S. J. Phee, W. S. Ng, I. M. Chen, F. Seow-Choen, and B. L. Davies. Locomotion and steering aspects in automation of colonoscopy part one: A literature review. *IEEE Engineering in Medicine and Biology Magazine*, 16(6):85–96, November/Detember 1997.

[141] G. Robinson and J. B. C. Davies. Continuum robots – a state of the art. *IEEE International Conference on Robotics and Automation*, pages 2849–2854, 1999.

[142] R. J. Rohrich, J. K. Krueger, W. P. Adams, and B. F. Marple. Rationale for submucous resection of hypertrophied inferior turbinates in rhinoplasty: An evolution. *Plastic and Reconstructive Surgery*, 108(2):536–544, 2001.

[143] J. Romano, R. J. Webster III, and A. M. Okamura. Teleoperation of steerable needles. *IEEE International Conference on Robotics and Automation*, pages 934–939, 2007.

[144] A. Rovetta. Tests on reliability of a prostate biopsy telerobotic system. *Stud Health Technol Inform.*, 62:302–307, 1999.

[145] P. Sears and P. E. Dupont. A steerable needle technology using curved con-

centric tubes. *IEEE/RSJ International Conference on Intelligent Robots and Systems (IROS)*, pages 2850–2856, October 9-15 2006. Beijing, China.

[146] P. Sears and P. E. Dupont. Inverse kinematics of concentric tube steerable needles. *IEEE International Conference on Robotics and Automation*, pages 1887–1892, 2007.

[147] M. Shoham, R. Taylor, G. Chirikjian, A. Olivi, and F. Frassica. Flexible microtools for minimally invasive surgery. Research Proposal to JHU/Technion Program, Johns Hopkins University, Baltimore, MD, March 2002.

[148] N. Simaan. Snake-like units using flexible backbones and actuation redundancy for enhanced minaturization. *International Conference on Robotics and Automation*, pages 3023–3028, 2005.

[149] N. Simaan, R. Taylor, and P. Flint. A dexterous system for laryngeal surgery. *IEEE International Conference on Robotics and Automation*, pages 351–357, 2004.

[150] N. Simaan, R. H. Taylor, and P. Flint. High dexterity snake-like robotic slaves for minimally invasive telesurgery of the upper airway. *MICCAI 2004 - the 7th International Conference on Medical Image Computing and Computer-Assisted Intervention*, pages 17–24, 2004.

[151] C. Snyderman. Co-director, Center for Minimally Invasive and Cranial Base Neurosurgery, University of Pittsburgh Medical Center, 2004. Personal Communication.

[152] S. B. Solomon, A. Patriciu, M. E. Bohlman, L. R. Kavoussi, and D. Stoianovici. Robotically driven interventions: A method of using CT fluoroscopy without radiation exposure to the physician. *Radiology*, 225(1):277–282, 2002.

[153] D. Stoianovici. Urobotics – urology robotics at Johns Hopkins. *Journal of Computer Aided Surgery*, 6(6):360–369, 2001.

[154] D. Stoianovici, J. A. Cadeddu, R. D. Demaree, S. A. Basile, R. H. Taylor, L. L. Whitcomb, W. N. Sharpe, and L. R. Kavoussi. A novel mechanical transmission applied to percutaneous renal access. *American Society of Mechanical Engineers Dynamic Systems and Control*, DSC 61:401–406, 1997.

[155] D. Stoianovici, R. J. Webster III, and L. Kavoussi. Surgical robotic applications in minimally invasive uro-oncology surgery. In R. Moore and J. Bishoff, editors, *Minimally Invasive Uro-Oncologic Surgery*, pages 353–363. Taylor and Francis, London and New York, 2005. ISBN 1-84184-566-3.

[156] D. Stoianovici, L. L. Whitcomb, J. H. Anderson, R. H. Taylor, and L. R. Kavoussi. A modular surgical robotic system for image guided percutaneous procedures. *Medical Image Computing and Computer Assisted Intervention*, pages 404–410, 1998.

[157] L. M. Su, D. Stoianovici, T. W. Jarrett, A. Patriciu, W. W. Roberts, J. A. Cadeddu, S. Ramakumar, S. B. Solomon, and L. R. Kavoussi. Robotic percutaneous access to the kidney: Comparison with standard manual access. *J Endourol.*, 16(7):471–475, 2002.

[158] J. Suthakorn and G. S. Chirikjian. A new inverse kinematics algorithm for binary manipulators with many actuators. *Advanced Robotics*, 15(2):225–244, 2001.

[159] K. Suzumori, S. Iikura, and H. Tanaka. Development of flexible microactuator and its applications to robotic mechanisms. *IEEE International Conference on Robotics and Automation*, pages 1622–1627, 1991.

[160] K. Suzumori, S. Wakimoto, and M. Takata. A miniature inspection robot negotiating pipes of widely varying diameter. *IEEE International Conference on Robotics and Automation*, pages 2735–2740, 2003.

[161] M. Takahashi, I. Hayashi, N. Iwatsuki, K. Suzumori, and N. Ohki. The development of an in-pipe microrobot applying the motion of an earthworm. *International Symposium on Micro Machine and Human Science*, pages 35–40, 1994.

[162] R. Taylor, J. Funda, B. Eldridge, S. Gomory, K. Gurben, D. LaRose, M. Talamini, L. Kavoussi, and J. Anderson. A telerobotic assistant for laparoscopic surgery. *IEEE Engineering in Medicine and Biology Magazine*, 14(3):279–288, 1995.

[163] R. H. Taylor. A perspective on medical robotics. *Proceedings of the IEEE*, 94(9):1652–1664, 2006.

[164] R. H. Taylor, J. Funda, B. Eldridge, S. Gomory, K. Gruben, D. LaRose, M. Talamini, L. A. Kavoussi, and J. H. Anderson. A telerobotic assistant for laparo-

scopic surgery. *IEEE Engineering in Medicine and Biology Magazine*, 14(3):279 – 288, May-June 1995.

[165] R. H. Taylor, R. Kumar, and et al. Library of modular robot control. http://www.cisst.org/resources/software/mrc/. Engineering Research Center Computer Integrated Surgical Systems and Technology (ERC-CISST). Accessed 16 January 2003.

[166] R. H. Taylor and D. Stoianovici. Medical robotics in computer-integrated surgery. *IEEE Transactions on Robotics and Automation*, 19(5):765–781, 2003.

[167] M. Terayama, J. Furusho, and M. Monden. Curved multi-tube device for path-error correction in a needle-insertion system. *International Journal of Medical Robotics and Computer Assisted Surgery*, 3(2):125–134, 2007.

[168] S. C. Ulmer. Hepatocellular carcinoma: a concise guide to its status and management. *Postgrad Med*, 107(5):117–24, 2000.

[169] T. R. K. Varma, P. R. Eldridge, A. Forster, S. Fox, N. Fletcher, M. Steiger, P. Littlechild, P. Byrne, A. Sinnott, K. Tyler, and S. Flintham. Use of the neuromate stereotactic robot in a frameless mode for movement disorder surgery. *Stereotact Funct Neurosurg.*, 80(1–4):132–135, 2003.

[170] T. Vo-Dinh and B. Cullum. Biosensors and biochips: advances in biological and medical diagnostics. *Fresenius' Journal of Analytical Chemistry*, 366(6-7):540–551, 2000.

[171] Y. Wakahara, K. Asano, and T. Tsuchihashi. A computer aided manipulation system for a multijoint inspection robot. *Transactions of the American Nuclear Society*, 47:455–456, 1984.

[172] I. D. Walker and M. W. Hannan. A novel 'elephant's trunk' robot. *IEEE/ASME International Conference on Advanced Intelligent Mechatronics*, pages 410–415, 1999.

[173] K. Wallner, J. C. Blasko, and M. Dattoli. *Prostate Brachytherapy Made Complicated*. SmartMedicine Press, Seattle, Washington, second edition, 2001.

[174] R. J. Webster III and N. J. Cowan. Design and mechanics of active cannulas. *IEEE Transactions on Robotics*, 2008. In Preparation.

[175] R. J. Webster III, N. J. Cowan, G. S. Chirikjian, and A. M. Okamura. Nonholonomic modeling of needle steering. In *9th International Symposium on Experimental Robotics*, pages 35–44, Singapore, June 2004.

[176] R. J. Webster III, J. S. Kim, N. J. Cowan, G. S. Chirikjian, and A. M. Okamura. Nonholonomic modeling of needle steering. *International Journal of Robotics Research*, 25(5/6):509–526, May/June 2006.

[177] R. J. Webster III, J. Memisevic, and A. M. Okamura. Design considerations for robotic needle steering. *IEEE International Conference on Robotics and Automation*, pages 3599–3605, 2005.

[178] R. J. Webster III, A. M. Okamura, and N. J. Cowan. Toward active cannulas: Miniature snake-like surgical robots. *IEEE/RSJ International Conference on*

Intelligent Robots and Systems, pages 2857–2863, October 9-15 2006. Beijing, China (Finalist for Best Paper Award).

[179] R. J. Webster III, A. M. Okamura, and N. J. Cowan. Kinematics and calibration of active cannulas. *IEEE International Conference on Robotics and Automation*, 2008. Accepted.

[180] R. J. Webster III, A. M. Okamura, N. J. Cowan, G. S. Chirikjian, K. Y. Goldberg, and R. Alterovitz. Distal bevel-tip needle control device and algorithm, 2006. Provisional patent submitted 5/19/05, full patent submitted 5/19/06. US patent application number 11/436,995.

[181] R. J. Webster III, A. M. Okamura, N. J. Cowan, and R. H. Taylor. An active cannula for bio-sensing and surgical intervention. US and International Patent Pending.

[182] R. J. Webster III, J. Swenson, and N. J. Cowan. Differential kinematics and visual servoing for active cannulas. *International Journal of Robotics Research*, 2008. In Preparation.

[183] W. Wei, R. Goldman, N. Simaan, H. Fine, and S. Chang. Design and theoretical evaluation of micro-surgical manipulators for orbital manipulation and intraocular dexterity. *IEEE International Conference on Robotics and Automation*, pages 3389–3395, 2007.

[184] W. Wei, K. Xu, and N. Simaan. A compact two-armed slave manipulator

for minimally invasive surgery of the throat. *IEEE/RAS-EMB International Conference on Biomedical Robotics and Biomechatronics*, pages 287–292, 2006.

[185] Z. Wei, G. Wan, L. Gardi, G. R. Mills, D. B. Downey, and A. Fenster. Robot-assisted 3D − TRUS guided prostate brachytherapy: System integration and validation. *Medical Physics*, 31(3):539–548, 2004.

[186] P. M. White. Stress induced interposed connector, 2001. Patent 6,257,593.

[187] A. Wolf, H. B. Brown, R. Casciola, M. Schwerin A. Costa, E. Shamas, and H. Choset. A mobile hyper redundant mechanism for search and rescue tasks. *IEEE/RSJ International Conference on Intelligent Robots and Systems*, pages 2889–2895, 2003.

[188] P. Woo, J. Casper, B. Griffin, R. Colton, and D. Brewer. Endoscopic microsuture repair of vocal fold defects. *Voice*, 9(3):332–339, 1995.

[189] K. Xu and N. Simaan. Actuation compensation for flexible surgical snake-like robots with redundant remote actuation. *IEEE International Conference on Robotics and Automation*, pages 4148–4154, 2006.

[190] J. Yanof, J. Haaga, P. Klahr, C. Bauer, D. Nakamoto, A. Chaturvedi, and R. Bruce. CT-integrated robot for interventional procedures: Preliminary experiment and computer-human interfaces. *Computer Aided Surgery*, 6(6):352–359, 2001.

[191] P. Yen, R. D. Hibberd, and B. L. Davies. A telemanipulator system as an

assistant and training tool for penetrating soft tissue. *Mechatronics*, 6(4):423–436, 1996.

[192] Y. A. Yu, S. Shabahang, T. M. Timiryasova, Q. Zhang, R. Beltz, I. Gentschev, W. Goebel, and A. A. Szalay. Visualization of tumors and metastases in live animals with bacteria and vaccinia virus encoding light-emitting proteins. *Nature Biotechnology*, 22:313–320, 2004.

Vita

Robert J. Webster, III

Vanderbilt University, Mechanical Engineering Department
VU Station B 351592, 2301 Vanderbilt Place, Nashville, TN 37235-1592
Office Phone: (615)322-0193   Email: `robert.webster@vanderbilt.edu`
`http://research.vuse.vanderbilt.edu/MEDLab/`

CURRENT POSITION (AS OF 1/1/2008)

Assistant Professor, Mechanical Engineering, Vanderbilt University
Director of the Medical & Electromechanical Design Laboratory

EDUCATION

Ph.D. in Mechanical Engineering, Johns Hopkins University, December 2007
Dissertation: Design and Mechanics of Continuum Robots for Surgery
Advisors: Dr. Allison M. Okamura and Dr. Noah J. Cowan

M.S. in Mechanical Engineering, Johns Hopkins University, December 2004

B.S. in Electrical Engineering, Clemson University, May 2002
Summa Cum Laude, Departmental Honors, Thesis: The Electronic Ball Boy

HONORS AND AWARDS

Panelist NSF BME/RAPD Program, proposal review panel (December 2007)

Best Paper Finalist IROS 2006 for paper titled "Toward Active Cannulas: Miniature Snake-Like Surgical Robots."

Semifinalist Damon Runyon-Rachleff Innovation Award

National Science Foundation Fellowship (2003–2007)

Department of Defense NDSEG Fellowship (2002–2005)

Tau Beta Pi Fellowship (2002)

IEEE-RAD/IFRR School of Robotics Science–Design, Tokyo, Japan (2005)

Best Presentation, Engineering Research Center for Computer Integrated Surgical Systems and Technology Student Competition (2006)

Best Project, Advanced Computer Integrated Surgery Class, (2003)

NSF Travel Grants for conference attendance (5) 1999, 2000, 2002, 2004, 2006.

PUBLICATIONS
Journal Articles

1. R. J. Webster III, J. S. Kim, N. J. Cowan, G. S. Chirikjian, and A. M. Okamura, "Nonholonomic Modeling of Needle Steering," *International Journal of Robotics Research*, Vol. 25, No. 5-6, pp. 509-525, May-June 2006.

2. R. J. Webster III, "Object Capture with a Camera-Mobile Robot System: An Introductory Robotics Project," *IEEE Robotics and Automation Magazine*, Vol. 13, Issue 1, pp. 85-88, March 2006

3. R. J. Webster III, T. E. Murphy, L. N. Verner, and A. M. Okamura, "A Novel Two-Dimensional Tactile Slip Display: Design, Kinematics and Perceptual Experiments," *ACM Transactions on Applied Perception*, Vol. 2, No. 2, pp. 150-165, 2005.

4. E. Boctor, R. J. Webster III, H. Mathieu, A. M. Okamura, and G. Fichtinger, "Virtual Remote Center of Motion Control for Needle Placement Robots," *Computer-Aided Surgery*, Vol. 9 No. 5 pp. 175-183, 2004.

5. E. M. Boctor and M. A. Choti and E.C. Burdette and R. J. Webster III, "3DUS-Guided Robotic Needle Placement: An Experimental Evaluation", *International Journal of Medical Robotics and Computer Aided Surgery* (Submitted)

6. R. J. Webster III, J. M. Romano, and N. J. Cowan, "Design and Mechanics of Active Cannulas," *IEEE Transactions on Robotics*. (In Preparation)

7. R. J. Webster III and B. A. Jones, "A Unified Approach to Constant Curvature Continuum Robotics," *IEEE Transactions on Robotics*. (In Preparation)

8. R. J. Webster III, J. Swensen, and N. J. Cowan, "Differential Kinematics and Visual Servoing for Active Cannulas," *International Journal of Robotics Research*. (In Preparation)

Patents

1. R. J. Webster III, A. M. Okamura, N. J. Cowan, and R. H. Taylor, "An Active Cannula for Bio-Sensing and Surgical Intervention" US and International Patents Pending.

2. R. J. Webster III, A. M. Okamura, N. J. Cowan, G. S. Chirikjian, K. Y. Goldberg, and R. Alterovitz, "Distal Bevel-Tip Needle Control Device and Algorithm" US Patent Pending.

3. M. Matinfar, R. J. Webster III, and I. I. Iorachita, "Tensiometer for Biological Tissues," US provisional patent.

Book Chapters

1. D. Stoianovici, R. J. Webster III, L. R. Kavoussi, "Surgical Robotic Applications in Minimally Invasive URL-Oncology Surgery" In: Moore R, Bishops J, edt. *Minimally Invasive URL-Oncologic Surgery.* London & New York: Taylor & Francis, ISBN 1-84184-566-3; 2005: 353-363

Refereed Conference Proceedings

1. R. J. Webster III, J. M. Romano, and N. J. Cowan, "Kinematics and Calibration of Active Cannulas," *IEEE International Conference on Robotics and Automation*, 2008, (Accepted)

2. M. Quirini, R. J. Webster III, A. Menciassi, and P. Dario, "Design of a Pill-Sized 12–legged Endoscopic Capsule Robot," *IEEE International Conference on Robotics and Automation*, 2007, pp. 1856-1862.

3. N. Ng Pak, R. J. Webster III, A. Menciassi, and P. Dario, "Electrolytic Bourdon Tube Microactuator for Reconfigurable Surgical Robots," *IEEE International Conference on Robotics and Automation*, 2007, pp. 3371-3376.

4. J. Romano, R. J. Webster III, and A. M. Okamura, "Teleoperation of Steerable Needles," *IEEE International Conference on Robotics and Automation*, 2007, pp. 934-939.

5. *R. J. Webster III, A. M. Okamura, and N. J. Cowan, "Toward Active Cannulas: Miniature Snake-Like Surgical Robots" *IEEE/RSJ International Conference on Intelligent Robots and Systems*, 2006, pp. 2857–2863. ***FINALIST - IROS BEST PAPER AWARD***

6. *R. J. Webster III, J. Memisevic and A. M. Okamura, "Design Considerations for Robotic Needle Steering," *IEEE International Conference on Robotics and Automation*, 2005, pp. 3599–3605.

7. R. J. Webster III, N. J. Cowan, G. S. Chirikjian, and A. M. Okamura, "Nonholonomic Modeling of Needle Steering," *9th International Symposium on Experimental Robotics 2004*, Springer Tracts in Advanced Robotics, Vol. 21, Mar 2006, pp. 35–44.

8. *T. Murphy, R. J. Webster III, and A. M. Okamura, "Design and Performance of a Two-Dimensional Tactile Slip Display," *Eurohaptics*, 2004, pp. 130–137.

9. E. M. Boctor, R. J. Webster III, M. A. Choti, R. H. Taylor, and G. Fichtinger, "Robotically Assisted Ablative Treatment Guided By Freehand 3D Ultrasound," *Computer Assisted Radiology and Surgery*, 2004, pp. 503–508.

10. E. M. Boctor, R. J. Webster III, H. Mathieu, A. M. Okamura, and G. Fichtinger, "Virtual Remote Center of Motion Control for Needle Placement Robots." *Sixth International Conference on Medical Image Computing and Computer Assisted Intervention MICCAI 2003*, Springer Lecture Notes in Computer Science (Vol. 2878), 2003, pp. 157–164.

11. *A. M. Okamura, R. J. Webster III, J. T. Nolin, K. W. Johnson, and H. Jafry, "The Haptic Scissors: Cutting in Virtual Environments," *IEEE International Conference on Robotics and Automation*, 2003, pp. 828–833.

12. *R. J. Webster III and A. S. Brannon, "The Electronic Ball Boy: A Reactive Visually Guided Mobile Robot For the Tennis Court," *IEEE International Conference on Robotics and Automation*, 2002, Vol. 2, pp. 2054–2059.

Indicates oral presentation by R. J. Webster III.

Posters

1. J. Memisevic, R. J. Webster III and A. M. Okamura, "Design of a Needle Steering Robot for Minimally Invasive Surgery," *Biomedical Engineering Society Fall Meeting*, Philadelphia, PA, Oct. 13–16, 2004.

INVITED PRESENTATIONS

1. "Superelastic Robots for Minimally Invasive Surgery," University of Georgia, Faculty of Engineering, Athens, GA, March 19, 2007.

2. "Superelastic Robots for Minimally Invasive Surgery," Duke University Department of Department of Mechanical Engineering and Materials Science, Durham, NC, February 27, 2007.

3. "Superelastic Robots for Minimally Invasive Surgery," Vanderbilt University, Department of Mechanical Engineering, Nashville, TN, February 19, 2007.

4. "Enhancing Surgical Robotics Through Haptics and Dexterous Instruments," Workshop on Medical Diagnosis, Micro Surgery, and Performance Evaluation at IEEE/RSJ International Conference on Intelligent Robots and Systems (IROS), Beijing, China, October 10, 2006.

5. "Design and Modeling of Dexterous Superelastic Instruments for Minimally Invasive Surgery" Engineering Research Center for Computer Integrated Surgical Systems and Technology Seminar Series, Johns Hopkins University, Baltimore, MD, May 3, 2006.

EXPERIENCE

Active Cannulas, Haptic Exploration Lab, Johns Hopkins   2005-present
Invented concentric curved superelastic tube design and developed both hand actuation and robotic actuation mechanisms. Devised and experimentally validated beam mechanics-based curved tube interaction models for forward and differential kinematics. Spearheaded successful efforts to involve both industrial partners (Philips) and medical collaborators (Pulminologist Nevins Todd). Primary author of one funded and one pending grant proposal, two conference papers, US and International patent applications, and three in-preparation Journal Articles.

Steerable Needles, Haptic Exploration Lab, Johns Hopkins   2003-present
Developed initial idea of steering via bevel forces, performed pilot studies for and co-authored successful NIH R21 grant proposal in 2003. Designed both a friction drive and a lead-screw actuated mechanism for steering flexible needles with force/torque sensing. Experimentally validated non-holonomic models for needle kinematics. Assisted Ron Alterovitz and Ken Goldberg at UC Berkely on FEM tissue models and colleagues at JHU on model-based control techniques. Developed mouse ballistics-based control laws for teleoperation, and demonstrated improvement in targeting. Mentored two undergraduate students. Co-author of one conference paper, successful NIH R21 and R01 proposals. Primary author of two conference papers, a US full patent application, and a journal article.

Mobile Medical Robots, Scuola Superiore Sant'Anna, Italy   2006
Designed lead-screw driven slot-follower mechanism to simultaneously miniaturize capsule to pill-size and add four legs. Optimized design numerically. Developed electrolytic silicon bourdon tube microactuator for modular reconfigurable medical robots. Co-author of two conference papers, two journal articles in preparation.

Tactile Haptics, Haptic Exploration Lab, Johns Hopkins   2003-2006
Invented 2-DOF tactile haptic slip display consisting of an actuated sphere. Optimized design via multiple prototypes and performed perceptual experiments to evaluate the fidelity of information perceived via fingertip slip. Developed a combined force/slip virtual paper manipulation experiment demonstrating human performance improvement with slip feedback. Developed a kinematic model of wheel/ball interaction to control ball surface velocity at fingertip. Co-author of a conference paper, primary author of a journal article.

Bio-Sensing, Maryland Spine Center   2006-present
Created a mechanical tension sensor to ensure nerve safety in spondloptosis operations. Recruited and mentored a graduate student to construct and experimentally validate the design. Planned experiments on a live pig will compare electrical and mechanical nerve root measurements. Primary Author of a provisional patent, conference and journal submissions planned.

Image-Guided Robotic Needle Placement, Johns Hopkins University   2002-2004
Developed fast heuristic searches that quickly align needles with surgeon's desired path from entry point to target. Algorithms are general-purpose and do not require a specific robot design, require very little calibration, and can be used with unencoded robots. This potentially reduces required dollar cost of needle placement robots and enhances patient safety. Co-author of a conference paper and a journal article. A second journal article has been submitted for publication.

Industrial Experience   1998-2001
Telecommunications Co-Op Engineer, 1998-2001 (4 Terms - 1 yr. Total)

Adtran, Huntsville, Alabama
ADTRAN Student Representative to Clemson, Fall, 1999
Assignment: Improve Corporate-University relations and recruit new co-ops.
Nuclear Power Plant Maintenance Engineer, Summer, 1998
Plant Vogtle, Georgia

Undergraduate Research   2001-2002

Hyperredundant 'Elephant's Trunk' Robot, Clemson University
Developed whole arm manipulation techniques to throw a basketball through a hoop.
Advised by Ian Walker.
Image-Guided Mobile Robots, University of Newcastle, Australia
Designed a computer vision/mobile robot system to capture tennis balls. Developed algorithms for obstacle avoidance, multiple objectives, rolling balls etc. Primary author of a conference paper and a Robotics and Automation Magazine article.
Advised by Rick Middleton.
Inchworm Pipecrawler Robot, Savannah River Technology Center
Built an inchworm pipecrawler robot to inspect the interior of pipes at a nuclear facility.
Advised by James Wong.
Battlebots, Central Savannah River Area Robot Warriors
Robot 'Jabberwok' defeated previous year champion Y-pout

TEACHING
Students Advised:

Joe Romano, Summer Research Experience for Undergraduates, 2006
Teleoperation of Flexible Medical Robots

Babak Matinfar, Graduate CS Student, 2006
Nerve Tensionometer for Spondyloptosis Surgery

Jasenka Memisevic, Summer Research Experience for Undergraduates, 2004
Steering Flexible Needles

Courses Assisted in Teaching:

Mechatronics
Taught Laboratory. Johns Hopkins University, 2006. Instructor: Allison M. Okamura
Teaching Evaluation Score Not Yet Available

Design and Analysis of Dynamic Systems
Taught Laboratory. Johns Hopkins University, 2005. Instructor: Allison M. Okamura
Teaching Evaluation Score 4.66/5.00

Surgery for Engineers
TA and Laboratory Assistant. JHU Medical Institute, 2004. Instructor: P. Rand Brown
Teaching Evaluation Score 4.31/5.00

Calculus I and Chemistry 101
Tutor, Clemson University, 2000.

GRANTS

1. NSF BME/RAPD R21: "Active Cannulas for Bio-Sensing and Surgery" (N. J. Cowan (PI), A. M. Okamura, R. J. Webster III). (8/2007-8/2010) Total award amount $240k. Vanderbilt Subcontract $180,589 over three years.

2. NIH R01: "Steering Flexible Needles in Soft Tissue" (Allison M. Okamura (PI), Gregory S. Chirikjian, Noah J. Cowan, Gabor Fichtinger, Ken Goldberg, Kieran Murphy) (6/2007-6/2012) I wrote small sections of this proposal.

3. (Awarded) NIH R21: "Biomechanical Modeling for Steerable Needles" (A.M. Okamura (PI), G. S. Chirikjian, K. Goldberg, and N. J. Cowan), for $384,323 over two years (4/04-3/06). Performed preliminary studies and wrote sections of this proposal.

PROFESSIONAL ACTIVITIES

Service
Student Volunteer, OR2020 Operating Room of the Future Workshop, Ellicott City, Maryland, March 18-20, 2004

Memberships
Institute of Electrical and Electronics Engineers (IEEE), Washington Computer Aided Surgery Society (WashCAS), Tau Beta Pi, Eta Kappa Nu, IEEE Mechatronics, Communications, and Power Societies, CISSRS Student Computer Integrated Surgery Society, Medical Image Computing and Computer-Assisted Intervention (MICCAI) Society

Technical Reviews
IEEE Transactions on Robotics, ASME Journal of Dynamic Systems, Measurement, and Control, IEEE International Conference on Robotics and Automation, Eurohaptics, Worldhaptics, Workshop on Robot-Human Communication (RO-MAN), International Conference on Medical Image Computing and Computer Assisted Intervention (MICCAI)

PERSONAL DATA

Citizenship: United States

Contact Information:
Department of Mechanical Engineering
VU Station B 351592
2301 Vanderbilt Place
Nashville, TN 37235-1592

Phone: 615-322-0193
Fax: 615-343-6687
Email: robert.webster@vanderbilt.edu
Laboratory Web page: http://research.vuse.vanderbilt.edu/MEDLab/